UNIVERSITY OF OKLAHOMA

GRADUATE COLLEGE

IV-VI MATERIALS & DEVICES FOR THERMOPHOTOVOLTAIC (TPV) POWER GENERATION

A DISSERTATION

SUBMITTED TO THE GRADUATE FACULTY

in partial fulfillment of the requirements for the Degree of

DOCTOR OF PHILOSOPHY

By

MANISHA CHATTERJEE CHAKRABURTTY
Norman, Oklahoma
2016

IV-VI MATERIALS & DEVICES FOR THERMOPHOTOVOLTAIC (TPV) POWER GENERATION

A DISSERTATION APPROVED FOR THE
SCHOOL OF ELECTRICAL AND COMPUTER ENGINEERING

BY

Dr. Patrick McCann, Chair

Dr. Michael Santos

Dr. James Sluss

Dr. Brian Grady

Dr. Hjalti Sigmarsson

© Copyright by MANISHA CHATTERJEE CHAKRABURTTY 2016
All Rights Reserved.

ACKNOWLEDGEMENTS

I want to express my sincere gratitude for all the guidance, help, support and encouragement that I received from my advisor Prof. McCann and especially for his patience as I went through the dissertation process. I feel very fortunate to have the opportunity to have studied in his group at the University of Oklahoma. I want to thank Dr. Santos for his willingness to serve on my committee and for answering my questions. I am grateful to Dr. Grady for agreeing to serve on my doctoral advisory committee and for initially directing me to the right doctoral program. I am also grateful to Dr. Sluss, and Dr. Sigmarsson for agreeing to serve on my doctoral advisory committee

I am thankful to Dr. Khosrow Namjou for performing some of the critical data acquisition that was part of this dissertation. I would like to express my appreciation to Chomani Gaspe, Len Olona, Lihua Zhao, Xinghua Shi, Gary Cai, Dr. Ghulam Hasnain, James Jeffers, Holly Hao, Lin Lei, for their help, friendship and for making the difficult days of the dissertation process a little easier.

I would like to thank my husband, for supporting my dreams and not trying to stop me from all the technical projects that I tried to implement over the years. My two boys, they are the joy and light of my life and the strength behind everything I do. I would also like to thank my Grandfather for instilling the love of learning in me at a very early age and setting the example of lifelong learning with his own life.

TABLE OF CONTENTS

ACKNOWLEDGEMENTS…………….……………………………….…………….….. iv
TABLE OF CONTENTS…………………………………..…………………….…v
LIST OF TABLES …………………………………..………………….....…….vii
LIST OF FIGURES…………………………………..……………………..….ix
ABSTRACT…………………..…………………………..……………………xiv

Chapter 1: Introduction to Thermophotovoltaic Technology…………….…………1
1.1 Motivation.…………………………………………………..…………..1
1.2 Electromagnetic Radiation…………………………………..…………..2
1.3 Infrared spectroscopy……………………………………………..…..5
1.4 Thermal detectors ……………………………………….………...6
1.5 Photodetectors……………………………………………………..……7
1.6 Portable Power Technologies………………………………………..…..8
Eletrochemical………………………………………………………...9
Mechanical….……………………………………………………...13
Solid State…………………………………………………….………13
1.7 Introduction to PVand TPV technology……………………………..…14
1.8 Selecting the optimum TPV emitter……………………………………..…..15
1.9 Physical limits to the efficiency of the PV/TPV cell…………………….…16
1.10 Current scope of thermophotovoltaic technology…………………….....18
1.11 Low Bandgap TPV cells………………………………………………..…20
1.12 Recent published work on promising TPV technology…………..……..20
1.13 Dissertation Organization…………………………………………….…22
References.………………………………………………………………..….23

Chapter 2 Density of States and Intrinsic Carrier Concentrations in Bulk and Quantum Well Materials…………………………………………………………………...26
2.1 Introduction…………………………………………………………....26
2.2 Fermi Dirac Distribution Function………………………………….…29
2.3 DOS and Intrinsic Carrier Concentration in Bulk Semiconductors 33
2.4 Quantum Well Physics…………………………………………………38
2.5 Fermi Dirac Distribution Function in Quantum Well Materials ……..…..44
2.6 Density of States and Intrinsic Carrier Concentration in QW Materials....46
2.7 Summary and Conclusion…………………………………….………..50
References…………………………………………..…………………..52

Chapter 3 Density of States and Intrinsic Carrier Concentrations in IV-VI Semiconductor Bulk and Quantum Well Materials…………………………………..53
3.1 Introduction………………………………………………………..…...53
3.2 Effect of temperature on IV-VI bulk and QW semiconductor material…..55
3.3 Effective mass in IV-VI bulk and QW semiconductor material………….56
3.4 Intrinsic Carrier Concentration in IV-VI in bulk semiconductor material..60
3.5 Intrinsic Carrier Concentration in IV-VI in QW semiconductor material..62

3.6 Summary and Conclusion……………………………..………………82
References…………………………………………………………………..……..83

Chapter 4 Growth and characterization of IV-VI bulk material TPV Device……..…86
4.1 MBE Growth of IV-VI Semiconductor TPV Device Structure ……..….86
4.2 Fabrication of IV-VI Semiconductor TPV Devices……………………...89
4.3 IV-VI Semiconductor Device Characterization LED & Detector Results.90
4.4 Current versus Voltage Characterization……………………….……...91
4.5 Device Characterization with Broadband Illumination…………………..96
4.6 Discussion…………………………………………………….………104
4.7 Recombination and Minority Carrier Lifetime…………………………109
Radiative Recombination…………………………………………....110
Shockley Read Hall (SRH)……………………………………….…112
Surface Recombination……………………………..……………113
Auger Recombination……………………………………….………114
Total Recombination……………………………………..……….115
4.8 Assessment of Fabricated IV-VI Semiconductor Devices……..……..…115
4.9 Summary and Conclusions……………………………..……………..116
References……………………………………………..…………………117

Chapter 5 Characterization of a IV-VI Semiconductor TPV Device using a Bandpass Filter and a Winston Cone………………………………………………….…119
5.1 Introduction…………………………………….………………119
5.2 Bandpass Filter…………………………………..…………………121
5.3 Winston Cone …………………………………..…………………129
5.4 Test Setup: Power Density Measurement Procedure………………..…..132
5.5 TPV Device Characterization with Bandpass Filter & Winston Cone….135
5.6 Discussion ……………………………………………………….…...139
5.7 Summary and Conclusions……………………………....……...........142
References…………………………………………………………………..…144

Chapter 6 Summary and Future Investigations…………………………….………145
6.1 Summary of Results……………………………………….……….…145
6.2 Recommendations for Future Investigations………………………….…..149
Multi-Junction IV-VI Semiconductor Based TPV Devices………....149
Multiple Quantum Well (MQW) Materials in Multi-Junction Cells..152
Optical Design Monte-Carlo Analysis for RayTracing……………..153
6.3 Summary and Conclusion……………………………………………157
References…………………………………………………………..……..159

Appendix A…………………………………………………………………....160
Appendix B…………………………………………………………….……165

LIST OF TABLES

Table 1.1: Categories within the IR spectrum, their application and the detection technology……………………………………………………………………….…..5

Table 1.2: Energy densities of portable power technologies……..9

Table 1.3: The comparison of maximum Carnot efficiency achievable from a TEG and a TPV generator……………………………………………………………18

Table 1.4: Bandgaps and Cut-off-Wavelengths for IV-VI TPV materials…………20

Table 1.5: Efficiency of a multijunction cell with & without photon recycling….…21

Table 2.1: Effective masses, bandgaps, degeneracies, effective densities of states and intrinsic carrier concentration for III-V materials………………………………….....36

Table 2.2: Table 2.2: Density of States and energy values for GaAs………………49

Table 3.1: Effective masses for electrons and holes in PbSe and $Pb_{0.93}Sr_{0.07}Se$…….60

Table 3.2: Effective masses, effective density of states for the conduction and valence band and the intrinsic carrier concentration concentration for bulk PbSe, $Pb_{1-x}Sr_xSe$..61

Table 3.3: The degeneracy split for PbSe well and $Pb_{0.93}Sr_{0.07}Se$ barrier……………..63

Table 3.4: The degeneracy split for PbSe well and $Pb_{0.90}Sr_{0.10}Se$ barrier……….…....64

Table 3.5: The degeneracy split for PbSe well and $Pb_{0.87}Sr_{0.13}Se$ barrier……….……64

Table 3.6: The degeneracy split for PbSe well and $Pb_{1-x}Sr_xSe$ barrier……………...65

Table3.7: Intrinsic carrier concentration, dark current & open circuit voltage for bulk $Pb_{0.93}Sr_{0.07}Se$ and 3 nm wide PbSe/ $Pb_{0.87}Sr_{0.13}Se$ Quantum Well at 300K…………….70

Table3.8: Intrinsic carrier concentration, dark current & open circuit voltage for bulk $Pb_{0.90}Sr_{0,10}Se$ and 2.5 nm wide PbSe/ $Pb_{77.5}Sr_{22.5}Se$ Quantum Well at 300K…………...71

Table3.9: Intrinsic carrier concentration, dark current & open circuit voltage for bulk $Pb_{0.87}Sr_{0.13}Se$ and 2 nm wide PbSe/ $Pb_{73}Sr_{27}Se$ Quantum Well at 300K…………..72

Table 5.1: Refractive indices, thickness, and the number of layers used for the design of two different bandpass filters…………………………………………..…………127

Table 5.2: Winston cone entrance diameter, exit diameter, focal ratio (f), and the length of the cone……………………..………………………………………..130

Table 5.3: IR source power, incident optical power density, short circuit current density (Jsc), open circuit voltage (Voc), fill factor (FF), electrical output power and power conversion efficiency ( ) for TPV device number M292 b1a3 at 283K..……140

Table 5.4: Incident power, absorbed photons, incident photons, e-charge/current, EQE and IQE for M292 b1a3 at 283K……….……………………………………...142

LIST OF FIGURES

Figure 1.1: Electromagnetic spectrum and the typical applications of each spectrum range……………………………………..……………………………………..2

Figure 1.2: Blackbody radiation as a function of wavelength for various temperatures ……………………………………………………………………………….....3

Figure 1.3: Plot of Earth atmosphere transmittance in the infrared region of the electromagnetic spectrum………………………….……………………………..4

Figure 1.4: an example of the absorption spectrum of Silicone measured with a Fourier Transform infrared spectroscopy (FTIR) system……………………………...6

Figure 2.1: The Fermi Dirac distribution at 250K, 300K and 350 K for an intrinsic semiconductor with a 450 meV bandgap……………………………………..……31

Figure 2.2: Expanded view of the Fermi Dirac distribution at 250K, 300K and 350 K for an intrinsic with a 450 meV bandgap………………………………………... 32

Figure 2.3: Arrhenius plot of intrinsic carrier concentration for bulk GaAs, Si, GaSb, Ge, InSb as a function of inverse temperature…………………………….……... 38

Figure 2.4: Quantum well (2D) with finite height of barriers……………………....40

Figure 2.5: Solutions of finite potential well problem are at the intersections of the semi-circles and the trigonometric functions………………………..……………..42

Figure 2.6: A 4 nm wide Quantum well (2D) with finite height rectangular potential barrier and wells showing the quantized energy sub bands……………………..……43

Figure 2.7: The Fermi Dirac distribution at 250K, 300K and 350 K for a multiple quantum well structure having 275 meV bandgap material for the well and 450 meV bandgap material for the barrier…………....……………………………………..44

Figure 2.8: Expanded view of the Fermi Dirac distribution at 250K, 300K and 350 K for a multiple quantum well structure having 275 meV bandgap well material and 450 meV bandgap barrier material………………..……………………………………… 45

Figure 2.9: Density of states per unit area and energy for a 7 nm wide quantum well with finite barriers where $m^*/m_0 = 0.067$……………………………….……………….50

Figure 3.1: The surface of constant energy in k-space for lead salt materials eight half ellipsoids of revolution centered at the L points on the first Brillouin zone boundary...53

Figure 3.2: Arrhenius plot of Intrinsic carrier concentration for bulk PbSe, $Pb_{0.93}Sr_{0.07}Se$, $Pb_{0.90}Sr_{0.10}Se$ and $Pb_{0.87}Sr_{0.13}Se$ as a function of inverse temperature……..61

Figure 3.3: The conduction band L-Valley degeneracy splitting energies for n=1 electrons for $PbSe(E_g = 275meV)$ well and $Pb_{0.87}Sr_{0.13}Se(E_g = 450meV)$ / $Pb_{0.775}Sr_{0.225}Se(E_g = 550meV)$ / $Pb_{0.73}Sr_{0.27}Se(E_g = 650meV)$ barrier at 300K. Degeneracy splitting energies were calculated using $Schrödinger's$ equation………………………66

Figure 3.4: Illustration of the degeneracy-split normal and oblique valleys in the conduction band for $Pb_{0.93}Sr_{0.07}Se$ and $Pb_{0.87}Sr_{0.13}Se$ w showing the reduction in carrier density as the degeneracy split increased……………………………………………..67

Figure 3.5: Interband transition for bulk $Pb_{0.93}Sr_{0.07}Se$ and intersubband transition for PbSe / $Pb_{0.87}Sr_{0.13}Se$ quantum well……………………………………….……………70

Figure 3.6: Arrhenius plot of intrinsic carrier concentration for bulk $Pb_{0.93}Sr_{0.07}Se$ and 3 nm wide PbSe/ $Pb_{0.87}Sr_{0.13}Se$ Quantum Well as a function of inverse temperature….72

Figure 3.7: Arrhenius plot of intrinsic carrier concentration for bulk $Pb_{0.90}Sr_{0,10}Se$ and 2.5 nm wide PbSe/ $Pb_{0.775}Sr_{0.225}Se$ Quantum Well as a function of inverse temperature73

Figure 3.8: Arrhenius plot of intrinsic carrier concentration for bulk $Pb_{0.87}Sr_{0.13}Se$ and 2 nm wide PbSe/ $Pb_{0.73}Sr_{0.27}Se$ Quantum Well as a function of inverse temperature….74

Figure 3.9: Arrhenius plot of dark current for bulk $Pb_{0.93}Sr_{0.07}Se$ and 3 nm wide PbSe/ $Pb_{0.87}Sr_{0.13}Se$ Quantum Well as a function of inverse temperature……………...75

Figure 3.10: Arrhenius plot of dark current for bulk $Pb_{0.90}Sr_{0,10}Se$ and 2.5 nm wide PbSe/ $Pb_{0.775}.Sr_{0.225}Se$ Quantum Well as a function of inverse temperature…………....76

Figure 3.11: Arrhenius plot of dark current for bulk $Pb_{0.87}Sr_{0.13}Se$ and 2 nm wide PbSe/ $Pb_{0.73}Sr_{0.27}Se$ Quantum Well as a function of inverse temperature……………..77

Figure 3.12: Dark current in a pn junction device for bulk $Pb_{0.93}Sr_{0.07}Se$, $Pb_{0.90}Sr_{0.10}Se$, and $Pb_{0.87}Sr_{0.13}Se$ material as a function of inverse lattice temperature for electron and hole minority carrier lifetime of 100ns , 10 ns and 1 ns……………………………..78

Figure 3.13: Arrhenius plot of open circuit voltage for bulk $Pb_{0.93}Sr_{0.07}Se$ and 3 nm wide PbSe/ $Pb_{0.87}Sr_{0.13}Se$ Quantum Well as a function of inverse temperature………..79

Figure 3.14: Arrhenius plot of open circuit voltage for bulk $Pb_{0.90}Sr_{0.10}Se$ and 2.5 nm wide PbSe / $Pb_{0.775}Sr_{0.225}Se$ Quantum Well as a function of inverse temperature………80

Figure 3.15: Arrhenius plot of open circuit voltage for bulk $Pb_{0.87}Sr_{0.13}Se$ and 2 nm wide PbSe / $Pb_{0.73}Sr_{0.27}Se$ Quantum Well as a function of inverse temperature……….80

Figure 3.16: Open circuit voltage in a pn junction device for bulk $Pb_{0.93}Sr_{0.07}Se$, $Pb_{0.90}Sr_{0.10}Se$, and $Pb_{0.87}Sr_{0.13}Se$ as a function of inverse lattice temperature for electron and hole minority carrier lifetime of 100ns, 10 ns and 1 ns……………..81

Figure 4.1: Bandgap energy and lattice constants of various binary IV-VI compounds and related ternary and quaternary alloys at 77 K. ………………………….....…….86

Figure 4.2: MBE system used to fabricate IV-VI TPV devices at University of Oklahoma………………………………………………………………..……………87

Figure 4.3: $Pb_{0.93}Sr_{0.07}Se$ TPV diode structure epitaxially grown using MBE. This growth was identified as number M292……………………………………...…….88

Figure 4.4: Fabricated TPV device……………………………………….…………89

Figure 4.5: LED emission and detector photo-response of M292 showing the bandgap energy of the material is 450 meV…………………………………………. 91

Figure 4.6: Linear plot of current versus voltage characteristics of M292 a2e1, for temperatures between 10^0C and 50^0C ………………………………………….. 93

Figure 4.7: Linear plot of current versus voltage characteristics of M292 b1a3, for temperatures between 10^0C and 50^0C. ………………………….……………………93

Figure 4.8: Semi-logarithmic plot of current versus voltage characteristics of M292 a2e1 for temperatures between 10^0C and 50^0C ……………………….…………94

Figure 4.9: Semi-logarithmic plot of current versus voltage characteristics of M292 b1a3 for temperatures between 10^0C and 50^0C. …………………………………... 94

Figure 4.10: Expanded view of the reverse bias region for M292 b1a3 at temperatures between 10^0C and 50^0C ……………………………………………95

Figure 4.11: The resistance area product for M292 a2e1 at 300 K…………………95

Figure 4.12: The resistance area product for M292 b1a3 at 300 K………………....96

Figure 4.13: Experimental setup for measurement of current versus voltage characteristics with broadband thermal illumination…………………..……………..97

Figure 4.14: Semi-logarithmic plot of current versus voltage characteristics of M292 a2e1, for temperatures between $10^0 C$ and $50^0 C$ for broadband thermal radiation with the device located at a hot spot with an optical power density of 5.6 Watts/cm^2…….98

Figure 4.15: Semi-logarithmic current versus voltage characteristics of M292 b1a3, for temperatures between $10^0 C$ and $50^0 C$ ……………………………………...99

Figure 4.16: Current density versus voltage plot for M292 a2e1 and b1a3 at 10^0C.100

Figure 4.17: Current density versus voltage characteristics plot of M292 a2e1 & b1a3 at 40°C……………………………………….……………………………...101

Figure 4.18: A plot of measured open circuit voltage vs heat sink temperature for M292 a2e1 and b1a3…………………………………………………….……101

Figure 4.19: Electrical power generated by M292 b1a3 at heat sink temperatures of 10^0C and 40^0C………………………………………………………………….. 102

Figure 4.20: Power conversion efficiency vs heat sink temperature for M292 a2e1 and b1a3. Conversion efficiency is calculated by taking the ratio of electrical output power density of M292 over the incident broadband thermal radiation power density……………………………………………………………………..…..103

Figure 4.21: Arrhenius plot of intrinsic carrier density of $Pb_{0.93}Sr_{0.07}Se$ from 30^0C to 60^0C ……………………………………………..……..…………………....106

Figure 4.22: Calculated Arrhenius plots of reverse bias saturation current for a $Pb_{0.93}Sr_{0.07}Se$ pn junction from 30^0C to 60^0C with minority carrier lifetimes of 10 ns and 100 ns along with measured dark current data at -26 mV for two different devices.……………………………………..………………………………..107

Figure 4.23: Auger coefficient (IV –VI materials) vs temperature [23]……..……114

Figure 5.1: Transfer matrix parameters………………………………….……...122

Figure 5.2: Transmission matrix for a dielectric stack …………………………....125

Figure 5.3: Multiple reflections and refractions for light moving through layers…125

Figure 5.4: Transmission as a function of wavelength for dielectric filter (CWL~5µm)……………………………………………………………………127

Figure 5.5: Transmission as a function of wavelength for dielectric filter (CWL~2.5μm)……………….…………………………………………….…….…...128

Figure 5.6: Transmission spectrum of Thorlab's IR bandpass filter……………….129

Figure 5.7: Schematic diagram of a Winston cone light concentrator…………….....131

Figure 5.8: Power density measurement setup………………………..……..…132

Figure 5.9: Measured infrared optical power exiting the Winston cone as a function of distance from the exit aperture for two infrared source powers ……………...…133

Figure 5.10: Measured infrared optical power exiting the Winston cone as a function of lateral distance perpendicular to the cone axis for two infrared source powers.....134

Figure 5.11: LED emission and detector response spectra of pn junction device M292-C showing a bandgap energy of around 450 meV…………...………………135

Figure 5.12: Test setup for measuring the performance of TPV device number M292 b1a3…………………………………..…………………………………...136

Figure 5.13: Dark and illuminated current voltage characteristics of M292 b1a3...137

Figure 5.14: Dark and illuminated current density and voltage characteristics of M292 b1a3………………………………..……………………………………138

Figure 5.15: Electrical output power of M292 b1a3 at a heat sink temperature of 10°C…………………………………………………………………………139

Figure 6.1: Tunnel junction between a dual junction cell, $Eg_1 > Eg_2$…………..…150

Figure 6.2: TPV multi-junction cell with five junctions…………………………...151

Figure 6.3: IV-VI QW designed for maximum degeneracy split………….………153

Figure 6.4: Light reflected and transmitted at the interface z = 0………………..…...154

Figure 6.5: Planar collimator design…………………………………….………...156

Figure 6.6: The mechanism to collimate light using total internal reflection and refraction…………………….…………………………………………………156

ABSTRACT

IV-VI semiconductors, with direct gap conduction and valence band extrema at the L-point in k-space, are characterized by four-fold L-valley degeneracy. Prior work [1] has shown that this degeneracy can be removed with quantum confinement in the [111] direction. The first half of this dissertation demonstrates the beneficial effects that this degeneracy removal can have on the performance of thermophotovoltaic (TPV) devices. PbSe quantum wells (QWs) with $Pb_{1-x}Sr_xSe$ barriers were evaluated. Using Schrodinger's equation and the two different effective masses for charge carriers in the degeneracy split normal (or longitudinal) L-valley and the higher energy three-fold degenerate oblique L-valleys, the largest possible degeneracy splitting energies for three different normal valley subband energy gaps of 450 meV, 550 meV and 650 meV were found to be 21.7 meV, 37.1 meV, and 43.9 meV, respectively. Intrinsic carrier concentrations were calculated for these QWs using density of states functions and Fermi-Dirac statistics. It was found that thermally generated intrinsic carrier density can be reduced by more than an order of magnitude as compared to that of a bulk IV-VI semiconductor material with the same bandgap energy. Dark current and open circuit voltages for TPV devices made from IV-VI materials were also calculated. Results show that use of optimal QW designs can increase open circuit voltages by almost a factor of two as compared to a bulk material having the same band gap energy. With a doubling of open circuit voltages, the incorporation of QW designs in IV-VI semiconductor TPV devices is predicted to enable a 100% increase in optical-to-electrical power conversion efficiencies.

The second half of this dissertation discusses the experimental results and analysis of data obtained from characterization of pn junction devices fabricated from a bulk $Pb_{0.93}Sr_{0.07}Se$ active layer. The pn junction layer, which consisted of a 2 µm thick n-type layer doped with bismuth to give an electron density of $n=4x10^{18}$ cm^{-3} and a 2 µm thick p-type layer with a selenium overpressure during growth to give a hole density of $p=4x10^{17}$ cm^{-3}, was grown by molecular beam epitaxy (MBE) on silicon, transferred to copper using a novel flip-chip eutectic bonding method, and fabricated into mesa-etched device structures with sizes of 200 x 200 μm^2 and 400 x 400 μm^2. Current-versus-voltage characterization was performed with and without broadband illumination at different heatsink temperatures to assess the performance of these devices as TPV cells. Measured reverse bias saturation current densities at -26 mV were observed to increase from 7.5 mA/cm^2 to 26.9 mA/cm^2 as the lattice temperature was increased from 10°C to 50°C. After accounting for band gap temperature dependence and thermal generation effects, these values were consistent with an increase in minority carrier lifetime from 10 ns at 10°C to 100 ns at 50°C. These data show a clear lifetime enhancing thermal re-excitation effect and confirm the high quality of these IV-VI semiconductor epitaxial layer materials for device fabrication applications. Moreover, these data show that high materials quality is maintained during device processing and that there are no significant surface recombination problems with the fabricated device structures. These pn junction devices were also operated at room temperature and in continuous wave (cw) mode as light emitting diodes (LEDs) and as mid-infrared detectors. Representing the first known demonstration of such mid-infrared IV-VI semiconductor device operation, LED

emission spectra and detector spectral response showed a bandgap energy of 450 meV (2.76 μm cutoff wavelength) for the MBE-grown $Pb_{0.93}Sr_{0.07}Se$ layer. Broadband illumination measurements were performed with spectrally-filtered thermal radiation and a parabolic optical concentrator (Winston cone). Unlike illumination with a laser, these testing conditions accurately simulate the environment that a TPV cell would experience in an actual TPV generator system. Open circuit voltages as high as 116 mV, short circuit current densities as high as 409 mA/cm^2, and fill factors of 43% with an incident optical power density of 620 mW/cm^2 were observed. Generated electrical power was greater than 20 mW/cm^2 thus giving an optical-to-electrical power conversion efficiency of 3.3% for this non-QW device. External quantum efficiency (EQE) and an estimated internal quantum efficiency (IQE) based on an assumed 40% reflection loss were calculated to be 33% and 55%, respectively. Further optimization of materials growth, device design, and processing techniques as well as incorporation of anti-reflective coatings and use of higher incident optical power densities should ultimately enable power conversion efficiencies in the range of 10% for this bulk material single-junction device. This dissertation concludes with suggestions for how future work can be conducted to take advantage of the unique materials properties of nano-structured IV-VI semiconductors and to use QW materials within multi-junction TPV cell designs to achieve power conversion efficiencies that can be significantly larger than the good values that have already been experimentally demonstrated here.

[1] H. Z. Wu, N. Dai, M. B. Johnson, P. J. McCann, and Z. S. Shi, "Unambiguous Observation of Subband Transitions from Longitudinal Valley and Oblique Valleys in IV–VI multiple Quantum Wells", *Applied Physics Letters* **78**, 2199 (2001).

Chapter 1

Introduction to Thermophotovoltaic Technology

To myself I am only a child playing on the beach,
while vast oceans of truth lie undiscovered before me.
Isaac Newton

1.1 Motivation

The motivation for this research comes from the energy industry, particularly from its continuous trend towards higher efficiencies and lower cost. Thermophotovoltaic (TPV) systems are a promising solution to the energy industry's search for auxiliary power generators and co-generation systems where electrical power is generated with no waste heat. This research investigates the use of IV-VI materials as a viable, more efficient and cost effective alternative for the currently more commonly used III-V materials for TPV devices. The objective of this research is to develop an efficient IV-VI semiconductor nanostructured detector / thermophotovoltaic device in order to harvest electrical power from thermal sources as described in Chapter 4 and 5. IV-VI semiconductor PN junctions were grown on Silicon using molecular beam epitaxy, and flip chip bonding was used to fabricate the devices. This represents the first known effort to explore the growth and fabrication of IV-VI semiconductor TPV devices using these manufacturing-friendly methods. The high power densities possible with TPV devices make them an attractive option for generation of electricity from thermal sources. Combustion of any kind can be used to heat a radiator which emits most of its photons in the mid-infrared portion of the electromagnetic spectrum. The radiant heat produced can be converted directly to electricity with a TPV cell much like a solar cell produces electricity from solar

radiation. A TPV based generator will ultimately be smaller, lighter, easier to maintain and less expensive than current electrical generating systems that are based on piston engines or steam turbines. Military applications, particularly unmanned reconnaissance vehicles, would benefit from a lightweight, near-silent source of electricity provided by a TPV system. Applications like these are driving a growing interest in TPV devices. As TPV devices are a form of an infrared (IR) photodetector, we need to discuss the electromagnetic radiation and different IR detectors currently available.

1.2 Electromagnetic Radiation

Electromagnetic radiation, described by Maxwell's equations, span a wavelength range from a few kilometers to less than a picometer. This spectral range is divided into many bands based on their applications and the sources and receivers of the

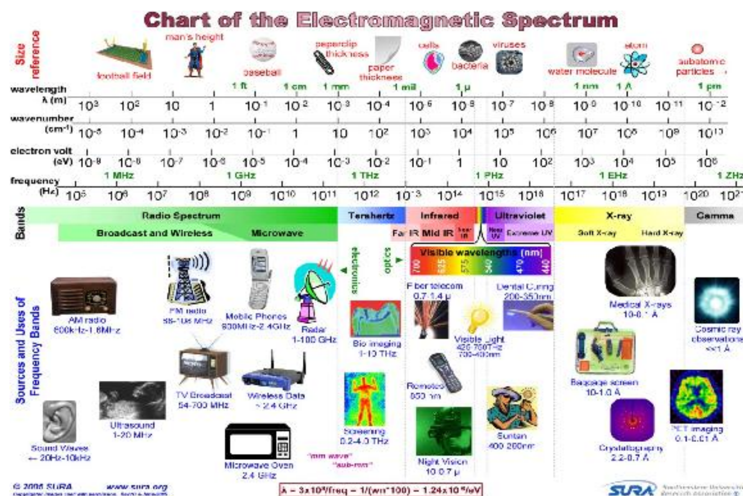

Figure 1.1: Electromagnetic spectrum and the typical applications of each spectrum range. (Image replicated from: http://www.t-lea.net/spectrumSURA.html.

radiation, as shown in Figure 1.1.

The infrared is a spectral range that starts from the edge of visible red light (~0.7 μ m) up to 100 μ m. According to Planck's law of black body radiation, all objects radiate electromagnetic waves based on their temperature and their emissivity, Equation 1.1 represents Planck's law and describes the electromagnetic radiation emitted by a black body at a definite temperature.

$$E(T,\lambda) = \frac{2\pi\varepsilon hc^2}{\lambda^5 (e^{\frac{hc}{\lambda kT}} - 1)} \tag{1.1}$$

where E (T,   ) is the power emitted per unit area, *h* is Planck's constant, *c* is speed of light,   is the wavelength, *k* is Boltzmann's constant and *T* is temperature of the object.   is the emissivity, which is a number between 0 and 1 and is defined as the ratio of the power emitted from an object to the power coming from an ideal blackbody. Blackbody spectrum at different temperatures are shown in Figure 1.2.

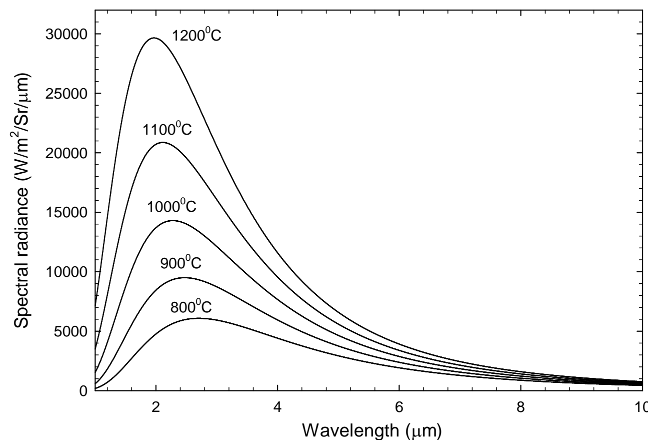

Figure 1.2: Blackbody radiation as a function of wavelength for various temperatures.

The position of the blackbody peak can be determined using Wein's law, however, for terrestrial applications, the transmission spectrum of the atmosphere is important in most infrared applications. The transmission spectrum of earth atmosphere is shown in

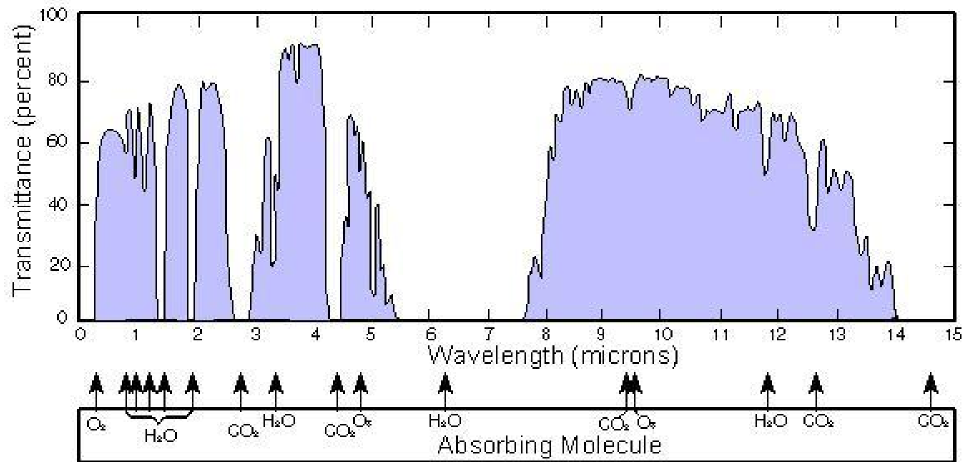

Figure 1.3: Plot of Earth atmosphere transmittance in the infrared region of the electromagnetic spectrum. (Image replicated from https://ewhdbks.mugu.navy.mil/ transmit.gif).

Figure 1.3. The infrared spectral range is divided into several bands based on the transmitted radiation intensity of the objects. There are two main atmospheric windows, they are between 3µm and 5µm and between 8µm and 12µm. Most thermal imaging devices are designed to operate in either of these windows.

Table1.1: Categories within the IR spectrum, their application and the detection technology.

Name	Shorthand	Wavelength (μm)	Common application	Detector technology
Near infrared	NIR	0.7-1	Fiber telecommunication Night vision devices	Photocathode CCD
Short-wave infrared	SWIR	1-3	Long distance fiber telecommunication	InGaAS Lead-Salt compounds
Mid-wave infrared	MWIR	3-5	Missile tracking and heat seeking devices (utilizing 3-5 μ m atmospheric window) Can be used for an ideal TPV device	InSb Type-II superlattice HgCdTe Lead selenide (PbSe)
Long-wave infrared	LWIR	8-12	Thermal imaging	Bolometer HgCdTe Type-II superlattice
Very long wave infrared	VLWIR	12-30	Thermal imaging for cooler objects	Doped silicon Type-II superlattice

1.3 Infrared Spectroscopy

In molecules, the vibrational modes of heteronuclear bonds create a dipole oscillator. As a result, infrared light can excite these vibrational modes and the IR photons get absorbed. The exact positions of these absorption lines depend on the strength of the bond and the masses of the atoms involved in the bond. It also depends on the type of the vibration such as bending or stretching. A typical absorption spectrum for an organic molecule (polydimethylsiloxane) is shown in Figure 1.4. As can be seen, the C-H stretch at 2963 cm^{-1} is fairly clean and isolated from the other stretching and rocking modes from 1500 cm^{-1} to 500 cm^{-1}. These absorption features

can be used to identify specific molecules by comparing a measured spectrum to a known spectrum.

Infrared detectors are broadly divided into two categories: thermal detectors and photodetectors. Thermal detectors are detectors that are sensitive to a change of the temperature caused by the infrared radiation. While photodetectors are based on Einstein's photoelectric effect where the absorption of a photon produces a direct electrical signal. A TPV device is essentially a photodetector operating in the mid infrared spectral region that is designed for high electrical power production.

1.4 Thermal Detectors

The principles of operation for thermal detectors involve changes in the temperature of the detector, and this change in the temperature causes some changes in the material properties such as resistivity that can be used to measure the temperature and consequently the infrared radiation intensity. Based on the property that changes

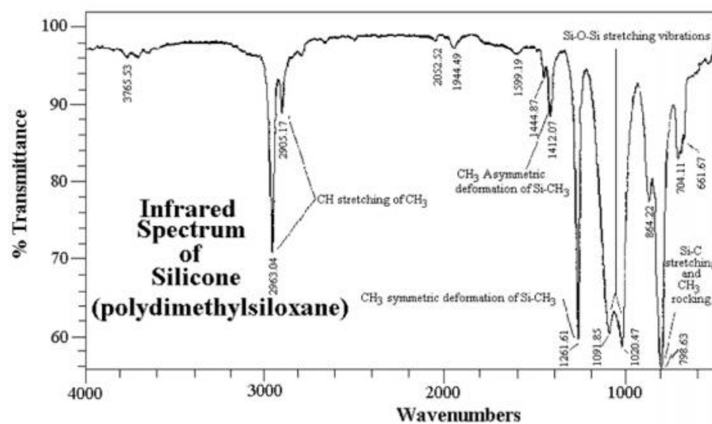

Figure 1.4 an example of the absorption spectrum of Silicone measured with a Fourier Transform infrared spectroscopy (FTIR) system. (Image replicated from http://www.wcaslab.com/tech/tbftir.htm).

as the result of temperature and the mechanism of the change, thermal detectors are divided into different categories. Thermal detectors normally have the advantage of operating at room temperature. However, due to their principles of operations, which is based on the change in temperature, they are relatively slow and are not suitable for high speed applications such as tracking. The two main categories of thermal detectors are Pyroelectric and Bolometers:

In pyroelectric materials the change in temperature leads to a change in the polarization. This change in polarization can induce some change in voltage or current depending on the detector configuration, which can produce an electrical signal. Common pyroelectric detectors are made with two materials: Lithium Tantalite (LiTaO3), and Triglycine Sulfate (TGS) and Deuterated Triglycine Sulfate (DTGS).

In bolometers, the resistance of the material changes as a result of the change in the temperature. The materials that are suitable for bolometers should have a high thermal coefficient of the resistance. Commonly used materials for bolometers are vanadium oxides which have a very high thermal coefficient at temperatures around 60^0C. Using this principle, micro bolometers and infrared imagers have been developed that can work at room temperature.

1.5 Photodetectors

Photodetectors, unlike thermal detectors that are sensitive to temperature, are sensitive to photons. The absorption of photons in photodetectors results in the excitation of charge carriers. These carriers create an electrical signal that can be used for the detection of light. Photodetectors can be categorized based on their absorption mechanism or the mechanism to collect the excited carriers. The main condition for

the photon to get absorbed is that the energy of the photon should be larger than the band gap of the photodetector material. III-V compounds such as InGaAs or InSb, IV-VI compounds such as lead selenide (PbSe) or lead sulfide (PbS), and II-VI compounds such as HgCdTe are the main materials used for interband infrared absorption. Extrinsic absorption is based on the excitation of electrons from states in the valence band to states in the conduction band. These detectors normally need to operate at very low temperatures to avoid intrinsic thermal generation of charge carriers. Once the carriers are generated due to the photon absorption, they need to be collected to create a photo signal without a large influence of background thermally generated carriers. Photodetectors can be divided into two categories: photoconductive and photovoltaic. For photoconductors the transport mechanism is dominated by drift of photo generated charge carriers and depending on the lifetime of the excited carriers and travel time between the two metal contacts, the detector exhibits a reduction in resistance depending on the intensity of the absorbed light. In photovoltaics, an internal built-in electric field is created due to the grading of the doping level from p to n type. This built in electric field and potential barrier also blocks the majority carriers on both sides of the junction and the dominant transport mechanism in these devices is the drift of the minority carriers due to the built-in electric field.

1.6 Portable Power Technologies

This section presents some other technologies being developed. Three major types of generators are studied here: electrochemical, thermal, and mechanical. Electrochemical generators includes batteries and fuel cells. Mechanical generators are traditional heat engines such as internal combustion engines and Stirling engines

where the mechanical energy is used to turn a generator. Thermal generators such as Stirling engines also use heat energy but have moving parts. The results are summarized in Table 1.2.

Table 1.2: Energy densities of portable power technologies.

Technology	Energy Density [Wh/kg]	Ref
Lithium-ion battery	150	[1]
Zinc-air battery	300	[2]
Lithium-air battery	3000	[3]
Direct methanol fuel cell	1100	[4]
Solid oxide fuel cell	7000	[5]
Stirling engine	1500	[6]
Thermoelectric	750	[7]
Thermophotovoltaics	750	

Energy densities do not tell the whole story. There are additional considerations such as size, scale, power density, cost, reliability, lifetime, etc. For example, a cordless drill needs high power density and low cost, making batteries a good choice. Soldiers in the field may favor TPV, thermoelectrics, or solid oxide fuel cells for the ability to burn arbitrary fuels. Even if energy density were the sole criteria, Table 1.2 would not be completely fair comparison because some technologies are mature while others are very much in the research phase.

Electrochemical

Batteries and fuel cells derive electricity from an oxidation-reduction reaction occurring at two electrodes: the negative anode and positive cathode. The electrodes are separated by an electrolyte though which ions but not electrons can pass. Electrons are liberated at the anode where they are forced through the load to the cathode. Ions

move through the electrolyte so that there is no charge accumulation. In a fuel cell the reactants are supplied externally and the byproducts are removed, whereas in batteries the reactants are an integral part of the cell.

Lithium-ion batteries

For traditional rechargeable batteries, lithium technology offers the highest energy density. There are many different varieties; we will focus on the lithium-ion battery as an example. In the lithium ion battery, Li^+ ions migrate from one lithium compound at the anode to another one at the cathode and electrons move through the load during discharge. The two lithium compounds have different electrochemical potentials in order to generate the battery's voltage. The anode compound should have a low potential and the cathode should have a high potential to give a large cell voltage. LiAl and Li_xC_6 are good cathodes; $LiMn_2O_4$, $LiNiO_2$, and $LiFePO_4$ are good anodes. For example, the cathode reaction is

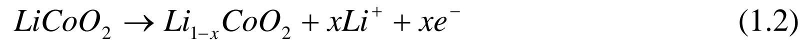

$$LiCoO_2 \rightarrow Li_{1-x}CoO_2 + xLi^+ + xe^- \quad (1.2)$$

and the anode reaction is

$$xLi^+ + xe^- + 6C \rightarrow Li_xC_6 \quad (1.3)$$

For $LiCoO_2$ cathode and a graphite anode. Metallic lithium would make a good cathode except it is highly reactive. During charging, when the Li+ plates out as lithium metal on the cathode, long dendrites can form, bridge the electrolyte, and short out the cell [1].

Zinc-air and lithium-air batteries

Zinc-air and lithium-air batteries are more accurately described as fuel cells than batteries. High energy density can be achieved because the oxidizer does not need to be stored in the cell. Oxygen from the air is used to oxidize the metal which is internal to the battery. The Li-O_2 cell can potentially have an energy density of 3000 Wh/kg. The anode is metallic lithium, the cathode is porous carbon, and the electrolyte is ceramic [3]. Zinc-air batteries operate on the same principle as lithium-air batteries. The theoretical energy density is 1350 Wh/kg, but in practice is only 200 or 300 Wh/kg. Zinc-air batteries can be recharged by replacing the zinc electrode [2].

Direct methanol fuel cells

Methanol is a desirable fuel because it is readily available, easy to store, and has 50% the energy density of propane. Direct methanol fuel cells (DMFCs) react methanol with oxygen from the air. The methanol is supplied at the anode where it is oxidized

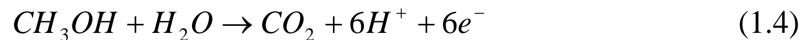

$$CH_3OH + H_2O \rightarrow CO_2 + 6H^+ + 6e^- \quad (1.4)$$

with a Pt-Ru catalyst. Oxygen is supplied at the cathode where a Pt catalyst is often used,

$$\frac{3}{2}O_2 + 6H^+ \rightarrow H_2O \quad (1.5)$$

The H^+ ions move through a proton exchange membrane separating the anode and cathode and electrons move through the load. Water production is problematic in DMFCs. The anode needs water to supply the reaction and the membrane needs to stay moist. However, methanol can dissolve in the water and cross the membrane to

the cathode where it is oxidized directly. Methanol crossover lowers the cell voltage and wastes fuel [5]. The best power densities reported for microscale DMFC, with comparable size to a TPV system, are in the range from 4 to 30 mW/cm^2 at an energy density of 1100 Wh/kg [4].

Solid oxide fuel cells

Solid oxide fuel cells (SOFCs) operate at high temperatures (around 900^{0}C) and can process naturally occurring fuels directly. The oxidizer is injected at the $La_{1-x}Sr_xMnO_3$ or $La_{1-x}Sr_xCoO_3$ cathode where the reaction is

$$\frac{1}{2}O_2 + 2e^- \rightarrow O^{2-} \tag{1.6}$$

The O^{2-} ions migrate through the electrolyte and, of course, the electrons move through the external circuit. The electrolyte is yttria-stabilized zirconia and becomes permeable to O^{2-} ions at high temperatures. The other half of the reaction happens at the anode where the fuel is injected. The anode nickel-zirconia cermet where nickel serves as a catalyst. For hydrogen, the reaction is

$$H_2 + O^{2-} \rightarrow H_2O + 2e^- \tag{1.7}$$

and for carbon monoxide it is

$$CO + O^{2-} \rightarrow C_2O + 2e^- \tag{1.8}$$

Complex fuels are reformed to hydrogen and carbon monoxide internally at the anode, then oxidized electrochemically according to the above reactions. A typical hydrogen-oxygen SOFC would have a voltage of 0.7 volts at a current density of 200 mA/cm^2 at 900^{0}C [5, 8].

Mechanical

Mechanical systems do not scale well because the surface to volume ratio increases thus increasing frictional loses, heat loses, etc. Furthermore, it is difficult to fabricate non planar structures such as shafts, bearings, valves, and seals at the microscale. Nevertheless, there are several impressive microscale mechanical generators, the most notable of which is the MIT micro turbine[9]. Powered by hydrogen, it is designed to generate 17 W of shaft power at 1.2 million rpm in a package the size of a shirt button. On the opposite end of the spectrum, Yale University reported a 42.5 We, 21% efficient JP8-fired Stirling engine generator[6]. At 1.7 kg and 400 cm^3, it is hardly microscale but could still be portable.

Solid State

Thermoelectric

A thermoelectric element is made of many thermocouples, thermally in parallel and electrically in series, sandwiched between a hot and cold reservoir. The thermo couples are semiconductors rather than metals. Thermoelectrics produce electricity directly from a temperature gradient by the Seebeck effect. When a temperature gradient is applied across a material, a voltage develops at the two ends,

$$V= \quad T \qquad (1.9)$$

where   is the Seebeck coefficient and T is the temperature difference. A thermoelectric material is characterized by a its figure of merit,

$$Z= \quad ^2/k \qquad (1.10)$$

Where   is the electrical conductivity and k is the thermal conductivity. A higher electrical conductivity leads to higher efficiency because less power is lost to Joule heating. Lower thermal conductivity means less heat can leak from the hot side to the

cold side without generating power. Commercially available thermoelectric generators (TEGs) are available for remote sensing and cathodic protection for pipelines and wells. These units have efficiencies around 6% in power ranges from 10 to 50 W [7, 8].

1.7 Introduction to PV and TPV Technology

The thermodynamic model of Shockley and Queisser [9] has established the theoretical limit for the efficiency of p-n junction devices in the ideal case where radiative recombination is dominant and where the source is considered as a black body. Thermophotovoltaic power was introduced by Wedlock [10] in 1963 and was studied in the last couple of decades [11-15]. TPV devices are semiconductor diodes that convert photons from a blackbody radiating source into electricity. Qualitatively they are the infrared analog to the semiconductor diodes that convert visible photons from the sun into electricity in solar photovoltaic (PV) devices. Thermal losses due to conduction, convection and radiation also play a big role in overall TPV system efficiency. TPV cells can use low-band gap materials to convert low energy, long wavelength IR photons to electric power. TPV devices operate at power densities of the order of 100-1000 times greater than solar PV cells, thus TPV diodes exhibit intrinsically higher current than PV diodes. The big advantage of TPV is that the emissivity of the source can be tailored to match the optical band gap of the semiconducting photo diode so it is possible to achieve good optical-to-electrical conversion efficiency. Low band gap (low E_g) materials for TPV devices have potentially important applications in the field of direct energy conversion due to the potential for efficient electrical power generation.

1.8 Selecting the Optimum TPV Emitter

The TPV conversion process begins with the emission of Lambertian distributed photon energy from an emitter. The standard derivation of thermal radiator blackbody emission proceeds by calculating the energy density of equilibrium photons at a temperature T_E [16]. The total energy density, ρ_E can be written as the integral of the phase-space volume $\frac{2}{(2\pi\hbar)^3} \times d^3r \times d^3p \times$ Bose Einstein distribution probability. Using $p = \hbar k$, where the wave-vector $|k| = \frac{\omega}{c}$ the total energy density is given by:

$$\rho_E = \frac{\hbar}{4\pi^3 c^3} \int \omega^3 f(\omega, T) \sin\theta \partial\omega \partial\theta \partial\varphi \equiv \int \rho_E(\omega, \theta, \varphi) \partial\omega \partial\Omega \qquad (1.11)$$

where, ω is the frequency, c is the speed of light, is Planck's constant divided by 2 , is the polar angle, is the azimuthal angle and d = sin d d . The Poynting vector (energy flux) is a function of ω , , and . The intensity of radiation, I (ω , ,), emitted from a blackbody is obtained by taking the dot product of the Poynting vector and the unit normal, n:

$$\mathrm{I}(\omega, \ , \ )\, d\omega\, d \ = \mathrm{P}(\omega, \ , \ ).n.d\omega\, d \qquad (1.12)$$

Integrating the above equation over a hemispherical solid angle yields the frequency dependent energy emission rate:

$$\mathrm{I}(\omega) = \frac{\hbar\omega^3}{4\pi^2 c^2} \frac{1}{e^{\hbar\omega/kT} - 1} \qquad (1.13)$$

1.9 Physical Limits to the Efficiency of the PV/TPV Cell

A TPV system is a photonic heat engine, therefore, the system is subject to thermodynamic (entropy generation) limitations where the maximum Carnot efficiency ($_{Carnot}$) is bounded by the operating temperature limits of the heat source emitter (T_E) and the heat sink (T_c) i.e., $_{Carnot}=\frac{T_E - T_c}{T_E}$. The Carnot formulation implicitly assumes the absence of internal entropy sources (i.e. irreversible losses). However, in a real heat engine where work is performed, internal entropy sources must be considered in the determination of achievable efficiency. The entropy sources in a TPV system include temperature drops necessary to transport energy from the heat source to the blackbody radiator, electric current flow necessary to generate power, and photon-induced deviations from diode equilibrium. The laws of thermodynamics limit the efficiency with which a thermophotovoltaic cell can extract electrical power from heat source just as they limit the power conversion efficiency of a steam turbine. The efficiency limit for a TPV cell can be estimated from the free energy carried by the blackbody and the process by which the light is converted into electricity in the cell. The free energy of light depends on how concentrated the light is, that is on how many photons there are in each radiation mode. If an electromagnetic mode with angular frequency S, is occupied by n (S) photons, the free energy of these photons can be written as [17]

$$F(S) = n(S) \quad S - kT\,[(1+n(S))\log(l+n(S)) - n(S)\log n(S)] \qquad (1.14)$$

where T_E is the emitter blackbody temperature. In the case of blackbody n (S) is the Bose Einstein distribution

$$n(S) = \frac{1}{e^{\frac{\hbar \check{S}}{kT_E}} - 1} \tag{1.15}$$

Using the Shockley Queisser's [9] model we can write the ultimate efficiency as

$$y_{\max} = \frac{J_{ph} V_g}{\int_0^{\infty} P(\check{S}) d\check{S}} \tag{1.16}$$

Where $V_g = \frac{E_g}{q}$, E_g is the band gap and energy $p(\check{S})$ the blackbody spectrum. The photon current density J_{ph} is given by

$$J_{ph} = q \int_{E_g}^{\infty} \frac{p(\check{S})}{h€} \tag{1.17}$$

In this analysis, we assume that the photon flux incident on the cell is limited by an optical filter that reflects all photons with energy less than the band gap back to the emitter and transmits all photons with energy greater than the band gap to the TPV cell. In this case the power absorbed by the cell is given by [18].

$$P_{abs} = \int_{E_g}^{\infty} p(\check{S}) d\check{S} \tag{1.18}$$

The ultimate efficiency is given by $y_{cell} = \frac{J_{ph} V_g}{P_{abs}}$ (1.19)

Ultimately, TPV generators will have significantly larger Carnot efficiencies than thermoelectric generators since the hot side temperature can be very high as the hot radiator is not in physical contact with the TPV device. Thermoelectric generators (TEG)s are limited to hot side temperatures that are typically below 600^0C due to the material, electronic and thermodynamic constraints. On the other hand, TPV devices

can work with radiators that can be as hot as 2000^0C.

1.10 Current Scope of Thermophotovoltaic Technology

The TPV concept was first demonstrated in the 1950s using a Coleman lantern and ordinary silicon solar cells [19]. Poor spectral efficiency was partially responsible for the low overall efficiency, meaning that the overlap between the emission spectrum of the lantern mantel and the spectral response of the solar cells was low. Only photons with energies above the bandgap of the solar cell can be converted into electricity. Thermal emitters at 1000-2000^0C are poorly matched to silicon photovoltaics which are better matched to the solar spectrum.

Table 1.3: shows the comparison of maximum Carnot efficiency achievable from a TEG and a TPV generator.

Technology	T_c(K)	T_E(K)	$y_{Carnot} = \frac{T_E - T_c}{T_E}$
TEG	300	873	66%
TPV	300	2273	87%

Improved spectral efficiency has only recently been enabled through scientific and technological advancements in two critical areas: low-bandgap semiconductor materials and photonic crystals. Low-bandgap photovoltaic cells convert a much larger portion of the infrared spectrum into electricity, thus enhancing power density [20, 21]. Photonic crystals enable spectral shaping, maximizing the efficiency [22]. Furthermore these advances allow a lower temperature (900-1100^0C) emitter [23], resulting in reduced thermal stresses, larger spectrum of available materials, and better

material stability thus extending the possible design space. With these advances, conversion efficiencies approaching 30% are theoretically achievable.

A thermal to electricity conversion efficiency of 23% at a power density of 0.8 W/cm^2 was demonstrated using InGaAs cells and a cold side filter in a laboratory environment [24]. However a self-contained TPV system with an efficiency even close to that figure was not demonstrated yet. Several TPV systems have been demonstrated but they are large and inefficient like their thermoelectric counterparts. The attempts are described below.

1. JX Crystals presented work on a 12.3% efficient thermal system based on GaSb cells and a radiant tube burner. The system was large and the cells were operating at 1 W/cm^2 electrical power density. The burner was operated at 1250^0C and had an antireflection coated flat tungsten emitter [25].

2. NASA built a 25 W propane-fired converter in a 3 inch diameter by 12 inch long cylindrical form factor with an efficiency of 3.0%, although the authors claim efficiencies of 6-7% should be possible [26].

3. The National University of Singapore reported a miniature TPV generator using a 150 W hydrogen burner around 1000^0C and GaAs cells with a cold side filter. The efficiency was 0.67% [27].

4. In 2011 Ivan Celanovic of Institute for Soldier Nanotechnologies at Massachusetts Institute for Soldier Nanotechnologies reported high-efficiency, millimeter-scale TPV generator consisting of low band gap InGaAsSb cells and photonic crystal having efficiency 2.2% [12, 22].

1.11 Low Bandgap TPV Cells

Low bandgap PV diodes are a critical component to achieving high efficiency. For a blackbody radiator, the electronic bandgap should be around the blackbody peak suggests blackbody peaks for reasonable emitter (1000-1500 K) temperatures fall in the 2 to 2.5 µm, thus the bandgap needs to be around 0.4 to 0.8 eV. Using PbSe (band gap 0.27 eV) as the base material and alloying with Sr to tune the bandgap to match the blackbody spectra is a way to obtain high power conversion efficiencies. Table 1.2 gives the bandgaps of three TPV materials: used for this study PbSe, $Pb_{0.93}Sr_{0.07}Se$, $Pb_{0.86}Sr_{0.14}Se$, and $Pb_{0.79}Sr_{0.21}Se$

Table 1.4: Bandgaps and Cut-off-Wavelengths for IV-VI TPV materials.

Material	Bandgap	Cut-off Wavelength
PbSe	0.27 eV	4.5µm (direct)
$Pb_{0.93}Sr_{0.07}Se$	0.45 eV	2.5µm (direct)
$Pb_{0.90}Sr_{0.10}Se$	0.55 eV	2.3µm (direct)
$Pb_{0.87}Sr_{0.13}Se$	0.65 eV	2µm (direct)

PbS (0.37 eV) by nature of its direct low bandgap, solves many of the problems alloying with Sr, while still being inexpensive. The pn junction can be created by diffusion or epitaxy. Bandgaps are easily tunable with a Sr alloy [28].

1.12 Recent Published Work on Promising TPV Technology

Data et al. have calculated the optimum band gap(s) for single junction and multijunction TPV cells based on detailed balance theory and assuming only radiative recombination. They experimented with different optimum band gaps to maximize the efficiency. They found TPV devices using high band gap cells are more sensitive to optical losses hence they need an extremely high photon recycling system. The

solution to this problem is having a multijunction cell. They have shown multijunction TPV cells have maximized the efficiency and the power density simultaneously, mitigated the impacts of optical losses in the overall TPV system performance and reduced the photocurrent and increased the voltage. The predictions of Data et al can be summarized in table 1.5.

Table 1.5: Efficiency of a multijunction cell with and without photon recycling.

Junctions	**Efficiency (%)**	**Efficiency (%) w/BSR**
1	25	33
2	34	40
3	39	45

The triple junction 45% predicted efficiency by Data et al is as good as a steam turbine.

Data et al, [30] concluded by showing that with a good photon recycling system like back surface reflector (BSR) or spectral filter, a multijunction TPV cell with a very low band gaps (below 0.5 eV) for the bottom cell can achieve an efficiency of greater than 50%. This is the highest photovoltaic conversion efficiency projected to date for a very low concentration factor. Data et al, stated "In order to exploit the full potential of multijunction TPV devices, very low band gaps (below 0.5 eV) are generally needed for the bottom cell.” This low band gap and low Auger recombination that make IV-VI materials the ideal choice for a multijunction TPV device.

1.13 Dissertation Organization

This dissertation outlines the feasibility of using IV-VI materials as an option for TPV device fabrication. Chapter 2 describes the importance of intrinsic carrier concentration as a key feature for a viable TPV device material. Chapter 3 details the IV-VI bulk material and quantum well structure, and how quantum confinement can reduce the density of states and increase V_{oc}. Chapter 4 details the diode parameters of MBE grown $Pb_{0.93}Sr_{0.07}Se$ material. Chapter 5 shows the considerable increase in efficiency for the same device as the bandpass filter and Winston cone is used to emulate the real life circumstance of a TPV generator. Chapter 6 provides conclusions and recommendations for future research in this area.

References:

[1] A. Manthiram. Materials aspects: an overview G. Nazri and G. Pistoia, editors, Science and Technology of Lithium Batteries, chapter 1, pages 3–37. Springer, 2003.

[2] J. Goldstein, I. Brown, and B. Koretz. New developments in the electric fuel ltd. zinc/air system. Journal of Power Sources, 80(1-2):171 – 179, 1999.

[3] B. Kumar, J. Kumar, R. Leese, J. P. Fellner, S. J. Rodrigues, and K. M. Abraham. A solid-state, rechargeable, long cycle life lithium–air battery. Journal of The Electro- chemical Society, 157(1):A50–A54, 2010.

[4] A. Kamitani, S. Morishita, H. Kotaki, and S. Arscott. Miniaturized micro DMFC using silicon microsystems techniques: performances at low fuel flow rates.J. Micromech Microeng., 18:125019, 2008.

[5] V. Bagotsky. Fuel Cells: Problems and Solutions. Wiley, 2009.

[6] A Gomez, J. J. Berry, S. Roychoudhury, B. Coriton, and J. Huth. From jet fuel to electric power using a mesoscale, efficient stirling cycle. Proceedings of the Combustion Institute, 31(2):3251 – 3259, 2007.

[7] A. McNaughton. Commercially available generators. In D.M. Rove, editor, CRC Handbook of Thermoelectrics, chapter 36, pages 459–469. CRC Press,1995.

[8] S.B. Schaevitz. A MEMS Thermoelectric Generator. PhD thesis, Massachusetts Institute of Technology, 2000.

[9] Shockley, W., Queisser, H.J., " Detailed Balance Limit of Efficiency of pn Junction Solar Cells" Journal of Applied Physics, 32, 510 (1961).

[10] D. Wedlock, Proceedings of the IEEE, (1963) 694-698

[11] B.D. Wedlock, "thermophotovoltaic energy conversion" Proceedings IEEE, Volume 51, pp 694-698, May 1963.

[12] I Celanovic, et al., "Design and optimization of a Dielectric stack filter for advanced thermophotovoltaic systems", MIT/Industry consortium on advanced automotive electrical/electronic components and systems RU 11 project report, MIT laboratory for electromagnetic and electronic systems, September 2002.

[13] C.A. Wang "Thermophotovoltaic Devices" M.I.T. Technical seminar, February 4 2004. Lincoln Laboratory, Massachusetts Institute of Technology. Lexington, MA.

[14] T. J. Coutts, M. W. Wanlass, J. S. Ward, S. Johnson, A review of Recent Advances imp, Twenty Fifth IEEE Photovoltaic Specialists Conference, Washington, DC (IEEE, 1996).

[15] T. J. Coutts, C. S. Allman, J. P. Benner, Eds., Thermophotovoltaic Generation of Electricity, the Third NREL Conference, Vol. 401, American Institute of Physics, Woodbury, New York, 1997, pp. 537.

[16] M. Planck, Verh. Dtsch. Phys. Ges. 2, 237 (1900).

[17] L. D. Landau and E.M. Lifshitz, Statistical Physics Part 1, (AddisonWesley, 1970)

[18] J. L. Gray and A. El-Husseini, AIP Conf. Proc. 358, 3 (1996)

[19] H.H. Kolm. Solar-battery power source. Quarterly progress report, solid state research, group 35, MIT-Lincoln laboratory, 1956.

[20] M. W. Dashiell, J. F. Beausang, H. Ehsani, G. J. Nichols, D. M. Depoy, L R. Danielson, P. Talamo, K. D. Rahner, E. J. Brown, S. R. Burger, P. M. Fourspring, W. F. Topper Jr., P. F. Baldasaro, C. A. Wang, R. K. Huang, M. K Connors, G. W. Turner, Z. A. Shellenbarger, G. Taylor, J. Li, R. Martinelli, D. Donetski, S. Anikeev, G. L. Belenky, and S. Luryi. Quaternary InGaAsSb thermophotovoltaic diodes.Electron Devices, IEEE Transactions on, 53 (12):2879–2891, Dec. 2006.

[21] T. Schlegl, F. Dimroth, A. Ohm, and A. W. Bett. TPV modules based on GaSb structures. In Sixth Conference on Thermophotovoltaic Generation of Electricity, pages 285–293. AIP, 2004.

[22] I. Celanovic, N. Jovanovic, and J. Kassakian. Two-dimensional tungsten photonic crystals as selective thermal emitters. Applied Physics Letters, 92(19): ,2008.

[23] P. F. Baldasaro, E. J. Brown, D. M. Depoy, B. C. Campbell, and J. R. Parrington. Experimental assessment of low temperature voltaic energy conversion.In The first NREL conference on thermophotovoltaic generation of electricity, pages 29–43. AIP, 1995.

[24] B. Wernsman, R. R. Siergiej, S. D. Link, R. G. Mahorter, M. N. Palmisiano, R. J. Wehrer, R. W. Schultz, G. P. Schmuck, R. L. Messham, S. Murray, C. S. Murray, F. Newman, D. Taylor, D. M. Depoy, and T. Rahmlow. Greater Than 20% Radi- ant Heat Conversion Efficiency of a Thermophotovoltaic Radiator/Module System Us- ing Reflective Spectral Control. IEEE Transactions on Electron Devices, 51:512–515, March 2004

[25] L. M. Fraas, J. E. Avery, and H. X. Huang. Thermophotovoltaic furnace generator for the home using low bandgap gasb cells. Semiconductor Science and Technology, 18(5):S247, 2003.

[26] E. Doyle, K. Shukla, and C. Metcalfe. Development and demonstration of a 25 watt thermophotovoltaic power source for a hybrid power system.Technical Report TR04- 2001, National Aeronautics and Space Administration, August 2001.

[27] Y. Wenming, C. Siawkiang, S. Chang, X. Hong, and L. Zhiwang. Research on micro- thermophotovoltaic power generators with different emitting materials. Journal of Micromechanics and Microengineering, 15(9):S239, 2005.

[28] W. Z. Shen, H. F. Yang, L. F. Jiang, K. Wang, and G. Yu, H. Z. Wu and P. J. McCann," Band gaps, effective masses and refractive indices of PbSrSe thin films: Key properties for mid infrared optoelectronic device applications" J. Appl. Phys., vol. 91, no. 1, pp. 3319–3327, Jan. 2002.

[29] Alejandro Datas Medina" Development of Solar Thermophotovoltaic Systems" PhD Dissertation; Universidad Politecnica De Madrid.; 2011.

[30] A. Datas, Optimum semiconductor bandgaps in single junction and multijunction thermophotovoltaic converters Sol. Energy Mater. Sol. Cells 94 (134) (2015) 275–290.

Chapter 2

Density of States and Intrinsic Carrier Concentrations in Bulk and Quantum Well Materials

How wonderful that we have met with a paradox..
Now we have some hope of making progress.
Niels Bohr

2.1 Introduction

The intrinsic carrier concentration, n_i, is a fundamental quantity in semiconductor physics. It is involved in almost all calculations that relate to responses to excitations. For example, n_i strongly influences minority carrier densities and dark current, an important parameter for PV/TPV devices. Therefore, the exact quantification of n_i is of prime importance for an improved understanding and design of semiconductor devices. The thermal excitation of an electron from the valence band to the conduction band creates free charge carriers in both bands. The intrinsic concentration of these carriers is n_i. The intrinsic carrier concentration describes the number of electrons in the conduction band or the number of holes in the valence band in an intrinsic (no impurities or other defects that contribute electrons or holes) material. This number of carriers depends on the band gap of the material, the density of states for electrons and holes and on the temperature of the material. A small band gap will make it easier for an electron to be thermally excited across the band gap, and therefore the intrinsic carrier concentration is higher in low band gap materials. This translates directly to PV/TPV cell efficiency. Let's consider a p-n junction single band gap TPV cell. Accurate models include series and parallel resistances as well as other diode parameters such as additional diodes or a diode ideality factor [1], but for simplicity,

let's focus on the ideal photovoltaic cell model. Equation (2.1) is the diode equation for a pn junction with no series resistance and infinite parallel resistance.

$$J_{dark}(V) = J_0\left(e^{\frac{qV}{nkT}} - 1\right) \qquad (2.1)$$

where J_0 is the reverse bias saturation current, n is the ideality factor, k_B is Boltzmann's constant and T is temperature in Kelvins. When illuminated, current can be generated by photons that have energies greater than the band gap energy. The current-voltage characteristic is then described by the Shockley diode equation (2.2) where J_{ph} is the photocurrent density. For the illuminated cell, ideally each photon above the bandgap E_g contributes one elementary charge q. When a photovoltaic cell is illuminated, the current-voltage curve is shifted and electrical power can be extracted from the cell.

$$J(V) = J_0\left(e^{\frac{qV}{nkT}} - 1\right) - J_{ph} \qquad (2.2)$$

There is a specific current density J_m and voltage V_m where the maximum power output, or maximum rectangular area under the curve, is obtained. The diode equation includes the dark saturation current density, J_0.

$$J_0 = qA\left(\frac{D_n n_p}{L_n} + \frac{D_p p_n}{L_p}\right) \qquad (2.3)$$

Eq. (2.3) defines J_0, where q is the elementary charge, D_n and D_p are the diffusion coefficients, L_n and L_p are the diffusion lengths for electrons and holes respectively, and n_p and p_n are the electron and hole concentrations on the p-type

and n-type sides respectively. It can be seen that several material parameters are required in order to calculate the dark saturation current density. We will show later in this chapter that J_0 increases as n_i increases, thus a reduction of intrinsic carrier density is key to reduction of reverse bias saturation (dark) current. A large band gap will make it more difficult for a carrier to be thermally excited across the band gap, and therefore the intrinsic carrier concentration is lower in higher band gap materials. Alternatively, for low band gap materials the added efficiency obtained by utilizing the more abundant low energy photons from a thermal source is counteracted by a larger density of thermally generated carriers. A reduction in the density of states for low band gap materials can reduce J_0 and increase open circuit voltage. J_0 can be significantly managed/reduced by reducing the density of states using quantum confinement techniques which will be discussed in the following sections and in Chapter 3. The overall current versus voltage characteristic of a pn junction when illuminated can be approximated as the sum of the short circuit photocurrent and the dark current. Therefore the net current density in an ideal case can be written by considering the sign of photocurrent as positive

$$J = J_{sc} - J_0 (e^{\frac{qV}{nk_B T}} - 1) \tag{2.4}$$

where J_{sc} is the short circuit current density generated by the absorbed light. The potential difference under open circuit conditions $V = V_{oc}$ can be derived from equation (2.4) by setting J=0 and solving for qV_{oc}

$$qV_{oc} = nk_B T \ln\left(\frac{J_{sc}}{J_0} + 1 \right) \tag{2.5}$$

The dark saturation current density J_0 has a thermodynamic lower limit because the cell not only absorbs radiation but also emits radiation. Frequently, models of J_0 depending on E_g use an approximation in the form defined in Eq. 2.6. Sze reported Eq. 2.6 for high radiation densities [2].

$$J_0 \approx CT^{\frac{3}{2}} e^{\frac{-E_g}{k_B T}} \tag{2.6}$$

The J_0 value of a PV cell can be determined by measuring the current under reverse bias conditions where V<<0 and J_{dark} in Eq. (2.1) goes to J_0. Eq. (2.3) shows that J_0 increases exponentially as E_g decreases thus reducing V_{oc}. At low radiator temperatures, when the blackbody spectral power distribution is broad and flat, the power emitted near the thermophotovoltaic cell band gap is not an appreciable percentage of the total emitted power, but as the radiator temperature increases, the blackbody spectral radiance increases and shifts towards shorter wavelengths. This leads to higher percentages of the emitted radiation being usable by the thermophotovoltaic cell.

2.2 Fermi Dirac Distribution Function

The simplest model for optical absorption between the valence and conduction bands in a bulk semiconductor is that an electron is raised from the valence band to a state of essentially the same momentum in the conduction band (a "vertical" transition). The number of energy states that are available for electrons in the bands, is described by the density of states (DOS) function, g (E). The expression $g(E)dE$ gives the number of states in the energy range [dE]. To find the total number of

electrons in the conduction band, we multiply this DOS with the probability that each energy level will have an electron occupying it and integrate across the conduction band. The Pauli Exclusion Principle forbids multiple identical electrons from occupying the same state simultaneously. For any given orientation, the spin of an electron may be +1/2 (spin up) or -1/2 (spin down). At T = 0, the lowest energy states are filled first, and then the next lowest, and so on. Thus, at T = 0 K, the distribution of electrons can be written as

$$f(E,\mu) = u(\mu - E) \tag{2.7}$$

where $u(\mu - E) = 1$ for $E < \mu$ and $u(\mu - E) = 0$ for $E > \mu$. Equation (2.7) shows that all states are filled below a characteristic energy, μ, the chemical potential. In the case of electrons the chemical potential is also known as the Fermi energy, $E_F = \mu$. Equilibrium requires that the electrons have the same temperature as the material that holds them. For arbitrary temperature, the electrons are described by the Fermi Dirac distribution:

$$f(E,\mu) = \frac{1}{1 + \exp\left[\frac{(E-\mu)}{k_B T}\right]} \tag{2.8}$$

The Fermi Dirac distribution is only valid if the number of fermions in the system is large enough so that adding one more fermion to the system has negligible effect on μ.

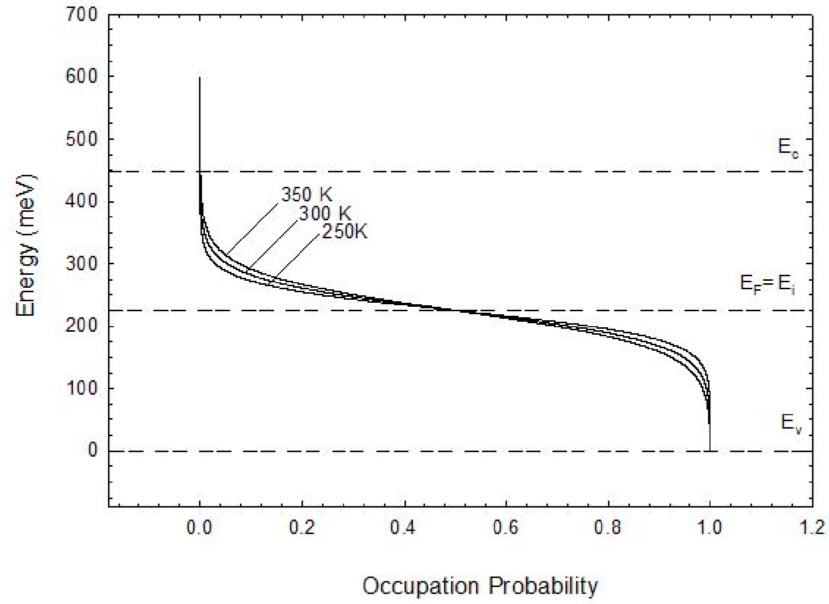

Figure 2.1: The Fermi Dirac distribution at 250K, 300K and 350 K for an intrinsic semiconductor $(E_f = E_i)$ with a 450 meV bandgap.

The above figure plots the Fermi Dirac probability function, Eq (2.8) and for the case of bulk semiconductor at 250K, 300K and 350 K when E_f is $\frac{E_g}{2}$, and the band gap energy of the semiconductor is 450 meV.

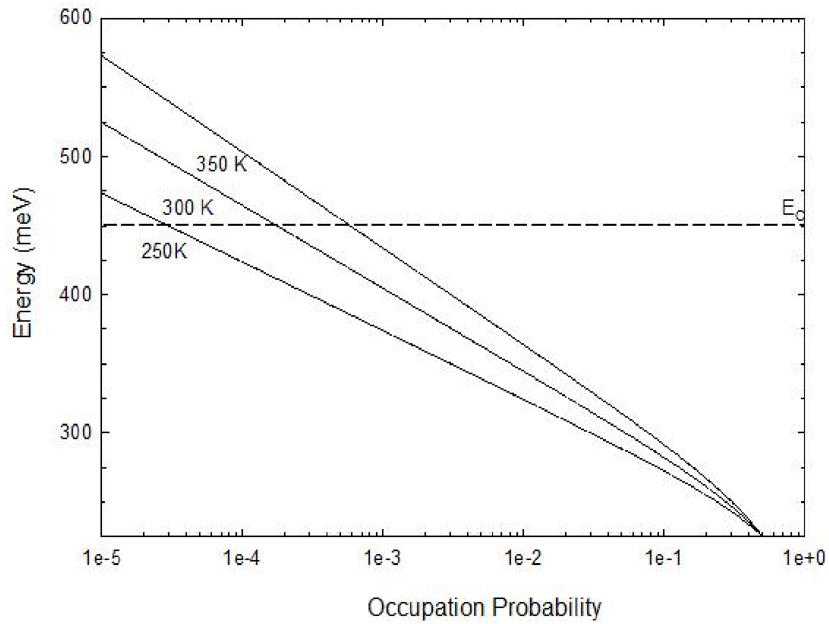

Figure 2.2: Expanded view of the Fermi Dirac distribution at 250K, 300K and 350 K for an intrinsic ($(E_f = E_i)$ with a 450 meV bandgap.

The above figure is an expanded view near the conduction band edge of the Fermi Dirac distribution function for 250K, 300K and 350K for an intrinsic semiconductor of band gap energy 450 meV. Note that the probability of electron occupation of conduction band states increases 20 times as the temperature rises from 250K to 350K.

2.3 Density of States and Intrinsic Carrier Concentration in Bulk Semiconductors

To understand the energy and momentum distributions, we need to know how many states are available for these particles to occupy in a particular system. For a number of particles in a three-dimensional system, such as in a bulk crystalline semiconductor, we can understand this by applying the Sommerfield model to the semiconductor [3] where the wave function at opposite ends of the crystal are equal. The volume of a unit cell (V_k^0) in the k-space occupied by one state is

$$V_k^0 = k_x * k_y * k_z = \frac{(2f)^3}{L^3} \tag{2.9}$$

where k is the wave number and L is the side length of a cube of the semiconductor material. We can write the DOS, g (E), as the number of states per unit energy per unit volume of real space, such that $g(E) = \frac{\partial N}{\partial E}$. It follows that the total number of states, N, is equal to degeneracy times the volume of a sphere in k-space divided by the volume occupied by one state (unit cell)

$$N = 2\frac{4fk^3}{3}\frac{1}{(2f/L)^3} = \frac{2}{3} \times \frac{4fk^3}{(2f)^3} \tag{2.10}$$

For electrons of spin $\frac{1}{2}$, the degeneracy is two for spin up and spin down. The DOS can be written as

$$g(E) = \frac{\partial N}{\partial k}\frac{\partial k}{\partial E} \tag{2.11}$$

where $\frac{1}{L^3}\times\frac{\partial N}{\partial k}=2\frac{4fk^2}{(2f)^3}$ and $E=\frac{\hbar^2|k|^2}{2m}$ therefore $\left|k=\sqrt{\frac{2mE}{\hbar^2}}\right|$

Then we differentiate eq. (2.10) with respect to the energy

$$dk=\frac{1}{2}\left(\frac{2mE}{\hbar^2}\right)^{-\frac{1}{2}}\left(\frac{2m}{\hbar^2}\right)dE \tag{2.12}$$

Thus the DOS in terms of energy for bulk material can be written as

$$g(E)_{3D}\,dE=\frac{k^2dk}{f^2}=\frac{2mE}{f^2\hbar^2}\left(\frac{2mE}{\hbar^2}\right)^{\frac{-1}{2}}\frac{m}{\hbar^2}dE=\frac{1}{2f^2}\left(\frac{2m}{\hbar^2}\right)^{\frac{3}{2}}E^{\frac{1}{2}}dE \tag{2.13}$$

To understand the concept of Fermi energy and the distribution of electrons and holes in a semiconductor, let us first assume that the semiconductor is intrinsic, which means that the number of electrons in the conduction band is equal to the number of holes in the valence band. The DOS for both the conduction and valence bands for an intrinsic semiconductor can be written as follows

$$g_e(E)_{3D}=M_c\frac{\sqrt{2(E-E_c)(m_e^*)^3}}{f^2h^3} \tag{2.14}$$

$$g_h(E)_{3D}=M_v\frac{\sqrt{2(E_v-E)(m_h^*)^3}}{f^2h^3} \tag{2.15}$$

Where the subscripts e and h stand for electrons and holes, respectively and M_c and M_v are the number of equivalent minima in the conduction and valence bands respectively and m_e^* is the density-of-state effective mass for electrons. $m_e^*=(m_1^*m_2^*m_3^*)^{\frac{1}{3}}$ and m_h^* is the density-of-states effective mass for holes. Where m_1^*, m_2^*, m_3^* are the effective masses along the principal axes of the ellipsoidal

energy surface, for example, in case of Silicon we have three fold degeneracy. Therefore we can write $m_e^* = (m_l^* m_t^{*2})^{\frac{1}{3}}$ where m_l^* is the longitudinal effective mass and m_t^* is the transverse effective mass. Similarly in case of valance band in case of Silicon we can write $m_h^* = (m_{lh}^{*\frac{3}{2}} + m_{hh}^{*\frac{3}{2}})^{\frac{2}{3}}$ where m_{lh}^* is the light hole mass and m_{hh}^* is the heavy hole mass in the valence band and E_c and E_v are the bottom and top of the conduction and valence bands, respectively.

$$n_0 = M_c \int_{E_c}^{\infty} f_{FD}(E) g(E) dE = M_c \int_{E_c}^{\infty} \frac{g(E)dE}{1+e^{\left(\frac{E-E_F}{k_BT}\right)}} = \frac{M_c}{2f^2}\left(\frac{2m_e^*}{\hbar^2}\right)^{\frac{3}{2}} \int_{E_c}^{\infty} \frac{\sqrt{E-E_c}\,dE}{(1+e^{\frac{(E-E_F)}{k_BT}})} \tag{2.16}$$

Where n_0 is the electron density. Similarly we can calculate the hole density

$$p_0 = M_v \int_{-\infty}^{E_v} f_{FD}(E) g(E) dE = M_v \int_{-\infty}^{E_v} \frac{g(E)dE}{1+e^{\left(\frac{E_F-E}{k_BT}\right)}} = \frac{M_v}{2f^2}\left(\frac{2m_h^*}{\hbar^2}\right)^{\frac{3}{2}} \int_{-\infty}^{E_v} \frac{\sqrt{E_v-E}\,dE}{(1+e^{\frac{(E_F-E)}{k_BT}})} \tag{2.17}$$

Considering $(E-E_F) >> kT$, the eq. (2.16) and (2.17) can be solved using

$$\int_0^{\infty} x^{\frac{1}{2}} e^{-ax} dx = \frac{\sqrt{f}}{2a\sqrt{a}} \tag{2.18}$$

Thus Eq. (2.16) gives the effective density of states in the conduction band

$$N_c = M_c \frac{1}{4}\left(\frac{2m_e^* k_B T}{f\hbar^2}\right)^{\frac{3}{2}} \tag{2.19}$$

Similarly Eq. (2.17) gives the effective density of states for the valence band

$$N_v = M_v \frac{1}{4}\left(\frac{2m_h^* k_B T}{f\hbar^2}\right)^{\frac{3}{2}} \tag{2.20}$$

when $(E_c - E_F) >> kT$, we can write the thermal equilibrium electron concentration in terms of the effective density of states of the conduction band and the separation between the Fermi level and the conduction band edge, E_c as:

$$n_0 = M_c\, N_c\, e^{\frac{-(E_c - E_F)}{k_B T}} \tag{2.21}$$

Similarly when $(E_F - E_v) >> kT$ we can write:

$$p_0 = M_v\, N_v\, e^{\frac{-(E_F - E_v)}{k_B T}} \tag{2.22}$$

The law of mass action states $n_0 p_0 = n_i^2$; where n_i is the intrinsic carrier concentration, which can be written as

$$n_i = \sqrt{n_0 p_0} = \frac{\sqrt{M_c M_v}}{4} \left(\frac{2\sqrt{m_h^* m_e^*} k_B T}{f\hbar^2} \right)^{\frac{3}{2}} e^{\frac{-E_g}{2k_B T}} \tag{2.23}$$

Where $E_g = E_c - E_v$ is the band gap energy.

Table 2.1 shows the effective masses, effective density of states for the conduction and valence band and the intrinsic carrier concentration for GaAs, GaSb, InSb, Ge and Si at 300K. In the case of Si the 3 fold valley degeneracy was considered. In the case of the valence band, only heavy and light hole bands were considered as the spin orbit band is sufficiently shifted, it can be ignored [2].

	m_c	m_v	E_g	M_c	M_v	N_c (cm^{-3})	N_v (cm^{-3})	$n_i = N_c N_v e^{-qEg/2kT}$ (cm^{-3})
GaAs	0.067	0.5	1.43	1	2	4.35E+17	8.86E+18	1.96E+06
GaSb	0.042	0.23	0.73	1	2	2.16E+17	2.76E+18	5.77E+11
InSb	0.014	0.4	0.18	1	2	4.15E+16	6.34E+18	1.58E+16
Ge	1.64	0.19	0.67	4	2	5.26E+19	2.08E+18	2.49E+13
Si	0.37	0.82	1.11	3	2	1.69E+19	5.58E+19	1.49E+10

Modelling of the impact of the PV cell characteristics depends largely on the calculation of J_0-values for each cell. Typically such modelling utilizes the thermodynamic limit of J_0 or an empirical equation depending on the bandgap energy as discussed in the following using the law of mass action and assuming $N_a = p_p$ and $N_D = n_n$. Recalling eq. (2.3) J_0 can be written as

$$J_0 = n_i^2 q\left(\frac{D_n}{L_n N_A} + \frac{D_p}{L_p N_D}\right) \tag{2.24}$$

Substituting the value of n_i from Eq. 2.23 we get

$$J_0 = \frac{qM_c M_v}{2}\left(\frac{\sqrt{m_h^* m_e^*}k_B T}{f\hbar^2}\right)^3\left(\frac{D_n}{L_n N_A} + \frac{D_p}{L_p N_D}\right)e^{\frac{-E_g}{k_B T}} \tag{2.25}$$

In the above equation n_i is the intrinsic carrier concentration E_g is the bandgap of the material, D_n and D_p are the electron and hole diffusion coefficients, L_n and L_p are the electron and hole diffusion lengths in the p and n regions respectively. Thus the dark current in a semiconductor device depends strongly on its intrinsic carrier concentration.

Figure 2.3 represents the Arrhenius plot of intrinsic carrier concentration for bulk GaAs, Si, GaSb, Ge, InSb as a function of inverse temperature using the Eq.(2.23). In the cases of Ge and Si the 4 and 3 fold conduction band valley degeneracy were considered respectively. For the valence band the heavy and light hole bands are considered as the spin orbit band is sufficiently shifted so it can be ignored [2].

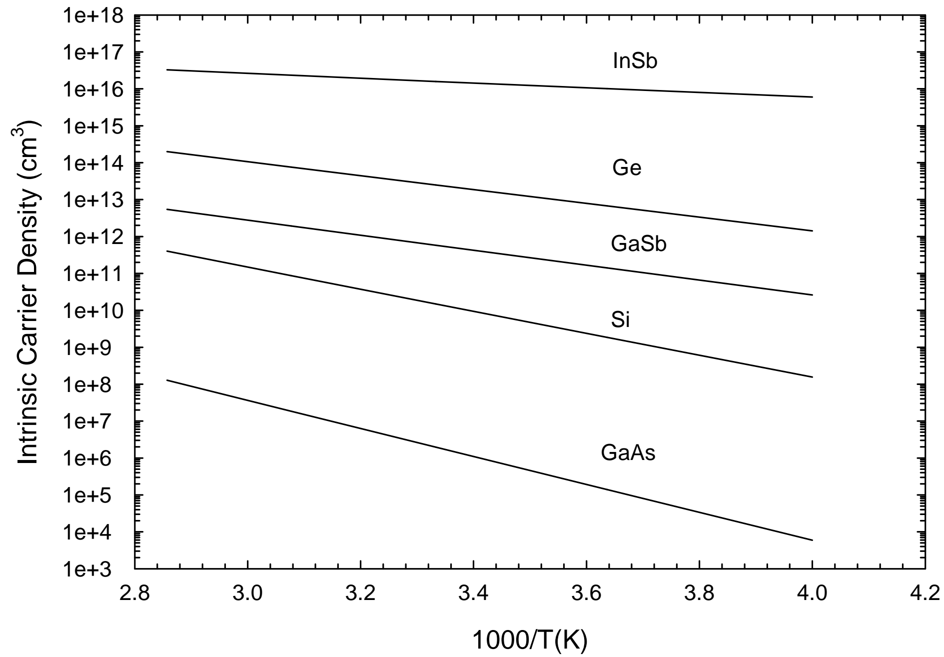

Figure 2.3: Arrhenius plot of intrinsic carrier concentration for bulk GaAs, Si, GaSb, Ge, InSb as a function of inverse temperature. For Ge and Si the 4 and 3 fold conduction band valley degeneracy were considered respectively. For the valence band only heavy and light hole band were considered as the spin orbit band is sufficiently shifted so it can be ignored [2].

2.4 Quantum Well Physics

Quantum wells are one example of heterostructures - structures made by joining different materials, usually in layers, and with the materials joined directly at the atomic level. A quantum well is a particular kind of heterostructure in which

one thin "well" layer is surrounded by two "barrier" layers. A type I well in which both electrons and holes are confined, is so thin that the fact that the electron and hole are both waves can not be ignored. In fact, the allowed states in this structure correspond to wave function in the direction perpendicular to the layers. Because only particular wave functions are allowed, the system is quantized. Multiple Quantum Well (MQW) materials can be made to a high degree of precision by modern epitaxial crystal growth techniques such as molecular beam epitaxy (MBE). MBE growth is discussed in Chapter 4. Many of the physical effects in quantum well structures can be seen at room temperature and can be exploited in real devices. We can understand the basic properties of a quantum well through the simple "particle-in-a-box" model. Here we consider Schrödinger's equation in one dimension

$$\frac{-\hbar^2}{2m}\frac{\partial^2 \Psi_n(x)}{\partial x^2} + V(x)\Psi_n = E_n \Psi_n(x) \tag{2.26}$$

where $V(x)$ is the structural potential (i.e., the "quantum well" potential) seen by the particle along the direction of interest (x), m is the particle's (effective) mass, E_n and Ψ_n are the eigenenergy and eigenfunction associated with the solution(s) to Eq. (2.26). The solution of the problem of an actual quantum well with finite barrier height is a straightforward mathematical exercise. It does, however, require that we choose boundary conditions to match the solutions in the well and the barriers. One boundary condition is obvious, which is that the wave function must be continuous at the edges of the well and the electron is localized. A second boundary condition is continuity of the wave function derivative across the boundary. With these boundary conditions and

the decay of the wave function to zero at $x = \pm\infty$ the finite potential square well problem as shown in Figure 2.4 is solved.

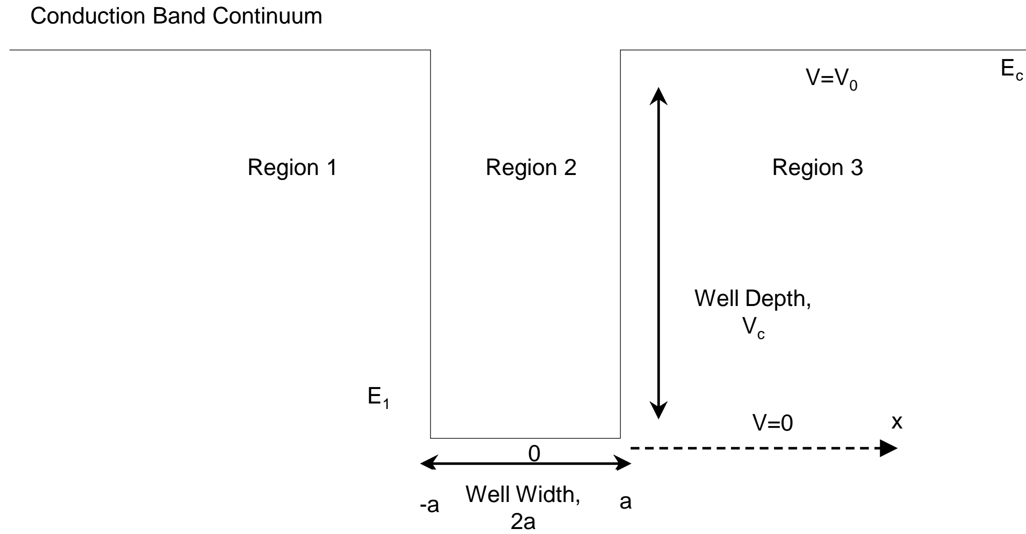

Figure 2.4: Quantum well (2D) with finite height of barriers.

We expect waves inside the well and an imaginary wave vector (yielding exponentially decaying probability of finding the particle) in the outside regions. For Figure 2.4 Eq 2.26 can be written as

$$\frac{\partial^2 \Psi(x)}{\partial x^2} + \frac{2m}{\hbar^2}\left[E - V(x)\right]\Psi(x) = 0 \tag{2.27}$$

The solution of the Schrödinger's equation $\Psi(x) = U(x)e^{ikx}$ where $U(x)$ is the Bloch function and k is the wave number. Let us consider the left side barrier as Region 1, $x \leq -a$, $V(x) = V_0$, for this region the wave function can be written as

$\text{Œ}_I = Ae^{\text{s}x}$ and $\frac{\partial^2 \text{Œ}_I}{\partial x^2} = \text{s}^2 \text{Œ}_I$ with $\text{s} = \sqrt{\frac{2m(V_0 - E)}{\hbar^2}}$. The equation makes it clear that we have exponential decay. The same equation can be used for Region 3 the right side of the well $x \geq a$, $V(x) = V_0$, $\text{Œ}_{III} = De^{-\text{s}x}$. For Region 2, inside the well, $-a \leq x \leq a$ $V(x) = 0$, so for this region. $\text{Œ}_{II} = B\sin \text{r}x + C\cos \text{r}x$. where $\text{r} = \sqrt{\frac{2mE}{\hbar^2}}$. There are even and odd parity solutions, $\text{Œ} = C\cos(\text{r}x)$ for even parity solutions and $\text{Œ} = D\sin(\text{r}x)$ for odd parity solutions. As the boundary conditions apply we need to match both the wave function magnitude, $\text{Œ}(x)$ and its derivative, $\frac{\partial \text{Œ}(x)}{\partial x}$ at the well boundaries, namely at $x = \pm a$ by utilizing the boundary condition such as $\text{Œ}_I(x = -a) = \text{Œ}_{II}(x = -a)$, $\frac{\partial \text{Œ}_I(x = -a)}{\partial x} = \frac{\partial \text{Œ}_{II}(x = -a)}{\partial x}$, the same applies for $x = +a$. Doing the calculation twice, since we have even and odd parity solutions, in Region II for $B = 0$, $\text{Œ}_{II} = C\cos(\text{r}x)$ and for $C = 0$; $\text{Œ}_{II} = -B\sin(\text{r}x)$ at $x = a$ equating Œ and $\frac{\partial \text{Œ}}{\partial x}$ for even parity we get $\frac{\text{s}}{\text{r}} = \tan\left(\frac{\text{r}a}{2}\right)$ and for odd parity we have $\frac{\text{s}}{\text{r}} = -\cot\left(\frac{\text{r}a}{2}\right)$. The above equations are transcendental equations and the energy, E, is the only unknown. Transcendental equations need to be solved graphically and we can do that by defining $\} = a\sqrt{\frac{2mE}{\hbar^2}}$ and $\sim = a\sqrt{\frac{2m(V_0 - E)}{\hbar^2}}$ Note that $\}^2 + \sim^2 = R^2$

where $R = \sqrt{\frac{2mV_0}{\hbar^2}} a$, a parameter that is independent of energy. R represents the depth and width of the QW as well as the effective mass of the confined electron or hole.

Figure 2.5. Shows solutions of the transcendental equation for a finite quantum well for different values of R.

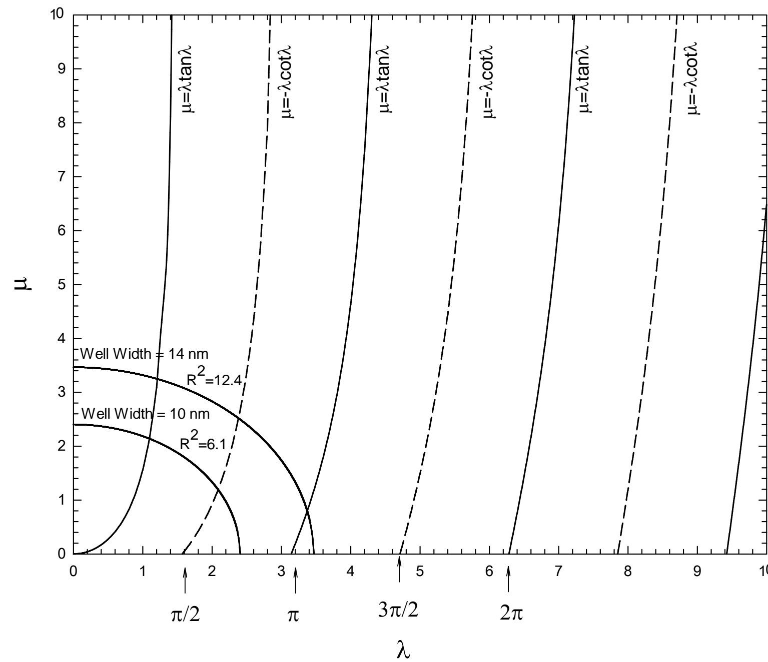

Figure 2.5: Solutions of finite potential well problem are at the intersections of the semi-circles and the trigonometric functions.

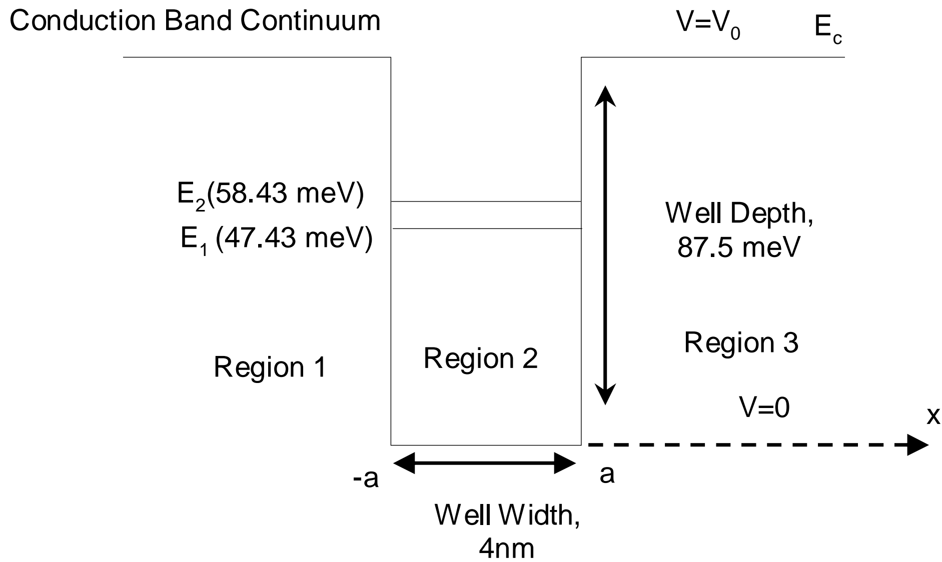

Figure 2.6: A 4 nm wide Quantum well (2D) having effective mass $0.11m_0$ with finite height rectangular potential barrier and wells showing the normal and oblique valley sub band.

Figure 2.6 was plotted for a 4 nm wide quantum well having a well depth of 87.5 meV showing the calculated normal and oblique valley band energies for the conduction band quantum well to be 47.43 meV and 58.43 meV. The effective mass value considered for this calculation is $0.11m_0$

The difference between the multiple quantum well and a super lattice structure is that if there is significant wave function penetration between the wells, causing the phenomena of mini bands. The mini bands arise when quantum wells are put very close together in a regular way.

2.5 Fermi Dirac Distribution Function in Quantum Well Materials

Figure 2.7 was plotted using the Eq. 2.8 Fermi Dirac distribution function for 250K, 300K and 350K in a multiple quantum well structure

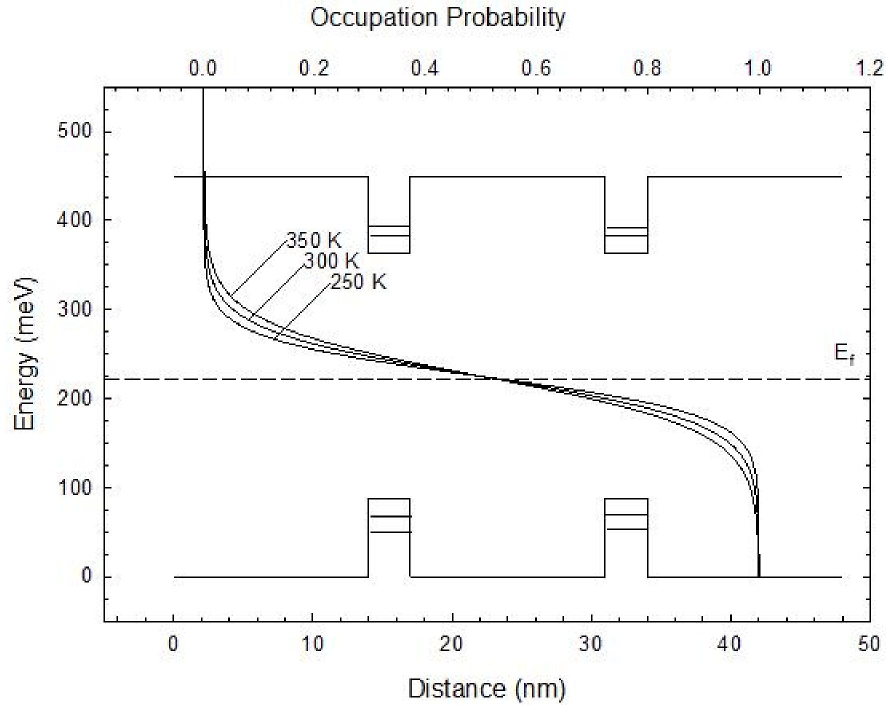

Figure 2.7: The Fermi Dirac distribution at 250K, 300K and 350 K for a multiple quantum well structure having 275 meV bandgap for the well and 450 meV bandgap for the barrier.

Figure2.7 graphically summarizes occupation probability of charge carriers (electrons and holes) in a MQW structure as predicted by Fermi Dirac distribution at 250K, 300K and 350 K for a semiconductor having 275 mev bandgap well and 450 meV bandgap barrier.

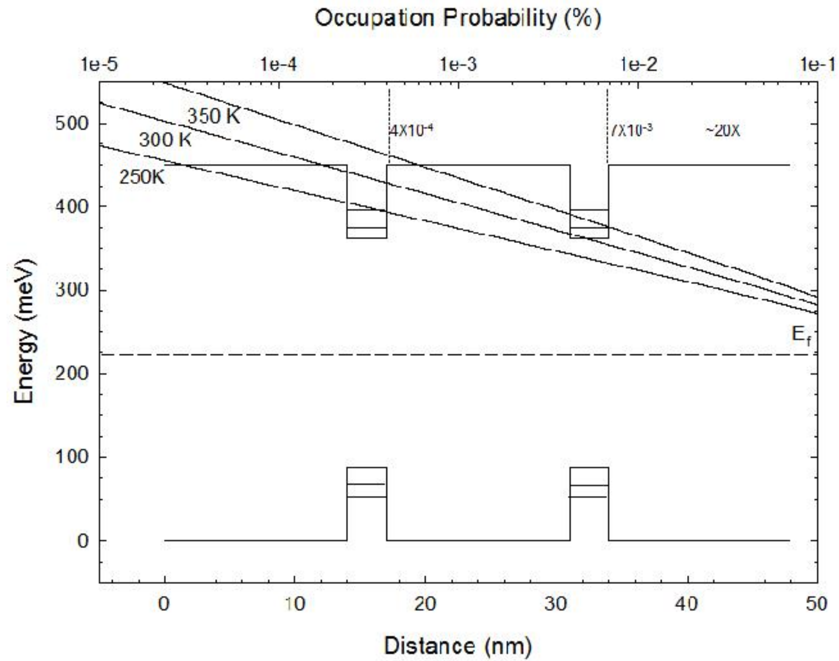

Figure 2.8: Expanded view of the Fermi Dirac distribution at 250K, 300K and 350K for a multiple quantum well structure having 275 meV bandgap well and 450 meV bandgap barrier.

The above figure explains the expanded view near the conduction band energy showing the expanded plot of Fermi Dirac distribution function of electrons in the conduction band at 250K, 300K and 350K for a MQW structure of barrier band gap energy 450 meV and well band gap energy 275 meV. Note that the probability of electron occupation of allowed states in the MQW subbands increases 20 times as the temperature rises from 250K to 350K.

2.6 Density of States and Intrinsic Carrier Concentration in Quantum Well Materials

In a 2D system like a quantum well (QW) structure we get a series of energy levels and associated sub bands due to the quantization of electrons in the direction of the QW thickness [7]. In a quantum well, the electrons and holes are still free to move in the directions parallel to the layers; hence, we do not really have discrete energy states for electrons and holes in quantum wells; we have instead sub bands that start at the energies calculated for the confined states. The electron in a given confined state can, in addition, have any amount of kinetic energy for its in-plane motion in the quantum well. The DOS in a quantum well system is restricted to the $k_x k_y$ plane where the electrons or holes are now confined in this plane and their motion is restricted along the growth axis (z direction in the real space, or k_z direction in the momentum space). The total number of states per unit cross sectional area is given by the area in k-space divided by the area of the unit cell in k-space and divided by the area in real space.

$$g^{2D} = 2fk^2 \frac{1}{\left(\frac{2f}{a}\right)^2} \frac{1}{L^2} = 2\frac{fk^2}{(2f)^2} \tag{2.28}$$

Where 2 = spin degeneracy of electrons, $\left(\frac{2f}{a}\right)^2$ = area of the two dimensional unit cell in k-space, a^2 = real space area of the well. The density of state can be expressed as

$$g^{2D}(E) = \frac{\partial N^{2D}}{\partial E} = \frac{\partial N}{\partial k}\frac{\partial k}{\partial E} = \left(\frac{k}{f}\right)\left(\frac{2m^*}{\hbar^2}\right)^{\frac{1}{2}} \frac{1}{2\sqrt{E}} = \frac{m_e^*}{f\hbar^2} \tag{2.29}$$

where m_e^* and $\hbar$ are the effective mass of electrons and Planck's constant respectively. The DOS for motion in the plane of the quantum well layers thus turns out to be constant with energy, as mentioned before, the DOS for a given sub band really is a step that starts at the appropriate confinement energy. If there is more than one confined state in the quantum well system, the DOS at a given energy is the sum over all sub bands below that particular energy. Taking into account the other energy levels in the quantum well, the DOS (per unit energy and area) of such confined electrons in a single quantum well (SQW) structure can be written as

$$g_e^{2D}(E) = \sum_{n=1}^{\infty} \frac{m_e^*}{f\hbar^2} H\left[E - \vee_n\right] \tag{2.30}$$

where $H(x)$ and $\vee_n$ are the Heaviside function and the quantized energy level of electrons in the nth sub band of the QW respectively. Utilizing the Maxwell-Boltzmann distribution, the electron and hole densities in a 2D semiconductor can be easily calculated at equilibrium by integrating the product of Eqs. (2.8) and (2.29):

In 2D quantum wells shown in Figure. 2.4, the total number of electrons $\left(n^{2D}\right)$ within a sub band is given as when $E_f = E_i$

$$n_i^{2D} = \int_{Subband} g^{2D}(E) f_{FD}(E) dE = \int_{E_j}^{\infty} \frac{m^*}{f\hbar^2} \frac{dE}{e^{\left(\frac{E-E_F}{k_B T}\right)} + 1} \tag{2.31}$$

The Fermi Dirac distribution function can be approximated by the Maxwell-Boltzmann function for $\left(E_c - E_F\right) >> k_B T$ where E_c is the bottom of the conduction band [9]. This implies that $E_f = E_i$ we can write $E_j = e^{\frac{E-E_F}{k_B T}} >> 1$. Assuming

$x = e^{\frac{(E-E_F)}{k_B T}}$; therefore $\partial x = \frac{x}{k_B T} \partial E$ and $x_j = e^{\frac{(E_i - E_F)}{k_B T}}$, inserting this assumption into eq. (2.31) we get

$$n_i^{2D} = \frac{m^* k_B T}{f\hbar^2} \int_{x_j}^{\infty} \frac{dx}{(x+1)x} \tag{2.32}$$

Integrating by parts yields

$$\int \frac{dx}{(x+1)x} = -\ln\left(1 + \frac{1}{x}\right) \tag{2.33}$$

Substituting back the value of x in eq. (2.31) and rearranging we get the density of electrons in j^{th} sub band and assuming the effective mass is same for all the sub bands we get

$$n_i^{2D} = \frac{m^* k_B T}{f\hbar^2} \left[-\ln\left(1 + \frac{1}{x}\right) \right]_{x_j}^{\infty} = \frac{m^* k_B T}{f\hbar^2} \ln\left(1 + \frac{1}{x_1}\right) = \frac{m^* k_B T}{f\hbar^2} \ln(1 + e^{\frac{(E_F - E_j)}{k_B T}}) \tag{2.34}$$

Thus by substituting $E_f = \frac{E_g}{2}$ in eq. (2.34) and summing for n^{th} bound sub bands in the quantum well we have

$$n_i^{2D} = \sum_{j=1}^{n} n_i^{2D} = \frac{m^* k_B T}{f\hbar^2} \sum_{j=1}^{n} \ln(1 + e^{(\frac{\frac{E_g}{2} - E_j}{k_B T})}) \tag{2.35}$$

where E_1, E_2 ,….are the energy states in the quantum well. Immediately, as the top of the energy-gap is reached, there is a significant number of available states. Our calculations show there is over eighty times less occupation from energy level E_1 to energy level E_5 so calculation of further energy states to infinity becomes insignificant.

The possible reduction of thermal loss is of great interest for future low bandgap TPV cells. The following is an example of GaAs and how we can reduce the intrinsic carrier concentration by applying the quantum confinement technique. Figure 2.9 shows the QW density of states (the step functions) which was plotted using the data from Table 2.2 GaAs

$$\text{2D Density of States} = \frac{m^*}{f\hbar^2} = \frac{(m^*/m_0)(m_0c^2)4f}{(hc)^2} = \frac{4f\,(0.067)*51100ev}{(1240nm*eV)^2}\left(\frac{10^9 nm}{m}\right)^2 =$$

$$2.8\times10^{17} m^{-2}eV^{-1}\times\left(\frac{1eV}{1000meV}\right)\left(\frac{1m}{100cm}\right)^2 = 2.8\times10^{10} cm^{-2}meV^{-1} \qquad (2.36)$$

Energy for Infinite well

$$E_n = \frac{f^2\hbar^2n^2}{2m^*L^2} = \frac{(hc)^2n^2}{8m^*c^2L^2} = \frac{(1240nmeV)^2n^2}{8(0.067)*511{,}000eV*(7nm)^2} = (115meV)n^2 \qquad (2.37)$$

where n is the quantized energy level of the charged carriers and L is the width of the quantum well.

Table 2.2: Density of States and energy values for GaAs.

m^* (kg)	E (meV)	$g^{2D}(meV^{-1}cm^{-2})$
$0.067*m_0$	115	2.80E+10
$0.067*m_0$	460	5.60E+10
$0.067*m_0$	1035	8.40E+10

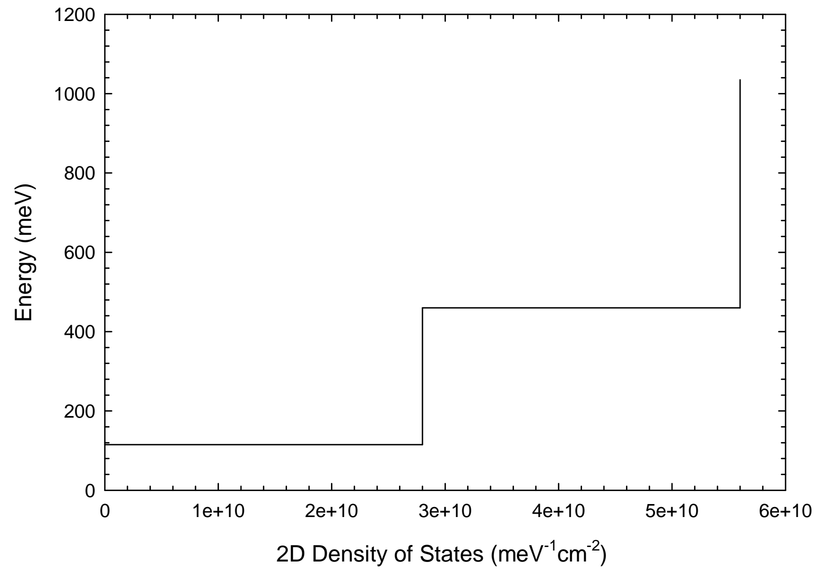

Figure 2.9: Density of states per unit area and energy for a 2-D, 7 nm quantum well with finite barriers where $m^*/m_0 = 0.067$.

Data in Figure 2.9 are in agreement with published results [8]. Dividing by the product of energy and 2D DOS by the well width gives a carrier concentration per cubic centimeter which is similar to the density of states in a bulk semiconductor

2.7 Summary & Conclusion

In this Chapter the correlation between intrinsic carrier density, dark current density and open circuit voltage for TPV device materials were explained. The Fermi Dirac distribution of the carriers and how the carrier concentration changes with temperature for both bulk and quantum well materials discussed. How the carrier effective mass in different valleys plays a role in the concentration of intrinsic carrier

density were described. Good agreement was found in calculations of multi valley materials like Si & Ge. Chapter 2 creates the foundation for the calculations of Chapter 3.

References:

[1] Würfel P (1995) Physik der Solarzellen (in German), 2nd edn. Spektrum Akademischer Verlag, Heidelberg.

[2] Sze SM (1981), Physics of semiconductor devices, 2nd edn. Wiley, New York.

[3] Omar, Manasreh, (2005)" Semiconductor Heterojunctions and Nanostructures", the McGraw-Hill Companies.

[4] Y. Xu, A. Shakouri, A, Yariv, T. Krabach and S. Dejewski," Direct measurement of doping density and barrier lowering effect with bias in quantum wells" Electronics Letters 16th February 1995 Vol. 31 No.4.

[5] C. Kittel, Introduction to Solid State Physics, Vol. 7. Wiley NewYork, 1976

[6] Burt M G, 1992, the justification for applying the effective-mass approximation to microstructures, J. Phys: Condens. Matter Vol. 4 6651.

[7] E.E. Mendez, K. von Klitzing (1987)" Physics and Applications of Quantum Wells and Superlattices", Springer.

[8] Fedor T. Vasko, Alex V. Kuznetsov (1999), "Electronic States and Optical Transitions in Semiconductor Heterostructures" Springer.

[9] W. Z. Shen, H. F. Yang, L. F. Jiang, K. Wang, and G. Yu, H. Z. Wu and P. J. McCann," Band gaps, effective masses and refractive indices of PbSrSe thin films: Key properties for mid infrared optoelectronic device applications" J. Appl. Phys., vol. 91, no. 1, pp. 3319–3327, Jan. 2002.

Chapter 3

Density of States and Intrinsic Carrier Concentrations in IV-VI Semiconductor Bulk and Quantum Well Materials

Nothing is more practical than a good theory
Kurt Lewin

3.1 Introduction

IV-VI semiconductor materials are potentially useful for fabrication of improved TPV devices. They can have band gaps that are considerably smaller than most III-V semiconductors so they can cover more of the long wavelength portion of the thermal spectrum. Unlike III-V materials, lead chalcogenides IV-VI semiconductor materials have a direct band gap with nearly symmetric conduction and valence bands which are located at the four equivalent L-points in the Brillouin zone.

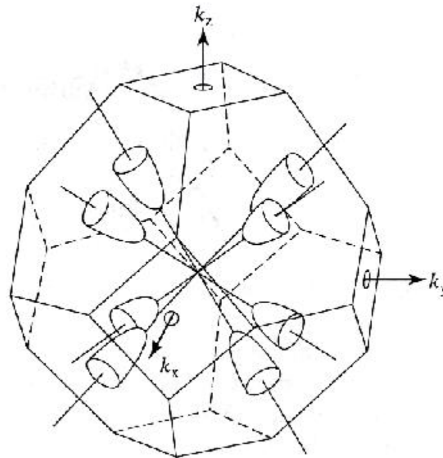

Figure 3.1 The surface of constant energy in k-space for lead salt materials eight half ellipsoids of revolution centered at the L points on the first Brillouin zone boundary [1].

The constant energy surfaces are prolate ellipsoids of revolution characterized by the longitudinal and transverse effective masses m_l^* and m_t^* respectively (Fig 3.1). Lead chalcogenides possess an extremely large bulk exciton Bohr radius (e.g. PbS 20 nm and PbSe 46 nm), which allows their bandgap and absorption edge to be tuned across the entire infrared spectrum. Composition dependence of the bandgap is not too strong, so it is possible to obtain a quite homogenous semiconductor for any given spectral range. The electronic band structure of IV-VI semiconductor compounds can be varied between 0 - 800 meV at the L-point of the Brillouin zone by changing the alloy composition and temperature. The major axes of the ellipsoids of a IV-VI material as shown in Fig. 3.1 are in the [111] directions. These semiconductors have the face centered cubic crystal structure with (100) cleavage planes because the conduction and valence bands at the L points are near mirror images of each other, the electron-and hole effective masses are nearly equal. The band gap temperature tuning coefficient is about 10 times larger than that for III-V materials, so IV-VI diode detectors can be tuned over a broad spectral range by changing the heat sink temperature. Because of their band structure properties photons can be efficiently absorbed due to direct interband transitions, are an ideal choice for fabrication of optoelectronic devices covering the mid-infrared region of the electromagnetic spectrum (3 μm to 30 μm) [2-5]. In this chapter calculation of effective masses and intrinsic carrier concentration for bulk and MQW $PbSe/Pb_{0.93}Sr_{0.07}Se$, $PbSe/Pb_{0..90}Sr_{0.10}Se$ and $PbSe/Pb_{0.87}Sr_{0.13}Se$ where $PbSe$ is the well and $Pb_{1-x}Sr_xSe$ is the barrier in the QW material.

3.2 Effect of temperature on IV-VI bulk and quantum well semiconductor material

Temperature affects the properties of electronic systems in a number of fundamental ways. The most fundamental of properties is the energy band gap, E_g, which is affected by temperature according to the Varshni equation [6].

$$E_g(T) = E_g(0) - \frac{r_E T^2}{T + s_E} \tag{3.1}$$

Where $E_g(0)$ is the band gap energy at absolute zero on the Kelvin scale in the given material, and r_E and s_E are material specific constants. The positive temperature coefficient of the band gap in lead chalcogenides, unlike many common semiconductors, is favorable for TPV materials. An increasing gap with temperature can act to suppress bipolar effects caused by intrinsic carrier activation. The temperature dependent gap in Pb_x is known to be due to both lattice expansion and electron-phonon interactions [7]. Considering the thermodynamic role of the band gap as chemical potential for the mass action law and taking into account the entropy contributions the temperature coefficient the effect can be described by $\frac{dE_g}{dT} = \left(\frac{dE_g}{dT}\right)_V + \frac{3r_L}{K}\left(\frac{dE_g}{dP}\right)_T$, where r_L is the linear thermal expansion coefficient $\left(\frac{1}{L}\left(\frac{dL}{dT}\right)_P\right)$, K is the bulk modulus $\left(\frac{-1}{V}\left(\frac{dV}{dP}\right)_T\right)$, $\left(\frac{dE_g}{dT}\right)_V$ describes the electron -phonon interactions and $\left(\frac{dE_g}{dP}\right)_T$ describes the bandgap dependent pressure [8].

The band gap of the PbSe well system is directly dependent on temperature as shown in the following Eq. (3.2) [9]

$$E_g(T) = 125 - 1021x + \sqrt{400 + 0.256T^2}\,(meV) \qquad (3.2)$$

Where T is the temperature, while the energy gap of $Pb_{1-x}Sr_xSe$ barrier system depends on temperature according to eq. (3.1) [2, 10]

$$E_g(x,T) = 0.150 + 3.608x - 1.314x^2 + (0.430 - 3.093x + 6.495x^2)\times 10^{-3}T(eV) \qquad (3.3)$$

$(0 \le x \le 0.276, 0, T \le 350K)$, where x is the Sr content and T is the temperature. In this study the non-parabolicity effects of the barrier material are ignored. The difference in the energy gaps between the well material and the barrier material is assumed to be equally divided between the conduction and valence bands, the conduction and valence-band effective masses in the well are assumed equal and the effective masses of the carriers outside the well are assumed to be constant.

3.3 Effective mass in IV-VI bulk and quantum well semiconductor material

In comparison to III-V semiconductor materials, low-dimensional IV-VI semiconductor such as PbSe, PbTe, and related alloys are relatively unexplored materials systems. IV-VI semiconductors have unique band structure properties that are quite different from III-V semiconductor materials. The conduction and valence bands are nearly symmetric and the valence band does not have a degenerate heavy-hole band. This last property is responsible for the much lower Auger recombination coefficients for bulk IV-VI materials [11] as compared to narrow band-gap III-V semiconductors [12]. The constant energy surfaces for electrons and holes in the

conduction and valence bands are prolate ellipsoids of revolution characterized by longitudinal and transverse effective masses. m_L and $m_‡$ respectively. The E-k relationship represents parabolic bands in the z-direction near the band edge can be written as $E_z = \frac{\hbar^2 k^2}{2m^*}$. However, away from the band edge the bands are non-parabolic. The dispersion relation for non-parabolic bands can be analyzed by using Luttinger-Kohn and the energy- dependent effective mass the effect of which is insignificant for TPV application. Hence for this dissertation the band structure of the barrier material is considered parabolic with a constant effective mass to simplify the calculations. For a quantum well in the [100] direction, the value of the well effective mass at the band extrema, m_w is calculated from the respective carrier longitudinal m_l and transverse m_t masses using the same methodology as Partin [13]. The dot product between the [100] direction and the [111] ellipsoid direction is given by the angle „ , [100] [111] =1= $\sqrt{3}\cos „$; $\cos „ = \frac{1}{\sqrt{3}}$ and $\sin „ = \frac{2}{\sqrt{3}}$. Following Partin [13] we can calculate the effective mass in the [100] direction

$$\frac{1}{m_w} = \frac{1}{3}\left[\frac{2}{m_t} + \frac{1}{m_l}\right] = \frac{1}{m_{100}} \tag{3.4}$$

This value for the effective mass is in the direction of the well, not in the direction of the ellipsoid major axis [111]. Substituting for this effective mass value in Schrödinger's eq. for effective mass the discrete energy levels can be found for parabolic bands. For QW structures grown on (100) oriented substrates, each of the four L-valleys along the (111) directions lies at the same angle with respect to the

direction of potential variation, so electrons and holes in each valley have the same effective mass [14]. Radiative recombination occurs between sub-bands, with relatively large densities of states due to the four fold degenerate energy levels in IV-VI semiconductor. This situation explains the decreases in threshold currents for QW laser structures but can be of significant advantage for a TPV device as it will increase the electron lifetime in the conduction band. QW materials grown on (111) oriented substrates. On the other hand, can provide a band structure that is more desirable for semiconductor device fabrication. In this case one of the L-valleys will be normal to the substrate surface. and the other three valleys will be at oblique angles to the substrate surface, Two different effective masses will thus exist for potential variation along the [111] direction [14].

$$m_{111}^{longitudinal} = m_L \tag{3.5}$$

and $$\frac{1}{m_{111}^{oblique}} = \frac{1}{9}\left[\frac{8}{m_{\ddagger}} + \frac{1}{m_L}\right] \tag{3.6}$$

The two different masses remove L valley degeneracy, placing the longitudinal valley (normal to substrate surface) at a slightly lower energy than the three degenerate oblique valleys. With an approximate four fold reduction in density of states intrinsic carrier concentration can be reduced significantly for a single L-valley enabling significant reductions in dark current. It is thus useful to consider the properties of IV-VI semiconductor QWs grown on (l11) oriented substrates. The electronic band structures of IV-VI semiconductor QW materials grown on both (100) oriented and (111) oriented substrates have been studied using infrared transmission

spectroscopy. Ishida et al. [15 -16] and Yuan et al [17] saw that a QW sample had only one sub-band absorption edge of 314meV and no other absorption edges, which would indicate splitting of L valley degeneracy. McCann et al [18] have investigated thoroughly the electronic sub-band properties and effective masses of (111)-oriented IV-VI MQW materials and the energy level calculations for electrons and holes confined in IV-VI semiconductor using barrier heights obtained from the measured FTIR transmission spectra and the band structure parameters from [100] and [101] sub band energies were calculated by McCann et al [18] using the envelope wave function approximation. The temperature dependence of the four constant energy surface ellipsoids in IV – IV semiconductor materials is determined by using 300 K for the temperatures in Equation (3.2) and (3.3) substituting the resultant values into the following directionally dependent equations [9]. As discussed before IV-VI semiconductor materials that confine electrons and holes in the [111] direction can have two different types of L-valleys [3, 19-20]. using the Eqs (3.5) and (3.6) in conjunction with the numerical results of Eqs. (3.7-3.10), the effective mass values are calculated for the normal and oblique valley states in a single quantum well and displayed in Table 3.1. Assumptions in the calculations included equal conduction and valance band edge discontinuities ($\Delta E_c : \Delta E_v = 1:1$), a reasonable assumption based on the work of Yuan et al [17] and the same electron and hole effective masses in the barrier layers as those in the PbSe.

$$\frac{m_{cl}}{m_0} = \left(20.7\frac{E_g(0)}{E_g(T)} + 4.3\right)^{-1} \tag{3.7}$$

$$\frac{m_{vt}}{m_0} = \left(20.7\frac{E_g(0)}{E_g(T)} + 8.7\right)^{-1} \tag{3.8}$$

$$\frac{m_{cl}}{m_0} = \left(11.4\frac{E_g(0)}{E_g(T)} + 2.9\right)^{-1} \tag{3.9}$$

$$\frac{m_{vt}}{m_0} = \left(11.4\frac{E_g(0)}{E_g(T)} + 3.3\right)^{-1} \quad (3.10$$

Table 3.1 shows the effective masses for electrons and holes in PbSe and $Pb_{0.93}Sr_{0.07}Se$ barrier at 300K lattice temperature where free electron mass is $m_o = 9.11 \times 10^{-31}$ kg, l = longitudinal valley and o= oblique valley.

Table 3.1: Effective masses for electrons and holes in PbSe and $Pb_{0.93}Sr_{0.07}Se$.

Temp (300K)	E_g	m_e^l	m_e^o	m_h^l	m_h^o
PbSe	0.278eV	0.111m_o	0.061m_o	0.107m_o	0.052m_o
$Pb_{0.93}Sr_{0.07}Se$	0.45eV	0.145m_o	0.089m_o	0.143m_o	0.066m_o

3.4 Intrinsic Carrier Concentration in IV-VI bulk semiconductor material

Intrinsic carrier density for bulk (3D) $Pb_{1-x}Sr_xSe$ can be determined using Eq. (3.11)

$$n_i = \sqrt{n_0 p_0} = \frac{\sqrt{M_c M_v}}{4}\left(\frac{2\sqrt{m_h^*}\sqrt{m_e^*}k_B T}{f\hbar^2}\right)^{\frac{3}{2}} e^{\frac{-E_g}{2k_B T}} \tag{3.11}$$

Table 3.2 shows the effective masses (average between longitudinal and oblique valleys), effective density of states for the conduction and valence band and the intrinsic carrier concentration for PbSe, $Pb_{0.93}Sr_{0.07}Se$, $Pb_{0.90}Sr_{0.10}Se$ and $Pb_{0.87}Sr_{0.13}Se$ at 300K.

Table 3.2: Effective masses, effective density of states for the conduction and valence and the intrinsic carrier concentration for bulk PbSe, $Pb_{1-x}Sr_xSe$ (x=0.7,10,13 %).

	m_c	m_v	E_g	Valley Degeneracy	N_c (cm^{-3})	N_v (cm^{-3})	$n_i= N_cN_v e^{-qEg/2kT}$
PbSe	0.09	0.08	0.27	4	2.27E+18	2.27E+18	1.23E+16
$Pb_{0.93}Sr_{0.07}Se$	0.11	0.1	0.45	4	4.43E+18	4.43E+18	7.41E+14
$Pb_{0.90}Sr_{0.10}Se$	0.15	0.13	0.55	4	5.82E+18	5.82E+18	1.41E+14
$Pb_{0.87}Sr_{0.13}Se$	0.18	0.15	0.65	4	7.34E+18	7.34E+18	2.57E+13

Figure 3.2 shows the Arrhenius plot of Intrinsic carrier concentration for bulk PbSe, $Pb_{0.93}Sr_{0.07}Se$, $Pb_{0.90}Sr_{0.10}Se$ and $Pb_{0.87}Sr_{0.13}Se$ as a function of inverse temperature.

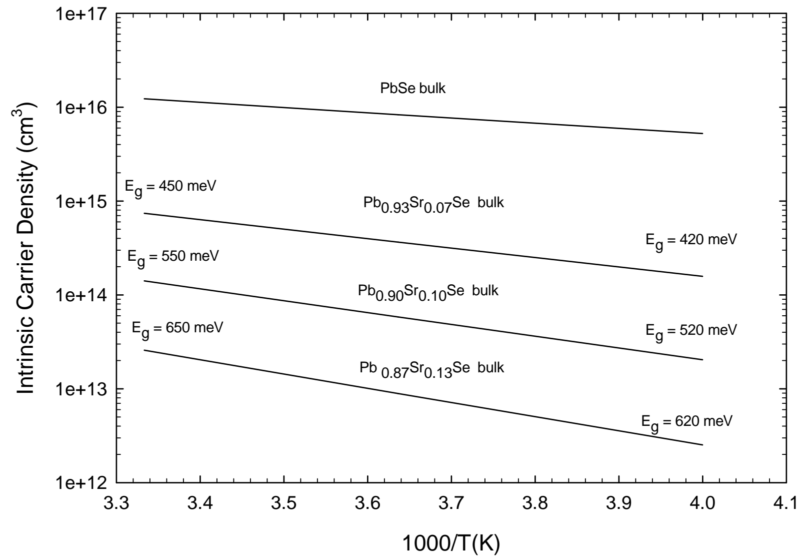

Figure 3.2 Arrhenius plot of Intrinsic carrier concentration for bulk PbSe, $Pb_{0.93}Sr_{0.07}Se$, $Pb_{0.90}Sr_{0.10}Se$ and $Pb_{0.87}Sr_{0.13}Se$ as a function of inverse temperature.

3.5 Intrinsic Carrier concentration in IV-VI QW Semiconductor Materials

In case of quantum well the two-dimensional reduced density of states can be determined using Equ. (3.12) where n is the total number of confined subbands in the quantum well, the reduced effective mass (determined from calculated values for the electron and hole given in Table 3.1), is Plank's constant, and H is a Heaviside step function with

$$g_e^{2D}(E) = \sum_{n=1}^{\infty} \frac{m_e^*}{f\hbar^2} H\left[E - \vee_n\right] \tag{3.12}$$

Quantized subband energy levels for 1,3,4,5, and 10 nm wide PbSe (bandgap = 275meV) QW confined by $Pb_{0.93}Sr_{0.07}Se$ (bandgap = 450 meV), $Pb_{0.90}Sr_{0.10}Se$ (bandgap = 550 meV) and $Pb_{0.87}Sr_{0.13}Se$ (bandgap = 650 meV) barrier layers were calculated using a time-independent, one- dimensional solution to Schrödinger's equation as discussed in Chapter 2 with equivalent band offsets for the conduction and valence band edge discontinuities (Ec: Ev = 1:1). Solutions took into account the two different effective masses for normal and oblique L-valley electrons and holes in the PbSe QW. As described above, growth on (111)-oriented substrates results in the four-fold L-valley degeneracy to be lifted in IV-VI quantum well structures, while growth on (110)-oriented substrates gives a partial lifting of the L-valley degeneracy. Knowledge of this phenomenon has allowed for the development of an accurate theoretical model for quantized energy levels in IV-VI quantum well materials based on solutions to the Schrödinger equation for finite quantum wells. Results of this

model are used to predict the band gap (i.e. material composition) and intrinsic carrier concentration required to reduce the dark current in the device.

Table 3.3 Shows the degeneracy split for PbSe $(E_g = 275meV)$ well and $Pb_{0.93}Sr_{0.07}Se$ $(E_g = 450meV)$ barrier having normal valley effective mass $0.11m_0$ and oblique valley effective mass $0.061m_0$ at 300K.

Table 3.3: The degeneracy split for PbSe well and $Pb_{0.93}Sr_{0.07}Se$ barrier.

m_o^*	m_n^*	Barrier Material Band gap (meV) $Pb_{0.93}Sr_{0.07}Se$	Well Material Band gap (meV) *PbSe*	Well Depth (meV)	Well Width (nm)	E_1^0 (meV)	E_1^n (meV)	$\Delta E = (E_1^o - E_1^n)$ (meV)
0.061* m_0	0.11* m_0	450	275	87.5	1	84.55	82.36	2.2
0.061* m_0	0.11* m_0	450	275	87.5	3	67.69	58.17	9.5
0.061* m_0	0.11* m_0	450	275	87.5	4	58.43	47.43	11.0
0.061* m_0	0.11* m_0	450	275	87.5	5	50.18	38.88	11.3
0.061* m_0	0.11* m_0	450	275	87.5	10	25.07	17.04	8.0

Table 3.4 shows the degeneracy split for PbSe $(E_g = 275meV)$ well and $Pb_{0.90}Sr_{0.10}Se$ $(E_g = 550meV)$ barrier having normal valley effective mass $0.11m_0$ and oblique valley effective mass $0.061m_0$ at 300K.

Table 3.4: The degeneracy split for PbSe well and $Pb_{0.90}Sr_{0.10}Se$ barrier.

m_o^*	m_n^*	Barrier Material Band gap (meV) $Pb_{0.90}Sr_{0.10}Se$	Well Material Band gap (meV) *PbSe*	Well Depth (meV)	Well Width (nm)	E_1^0 (meV)	E_1^n (meV)	$\Delta E = (E_1^o - E_1^n)$ meV)
$0.061*m_0$	$0.11*m_0$	550	275	137.5	1	130.39	125.33	5.1
$0.061*m_0$	$0.11*m_0$	550	275	137.5	3	122.8	105.9	16.9
$0.061*m_0$	$0.11*m_0$	550	275	137.5	4	78.68	60.92	17.8
$0.061*m_0$	$0.11*m_0$	550	275	137.5	5	65.20	48.23	17.0
$0.061*m_0$	$0.11*m_0$	550	275	137.5	10	29.42	19.33	10.1

Table 3.5 shows the degeneracy split for PbSe $(E_g = 275meV)$ well and $Pb_{0.87}Sr_{0.13}Se$ $(E_g = 650meV)$ barrier having normal valley effective mass $0.11m_0$ and oblique valley effective mass $0.061m_0$ at 300K.

Table 3.5: The degeneracy split for PbSe well and $Pb_{0.87}Sr_{0.13}Se$ barrier.

m_o^*	m_n^*	Barrier Material Band gap (meV) $Pb_{0.87}Sr_{0.13}Se$	Well Material Band gap (meV) *PbSe*	Well Depth (meV)	Well Width (nm)	E_1^0 (meV)	E_1^n (meV)	$\Delta E = (E_1^o - E_1^n)$ (meV)
$0.061*m_0$	$0.11*m_0$	650	275	187.5	1	174.59	165.77	8.8
$0.061*m_0$	$0.11*m_0$	650	275	187.5	3	117.97	93.92	24.1
$0.061*m_0$	$0.11*m_0$	650	275	187.5	4	94.51	70.87	23.6
$0.061*m_0$	$0.11*m_0$	650	275	187.5	5	76.43	54.86	21.6
$0.061*m_0$	$0.11*m_0$	650	275	187.5	10	55.3	43.7	11.6

Table 3.6 shows the degeneracy split for PbSe $(E_g = 275meV)$ well and $Pb_{0.93}Sr_{0.07}Se$ (bandgap = 450 meV), $Pb_{0.90}Sr_{0.10}Se$ (bandgap = 550 meV) and $Pb_{0.87}Sr_{0.13}Se$ (bandgap = 650 meV) barrier having normal valley effective mass $0.11m_0$ and oblique valley effective mass $0.07m_0$ at 300K.

Table 3.6: The degeneracy split for PbSe well and $Pb_{1-x}Sr_xSe$ barrier (x= 13, 22.5 & 27%).

MQW Intersub band Energy (meV)	m_n^*	m_o^*	Width (nm)	Depth (meV)	Barrier Height (meV)	Normal Valley (meV)	Oblique Valley (meV)	Degeneracy Splitting (meV)
450	0.13* m_0	0.07* m_0	3.0	188	651	87.6	109.3	21.7
550	0.13* m_0	0.07* m_0	2.5	321	917	137.8	174.8	37.1
650	0.13* m_0	0.07* m_0	2.0	385	1045	187.6	231.5	43.9

Fig 3.3 Shows the conduction band L-Valley degeneracy splitting energies for n=1 electrons for $PbSe(E_g = 275meV)$ well and $Pb_{0.87}Sr_{0.13}Se(E_g = 450meV)$ / $Pb_{0.775}Sr_{0.225}Se(E_g = 550meV)$ / $Pb_{0.73}Sr_{0.27}Se(E_g = 650meV)$ barrier at 300K. Degeneracy splitting were calculated using $Schrödinger's$ equation.

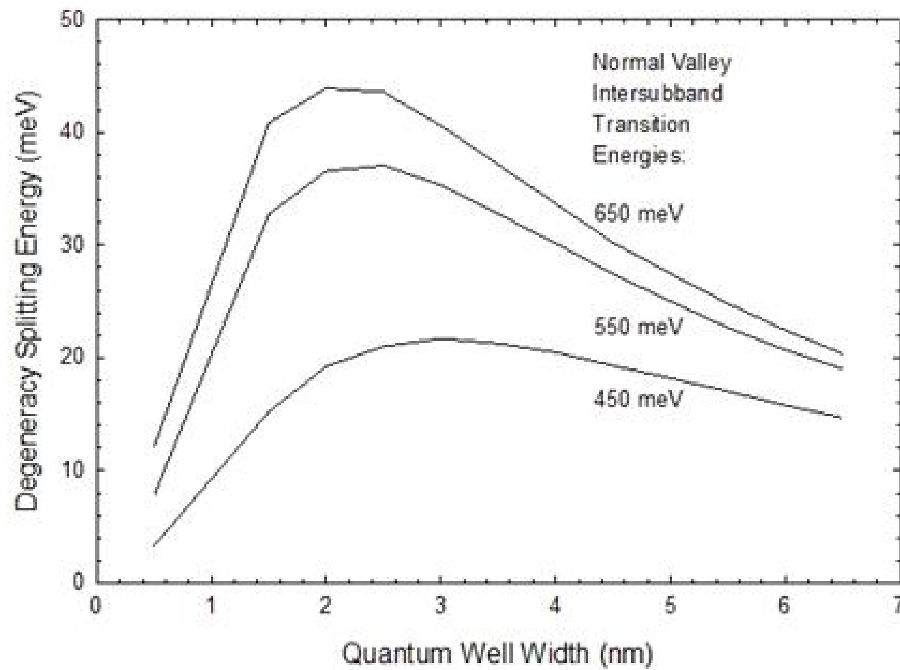

Figure 3.3: . The conduction band L-Valley degeneracy splitting energies for n=1 electrons for $PbSe(E_g = 275meV)$ well and $Pb_{0.87}Sr_{0.13}Se(E_g = 450meV)$ / $Pb_{0.775}Sr_{0.225}Se(E_g = 550meV)$ / $Pb_{0.73}Sr_{0.27}Se(E_g = 650meV)$ barrier at 300K. Degeneracy splitting energies were calculated using $Schrödinger's$ equation.

The previous section described degeneracy lifting between the L-valley conduction and valence subbands due to quantum confinement in the [110] and [111] directions. In the [111] direction, the degeneracy lifting results in a single normal valley and three-fold degenerate oblique valleys with valley extrema at different points in k-space.

Figure 3.4 illustrates the how the concentration of intrinsic carrier can be reduced by changing the concentration of the Sr alloy and with quantum confinement in the [111] direction. Note the significant reduction in number of carriers as the degeneracy split energy increases which will help significantly to reduce the dark current in a TPV device. McCann et al has focused on MBE growth and characterization of PbSrSe/PbSe multiple quantum well (MQW) structures.

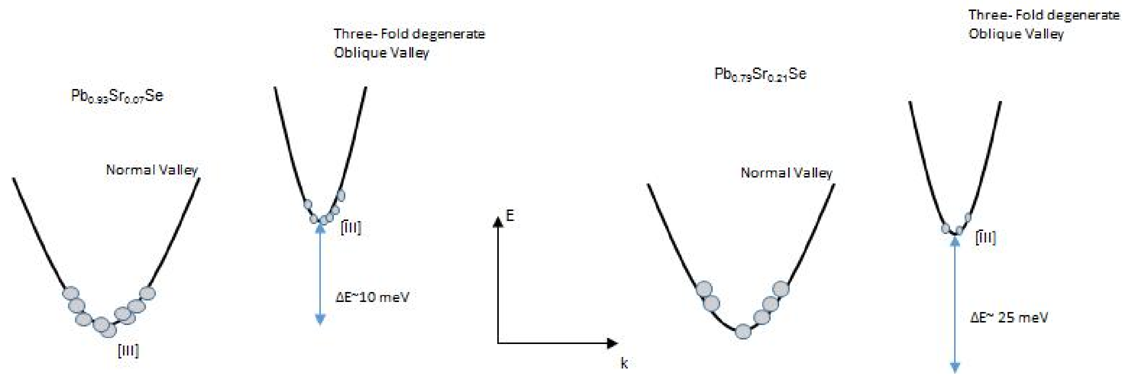

Figure 3.4:. Illustration of the degeneracy-split normal and oblique valleys in the conduction band for $Pb_{0.93}Sr_{0.07}Se$ and $Pb_{0.87}Sr_{0.13}Se$ which are indirect to one another in momentum space showing the reduction in carrier density as the degeneracy split increased.

As discussed before these structures have unique properties that make them particularly well suited as active region materials for mid-infrared lasers. Detailed procedures for MBE growth of PbSrSe/PbSe MQWs on (111)-oriented BaF_2 are described in [12]. Important results from this work include differential transmission spectroscopy (DTS) measurement of quantized energy levels in square and parabolic MQWs [2, 3]. In both cases removal of L-valley degeneracy is clearly observed, and it is shown that the quantum size effect (i.e. differences in normal and oblique valley effective masses) rather than epitaxial layer strain is responsible for L-valley degeneracy splitting for QWs thinner than 30 nm. The electron-hole pair 2-D sheet density calculated by substituting the results from Eq (3.12) and Eq (3.13), integrating over the energy difference between normal and oblique valley subband states.

$$n_i^{2D} = \int_{Subband} g^{2D}(E) f_{FD}(E) dE = \int_{E_j}^{\infty} \frac{m^*}{f\hbar^2} \frac{dE}{\left(e^{\left(\frac{E-E_F}{k_B T}\right)} + 1 \right)} \qquad (3.13)$$

Simplifying Eq (3.13) as discussed in Chapter 2 and substituting $E_f = \frac{E_g}{2}$ and summing for n^{th} bound sub bands in the quantum well we have

$$n_i^{2D} = \sum_{j=1}^{n} n_i^{2D} = \frac{m^* k_B T}{f\hbar^2} \sum_{j=1}^{n} \ln(1 + e^{(\frac{\frac{E_g}{2} - E_j}{k_B T})}) \qquad (3.14)$$

Now considering different effective masses for each sub band we can write

$$n_i^{2D} = \frac{m_{c1}^* k_B T}{f\hbar^2} \left[-\ln\left(1 + \frac{1}{x}\right) \right]_{x_1}^{x_2} + \frac{m_{c2}^* k_B T}{f\hbar^2} \left[-\ln\left(1 + \frac{1}{x}\right) \right]_{x_2}^{x_3} + \frac{m_{c3}^* k_B T}{f\hbar^2} \left[-\ln\left(1 + \frac{1}{x}\right) \right]_{x_3}^{x_4} + \ldots$$

…(3.15)

$$n_i^{2D} = \frac{m_{c1}^* k_B T}{f\hbar^2}\left[\ln\left(1+\frac{1}{x_1}\right) - \ln\left(1+\frac{1}{x_2}\right)\right] + \frac{m_{c2}^* k_B T}{f\hbar^2}\left[\ln\left(1+\frac{1}{x_2}\right) - \ln\left(1+\frac{1}{x_3}\right)\right] + \frac{m_{c3}^* k_B T}{f\hbar^2}$$

$$\left[\ln\left(1+\frac{1}{x_3}\right) - \ln\left(1+\frac{1}{x_4}\right)\right] + \ldots\ldots\ldots\ldots\ldots \quad (3.16)$$

Substituting back $x = e^{\frac{(E-E_F)}{k_B T}}$ we get,

$$n_i^{2D} = \frac{m_{c1}^* k_B T}{f\hbar^2}\left[\ln\left\{1+e^{\left(\frac{E_F-E_1}{k_B T}\right)}\right\} - \ln\left\{1+e^{\left(\frac{E_F-E_2}{k_B T}\right)}\right\}\right] + \frac{m_{c2}^* k_B T}{f\hbar^2}$$

$$\left[\ln\left\{1+e^{\left(\frac{E_F-E_2}{k_B T}\right)}\right\} - \ln\left\{1+e^{\left(\frac{E_F-E_3}{k_B T}\right)}\right\}\right] + \frac{m_{c3}^* k_B T}{f\hbar^2}\left[\ln\left\{1+e^{\left(\frac{E_F-E_3}{k_B T}\right)}\right\} - \ln\left\{1+e^{\left(\frac{E_F-E_4}{k_B T}\right)}\right\}\right] + \ldots$$

..(3.17)

Therefore by substituting $E_f = \frac{E_g}{2}$ in eq. (3.18) and summing for n bound sub bands in the quantum well we have

$$n_i^{2D} = \sum_{j=1}^{n} n_i^{2D} = \sum_{j=1}^{n} \frac{m_{cj}^* k_B T}{f\hbar^2} \sum_{j=1}^{n} \ln(1+e^{(\frac{\frac{E_g}{2}-E_j}{k_B T})}) \quad (3.18)$$

Where E_1, E_2,....are the energy states in the quantum well and m_1, m_1....are the effective masses in energy states E_1, E_2....respectively. Thus using the Eqs (3.2-3.10) we can calculate the effective masses for each valley in each sub band.

Table 3.7 Shows the intrinsic carrier concentration, dark current and open circuit voltage for bulk $Pb_{0.93}Sr_{0.07}Se(E_g = 450meV)$ and PbSe / $Pb_{0.87}Sr_{0.13}Se$ quantum well. Intrinsic carrier concentration was calculated using Equs 3.14, 2.3 and 2.5

respectively. The interband transition energy for the bulk $Pb_{0.93}Sr_{0.07}Se$ is 450 meV and the intersubband transition energy for PbSe / $Pb_{0.87}Sr_{0.13}Se$ quantum well is 450.2 meV. The energy level E_1^n was considered for this calculation.

Table 3.7: Intrinsic carrier concentration, dark current & open circuit voltage for bulk $Pb_{0.93}Sr_{0.07}Se$ and 3 nm wide PbSe/ $Pb_{0.87}Sr_{0.13}Se$ Quantum Well at 300K.

	E_g (meV)	m_e^* (kg)	n_i (cm^{-3}) at 300K	J_0 (mA) at 300K	V_{oc} (mV) at 300K
$Pb_{0.93}Sr_{0.07}Se$ (bulk)	450 meV Interband transition energy	$0.013*m_0$	7.86E+14	2.661	105.546
$PbSe$ / $Pb_{0.87}Sr_{0.13}Se$ (QW)	450.2 meV Intersubband transition energy	$0.013*m_0$	6.16E+14	1.633	118.011

Figure 3.5 is the schematic representation of interband and intersubband transition energy of 450mev in a $Pb_{0.93}Sr_{0.07}Se$ bulk and PbSe/ $Pb_{0.87}Sr_{0.13}Se$ QW material respectively.

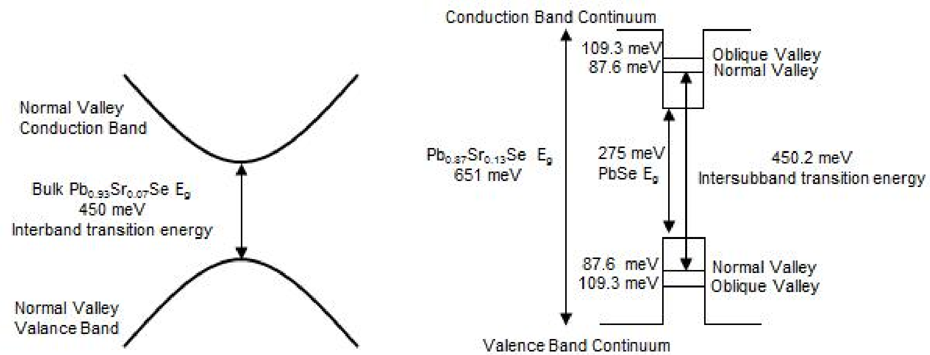

Figure 3.5: Interband transition for bulk $Pb_{0.93}Sr_{0.07}Se$ and intersubband transition for PbSe / $Pb_{0.87}Sr_{0.13}Se$ quantum well.

Table 3.8 Shows the intrinsic carrier concentration, dark current and open circuit voltage for bulk $Pb_{0.90}Sr_{0,10}Se(E_g = 550meV)$ and PbSe $/Pb_{77.5}Sr_{22.5}Se$ quantum well. Intrinsic carrier concentration was calculated using Eq 3.14, 2.3 and 2.5 respectively. The interband transition energy for the bulk $Pb_{0.90}Sr_{0,10}Se$ is 550 meV and the inter subband transition energy for PbSe / $Pb_{77.5}Sr_{22.5}Se$ quantum well is 550.6 meV. The energy level E_1^n was considered for this calculation.

Table 3.8: Intrinsic carrier concentration, dark current & open circuit voltage for bulk $Pb_{0.90}Sr_{0,10}Se$ and 2.5 nm wide PbSe/ $Pb_{77.5}Sr_{22.5}Se$ Quantum Well at 300K.

	E_g (meV)	m_e^* (kg)	n_i (cm^{-3}) at 300K	J_0 (mA) at 300K	V_{oc} (mV) at 300K
$Pb_{0.90}Sr_{0,10}Se$ (bulk)	550 meV Interband transition energy	$0.013^* m_0$	1.1384E+14	5.58E-02	203.37
$PbSe/$ $Pb_{77.5}Sr_{22.5}Se$ (QW)	550.6 meV Intersubband transition energy	$0.013^* m_0$	1.30E+13	7.23E-04	315.82

Table 3.9 Shows the intrinsic carrier concentration, dark current and open circuit voltage for bulk $Pb_{0.87}Sr_{0.13}Se(E_g = 650meV)$ and PbSe / $Pb_{73}Sr_{27}Se$ quantum well. Intrinsic carrier concentration was calculated using Eqs. 3.14, 2.3 and 2.5 respectively. The interband transition energy for the bulk $Pb_{0.87}Sr_{0.13}Se$ is 650 meV and the inter subband transition energy for PbSe / $Pb_{73}Sr_{27}Se$ quantum well is 650.2 meV. The energy level E_1^n was considered for this calculation.

Table 3.9: Intrinsic carrier concentration, dark current & open circuit voltage for bulk $Pb_{0.87}Sr_{0.13}Se$ and 2 nm wide PbSe/ $Pb_{73}Sr_{27}Se$ Quantum Well at 300K.

	E_g (meV)	m_e^* (kg)	n_i (cm^{-3}) at 300K	J_0 (mA) at 300K	V_{oc} (mV)at 300K
$Pb_{0.87}Sr_{0.13}Se$ (bulk)	650 meV Interband transition energy	$0.013{*}m_0$	1.65E+13	1.17E-03	301.34
$PbSe/$ $Pb_{73}Sr_{27}Se$ (QW)	650.2meV Intersubband transition energy	$0.013{*}m_0$	2.81E+11	3.40E-07	512.048

Figure 3.6 represent the Arrhenius plot of intrinsic carrier concentration for intrinsic carrier concentration for bulk $Pb_{0.93}Sr_{0.07}Se$ and 3 nm wide PbSe/ $Pb_{0.87}Sr_{0.13}Se$ Quantum Well as a function of inverse temperature. Figure 3.6 was plotted using the data from Table 3.8.

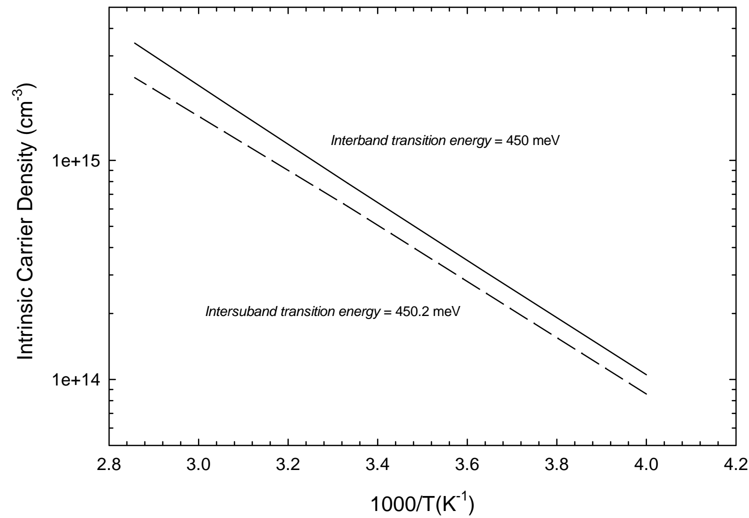

Figure 3.6: Arrhenius plot of intrinsic carrier concentration for bulk $Pb_{0.93}Sr_{0.07}Se$ and 3 nm wide PbSe/ $Pb_{0.87}Sr_{0.13}Se$ Quantum Well as a function of inverse temperature.

Figure 3.7 represent the Arrhenius plot of intrinsic carrier concentration for intrinsic carrier concentration for bulk $Pb_{0.90}Sr_{0,10}Se$ and 2.5 nm wide PbSe/$Pb_{77.5}Sr_{22.5}Se$ Quantum Well as a function of inverse temperature. Figure 3.7 was plotted using the data from Table 3.9.

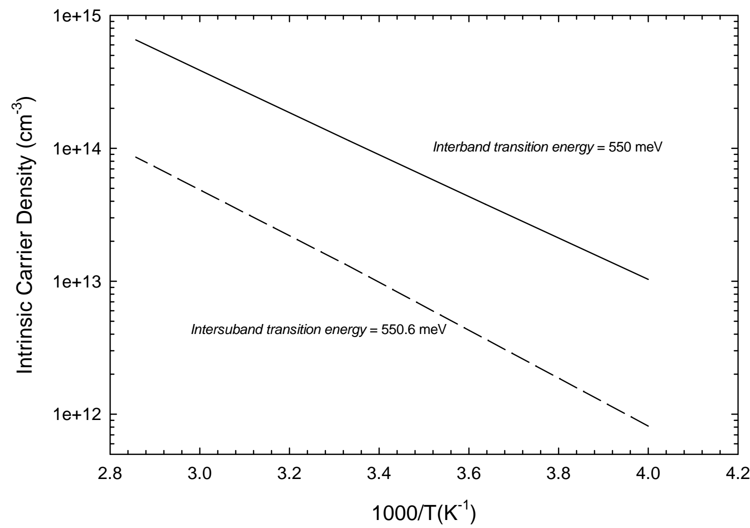

Figure 3.7: Arrhenius plot of intrinsic carrier concentration for bulk $Pb_{0.90}Sr_{0,10}Se$ and 2.5 nm wide PbSe/$Pb_{77.5}Sr_{22.5}Se$ Quantum Well as a function of inverse temperature.

Figure 3.8 represent the Arrhenius plot of intrinsic carrier concentration for intrinsic carrier concentration for bulk $Pb_{0.87}Sr_{0.13}Se$ and 2 nm wide PbSe/$Pb_{73}Sr_{27}Se$ Quantum Well as a function of inverse temperature. Figure 3.8 was plotted using the data from Table 3.10.

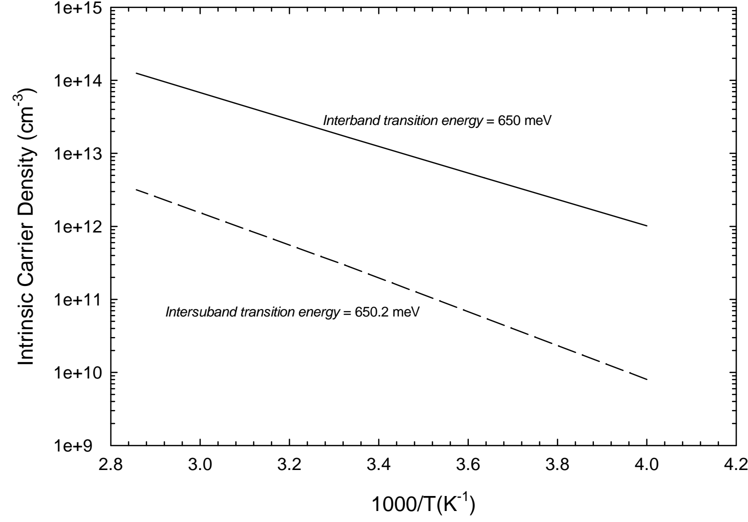

Figure 3.8: Arrhenius plot of intrinsic carrier concentration for bulk $Pb_{0.87}Sr_{0.13}Se$ and 2 nm wide PbSe/ $Pb_{73}Sr_{27}Se$ Quantum Well as a function of inverse temperature.

Reverse bias saturation current (J_0), can be calculated using equation (2.24). J_0 can be written as

$$J_0 = n_i^2 q\left(\frac{D_n}{L_n N_A} + \frac{D_p}{L_p N_D}\right) \tag{3.19}$$

Substituting the value of n_i from Eq. 2.23 we get

$$J_0 = \frac{qM_c M_v}{2}\left(\frac{\sqrt{m_h^* m_e^*} k_B T}{f\hbar^2}\right)^3 \left(\frac{D_n}{L_n N_A} + \frac{D_p}{L_p N_D}\right) e^{\frac{-E_g}{k_B T}} \tag{3.20}$$

This important figure of merit for a photovoltaic device is strongly affected by thermal generation of minority carriers as J_0 depend on the square of the intrinsic carrier concentration through the law of mass action.

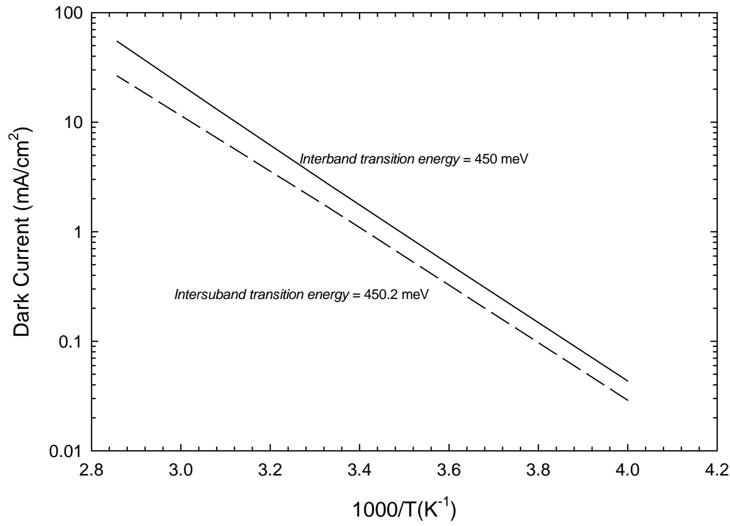

Figure 3.9: Arrhenius plot of dark current for bulk $Pb_{0.93}Sr_{0.07}Se$ and 3 nm wide PbSe/$Pb_{0.87}Sr_{0.13}Se$ Quantum Well as a function of inverse temperature.

Materials with higher degeneracy split having lower intrinsic carrier density in normal valley (Figures 3.9, 3.10 and 3.11) will have dark currents significantly lower as well as the quantum confinement effect reduces the dark current of the similar energy gap of bulk $Pb_{1-x}Sr_xSe$ material. This is illustrated in Figures 3.9, 3.10 and 3.11, Figures 3.9, 3.10 and 3.11 were plotted using the data from Tables 3.8, 3.9 and 3.10 respectively. The minority carrier lifetime considered in these plots is 100 ns which included the bulk lifetime, which is limited ultimately by Auger recombination, and the effects of surface recombination. It was assumed room temperature electron and hole mobilities of 200-300 cm^2/Vs. Figures 3.9, 3.10 and 3.11 demonstrates that there is significant reduction in dark current in a TPV device by changing the Sr. alloy resulting in lower intrinsic carrier density in normal valley electrons due to higher

degeneracy split. Quantum confinement adds additional reduction in intrinsic carrier concentration. Thus the higher alloy composition and the quantum confinement can reduce the dark current significantly in a IV –VI TPV device. It was assumed in Figures 3.9, 3.10 and 3.11 that the minority carrier lifetime is 100 ns, the improvement in dark current can be even more significant if minority carrier lifetimes are smaller.

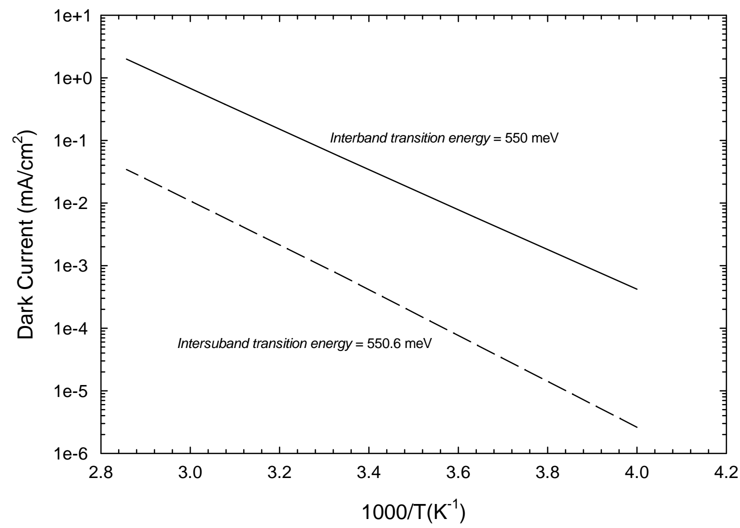

Figure 3.10: Arrhenius plot of dark current for bulk $Pb_{0.90}Sr_{0,10}Se$ and 2.5 nm wide PbSe/ $Pb_{77.5}Sr_{22.5}Se$ Quantum Well as a function of inverse temperature.

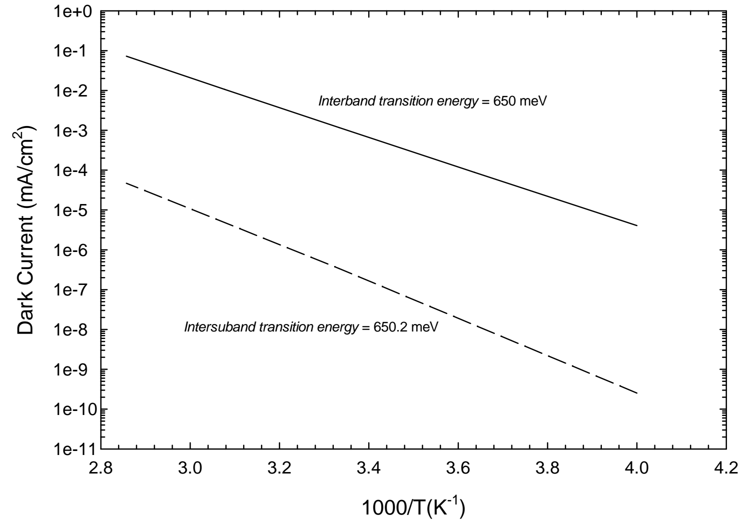

Figure 3.11: Arrhenius plot of dark current for bulk $Pb_{0.87}Sr_{0.13}Se$ and 2 nm wide PbSe/ $Pb_{73}Sr_{27}Se$ Quantum Well as a function of inverse temperature.

Figure 3.12 shows plots of dark current as a function of inverse lattice temperature for bulk QW confined by $Pb_{0.93}Sr_{0.07}Se$ (bandgap = 450 meV), $Pb_{0.90}Sr_{0.10}Se$ (bandgap = 550 meV) and $Pb_{0.87}Sr_{0.13}Se$ (bandgap = 650 meV) material for different minority carrier lifetimes, 1 ns, 10 ns, and 100 ns. The dark current, J_o, is obtained from equation (2.24-2.25).

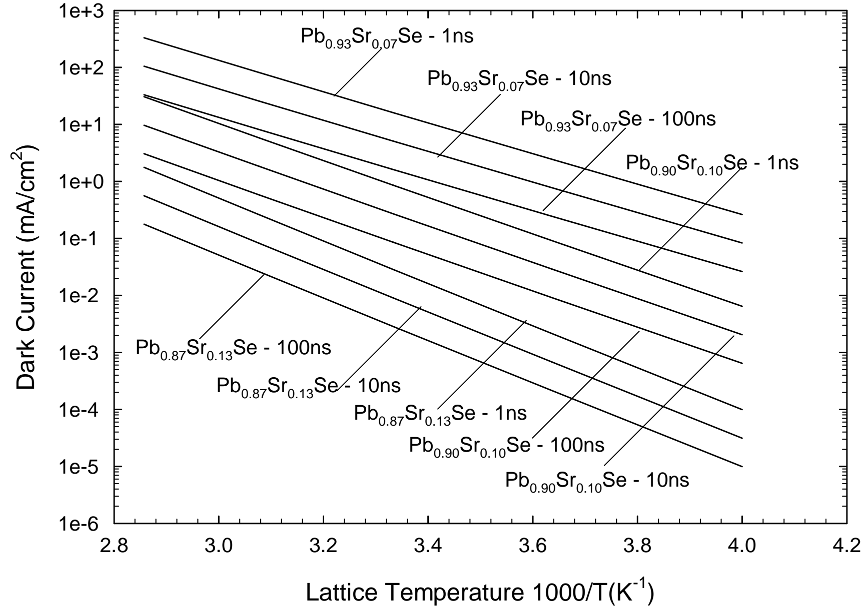

Figure 3.12: Reverse bias saturation current in a pn junction device for bulk $Pb_{0.93}Sr_{0.07}Se$, $Pb_{0.90}Sr_{0.10}Se$, and $Pb_{0.87}Sr_{0.13}Se$ material as a function of inverse lattice temperature for electron and hole minority carrier lifetime of 100ns , 10 ns and 1 ns.

The open circuit voltage for an illuminated pn junction is given by Eq (2.4)

$$qV_{oc} = nk_B T \ln\left(\frac{J_{sc}}{J_0} + 1\right) \tag{3.21}$$

Figures 3.13, 3.14 and 3.15 shows plot of open circuit voltage for a bulk $Pb_{0.93}Sr_{0.07}Se$ material and a 3 nm wide PbSe/ $Pb_{87}Sr_{13}Se$ Quantum Well, a bulk $Pb_{0.90}Sr_{0.10}Se$ material and a 2.5 nm wide PbSe/ $Pb_{77.5}Sr_{22.5}Se$ Quantum Well and a bulk $Pb_{87}Sr_{13}Se$ material and a 2 nm wide PbSe/ $Pb_{73}Sr_{27}Se$ as a function of inverse temperature respectively. Figures 3.13, 3.14 and 3.15 were plotted using the data from Tables 3.8, 3.9 and 3.10 respectively. The higher Sr. composition material has higher open circuit voltage due to the valley degeneracy removal and The QW material, due to its relatively low density of states, has much larger open circuit voltages than the same energy gap bulk material with the same minority carrier lifetime.

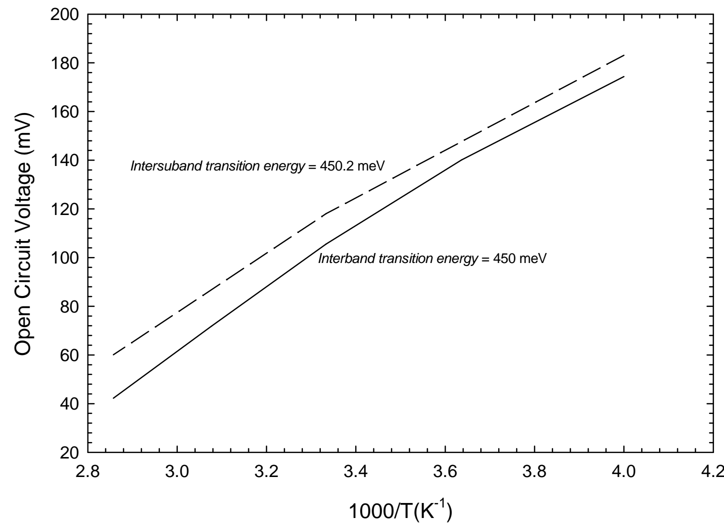

Figure 3.13: Arrhenius plot of open circuit voltage for bulk $Pb_{0.93}Sr_{0.07}Se$ and 3 nm wide PbSe/ $Pb_{87}Sr_{13}Se$ Quantum Well as a function of inverse temperature.

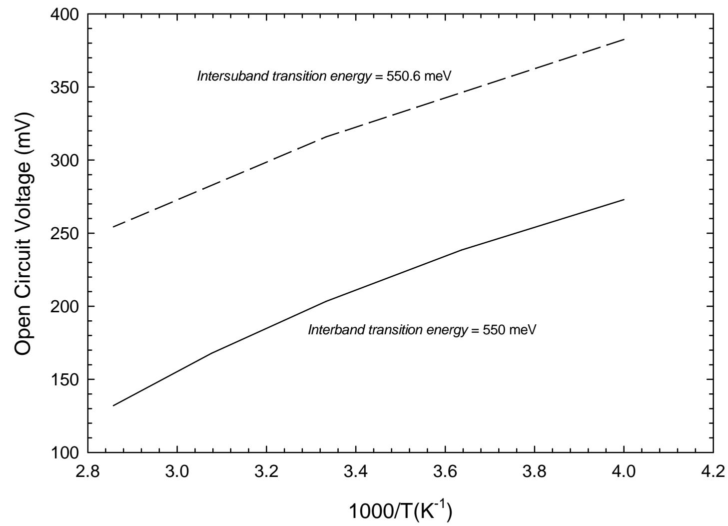

Figure 3.14: Arrhenius plot of open circuit voltage for bulk $Pb_{0.90}Sr_{0.10}Se$ and 2.5 nm wide PbSe / $Pb_{77.5}Sr_{22.5}Se$ Quantum Well as a function of inverse temperature.

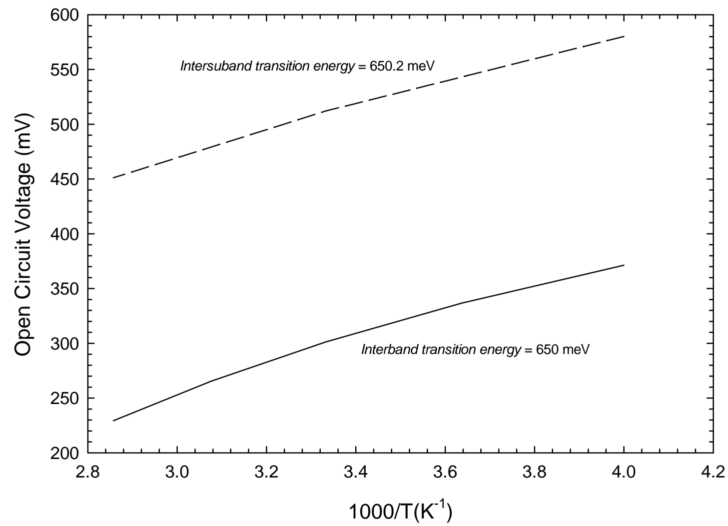

Figure 3.15: Arrhenius plot of open circuit voltage for bulk $Pb_{87}Sr_{13}Se$ and 2 nm wide PbSe / $Pb_{73}Sr_{27}Se$ Quantum Well as a function of inverse temperature.

Figure 3.16 shows plots of open circuit voltage as a function of inverse lattice temperature for $Pb_{0.93}Sr_{0.07}Se$ (bandgap = 450 meV), $Pb_{0.90}Sr_{0.10}Se$ (bandgap = 550 meV) and $Pb_{0.87}Sr_{0.13}Se$ (bandgap = 650 meV) materials for different minority carrier lifetimes, 1 ns, 10 ns, and 100 ns.

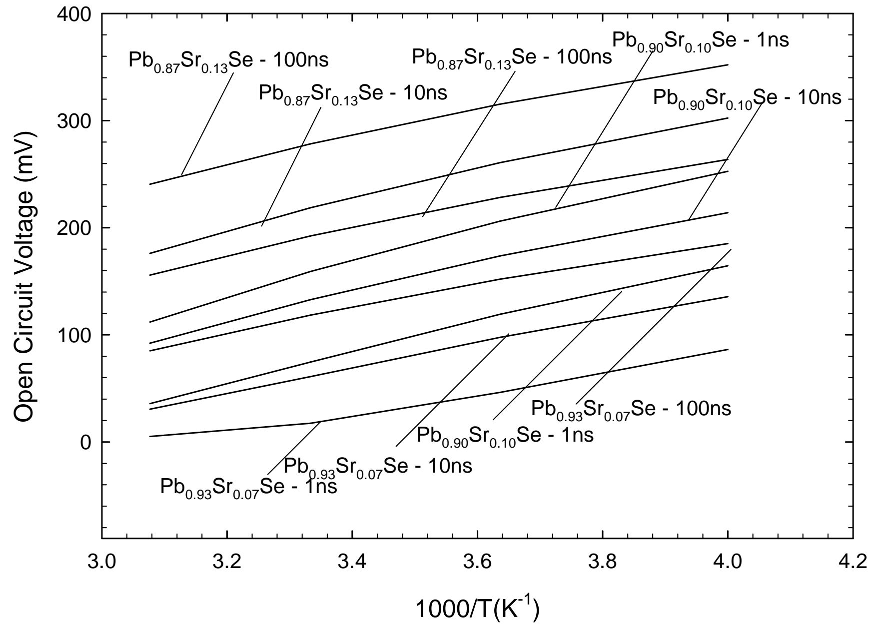

Figure 3.16: Open circuit voltage in a pn junction device for bulk $Pb_{0.93}Sr_{0.07}Se$, $Pb_{0.90}Sr_{0.10}Se$, and $Pb_{0.87}Sr_{0.13}Se$ as a function of inverse lattice temperature for electron and hole minority carrier lifetime of 100ns, 10 ns and 1 ns.

3.6 Summary and Conclusion

In this chapter the relationship between intrinsic carrier density, dark current and open circuit voltage for bulk and Quantum Well IV-VI material were demonstrated. The variations of effective masses in different bands and subbands were also calculated. A novel method to calculate intrinsic carrier density, dark current and open circuit voltage was developed based on the similar direct interband transition energy of bulk $Pb_{1-x}Sr_xSe$ and inter subband transition energy of PbSe well and $Pb_{1-x}Sr_xSe$ barrier QW because of the degeneracy split that occur between the normal and three fold degenerate oblique valley states. Thus in this chapter it was shown how the reduction of density of states for IV-VI materials can be achieved by applying the quantum confinement technique which will help significantly in the reduction of reverse bias saturation (dark) current and thus increase in open circuit voltage and external quantum efficiency of a narrow gap IV-VI semiconductor material TPV cell.

References:

[1] R. F. Pierret, Advanced Semiconductor Fundamentals, v. IV, 2nd Ed. (Prentice Hall, New Jersey, 2003).

[2] W. Z. Shen, H. F. Yang, L. F. Jiang, K. Wang, and G. Yu, H. Z. Wu and P. J. McCann," Band gaps, effective masses and refractive indices of PbSrSe thin films: Key properties for mid-infrared optoelectronic device applications" J. Appl. Phys., vol. 91, no. 1, pp. 3319–3327, Jan. 2002.

[3] H. Z. Wu, N. Dai, M.B. Johnson, P. J. McCann and Z. S. Shi," Unambiguous observation of sub band transitions from longitudinal valley and oblique valleys in IV–VI multiple quantum wells" Applied Physics Letters., Volume 78, Number 15, 9 April 2001.

[4] Krier, Anthony "Mid-infrared Semiconductor Optoelectronics" Springer 2006.

[5] Choi, Hong K. "Long -Wavelength Infrared Semiconductor Lasers" Wiley-Interscience, A John Wiley & Sons, Inc. , Publication 2004.

[6] Varshni YP (1967) Temperature dependence of the energy gap in semiconductors. Physica 34:149–154.

[7] Zachary M. Gibbs, Massoud Kaviany, Hyoungchul Kim and G. Jeffrey Snyder, Heng Wang, Robert L. White,Temperature dependent band gap in PbX (X =S, Se, Te); Applied Physics Letters 103, 262109 (2013).

[8] Zachary M. Gibbs; Band Engineering in Thermoelectric Materials Using Optical, Electronic, and Ab-Initio Computed Properties. Dissertation thesis California Institute of Technology 2015.

[9] H. Preier, “Recent Advances in Lead-Chalcogenide Diode Lasers”, *Appl. Phys.* 20, 189 (1979).

[10] W. Z. Shen, K.Wang, and L. F. Jiang; X. G. Wang and S. C. Shen; H. Z. Wu and P. J. McCann " Study of band structure in PbSe/PbSrSe quantum wells for midinfrared laser applications" Applied Physics Letters; Volume 79, Number 16; 15 October 2001.

[11] P. C. Findlay, C. R. Pidgeon, R. Kotitschke, A. Hollingworth, B. N. Murdin C. J. G. M. Langerak, A. F. G. van der Meer, C. M. Ciesla, J. Oswald, A. Homer, G. Springholz and G. Bauer " Auger recombination dynamics of lead salts under picosecond free-electron-laser excitation" phys. Rev. B 58, 12908 (1998).

[12] J. R. Meyer, C. L. Felix, W. W. Bewley, I. Vurgaftman, E. H. Aifer, L. J. Olafsen, J. R. Lindle, C. A. Hoffman, M.-J. Yang, B. R. Bennett, B. V. Shanabrook,

H. Lee, C.-H. Lin, S. S. Pei and R. H. Miles " Auger coefficients in type-II InAs/Ga1−xInx Sb quantum wells" Appl. Phys. Lett. 73, 2857 (1998).

[13] D. L. Partin, "Lead salt quantum effect structures," IEEE J. Quantum Electron., 24, 1716 (1988).

[14] M. F. Khodr, P. J. McCann, and B. A. Mason, "Optimizing and Engineering EuSe/PbSe0.78Te0.22/EuSe Multiple Quantum Well Lasers", IEEE Journal of Quantum Electronics 94, 1604 (1998).

[15] A .Ishida, Y. Sase and H. Fujiyasu " Optical properties of PbTe/$Pb_{1-x}Eu_xTe$ superlattices prepared by hot wall epitaxy" Appl. Surf. Sci 33/34 868 (1988).

[16] Akihiro Ishida, Shuji Matsuura, Makoto Mizuno and Hiroshi Fujiyasu "Observation of quantum size effects in optical transmission spectra of PbTe/$Pb_{1-x}Eu_xTe$ superlattices", Appl. Phys. Lett. 51, 478 (1987).

[17] Shu Yuan, H. Krenn, G. Springholz, G. Bauer and M. Kriechbaum " Large refractive index enhancement in PbTe/$Pb_{1-x}Eu_xTe$ multi quantum well structures" Appl. Phys. Lett. 62, 885 (1993).

[18] X M Fang, K Namjou, I Chao, P J McCann, N Dai, G Tor "Molecular beam epitaxy of PbSrSe and PbSe/PbSrSe multiple quantum well structures for use in midinfrared light emitting devices" J. Vac. Sci. Technol. B 18, 1720 (2000).

[19] I. I. Zasavitskii, E. A. de Andrada e Silva, E. Abramof, and P. J. McCann, "Optical Deformation Potentials for PbSe and PbTe", *Phys. Rev. B* 70, 115302 (2004).

[20] L. A. Elizondo, Y. Li, A. Sow, R. Kamana, H. Z. Wu, S. Mukherjee, F. Zhao, Z. Shi, and P. J. McCann, “Optically pumped mid-infrared light emitter on silicon”, *Journal of Applied Physics* 101, 104504 (2007).

[21] W. Xu, F. M. Peeters, and J. T. Devreese, “Electrophonon resonances in a quasi- two-dimensional electron system”, *Phys. Rev. B* 48, 1562 (1993).

[22] V. Bondarenko, “Electron-optical phonon interaction and in-plane mobility in lead chalcogenide quantum-well structures”, *Phys. Rev. B* 59, 15312 (1999).

[23] S. C. Lee, J. W. Kang, H. S. Ahn, M. Yang, N. L. Kang, and S. W. Kim, “Opticallydetected electron phonon resonance effects in quantum wells”, *Physica* E 28, 402 (2005).

[24] V. L. Gurevich, V. B. Pevzner, and G. Iafrate, “Electrophonon Resonances in Mesoscopic Structures”, *Phys. Rev. Lett.* 75, 1352 (1995).

[25] S. Yu, V. B. Pevzner, K. W. Kim, and M. A. Stroscio, "Electrophonon resonance in cylindrical quantum wires", *Phys. Rev. B* 58, 3580 (1998).

[26] M. Beck, D. Hofstetter, T. Aellen, J. Faist, U. Oesterle, M. Ilegems, E. Gini, and H. Melchior, "Continuous-wave operation of a mid-infrared semiconductor laser at room temperature", *Science* 295 , 301 (2002).

[27] R. Q. Yang, C. J. Hill, and B. H. Yang, "High-temperature and low-threshold midinfrared interband cascade lasers", *Appl. Phys. Lett.* 87, 151109 (2005).

[28] C. S. Kim, C. L. Canedy, E. H. Aifer, M. Kim, W. W. Bewley, J. G. Tischler, D. C.Larrabee, J. A. Nolde, J. H. Warner, I. Vurgaftman, E. M. Jackson, and J. R. Meyer, "Molecular beam epitaxy growth of antimonide type-II "W" high-power interband cascade lasers and long-wavelength infrared photodiodes",*J. Vac. Sci. Technol. B* 25,91 (2007).

[29] Gangyi Xu, Aizhen Li, Yaoyao Li, Lin Wei, Yonggang Zhang, Chun Lin, and Hua Li, "Low threshold current density distributed feedback quantum cascade lasers with deep top gratings", *Appl. Phys. Lett*. 89, 161102 (2006).

[30] G. Pellegrini, G. Mattei, and P. Mazzoldi, "Finite depth square well model: Applicability and limitations", *J. Appl. Phys.* 97, 073706 (2005).

[31] K. K. Nanda, F. E. Kruis, H. Fissan, "Effective mass approximation for two extreme semiconductors: Band gap of PbS and CuBr nanoparticles", *J. Appl. Phys.* 95, 5035(2004).
[32] K. K. Nanda, F. E. Kruis, H. Fissan, "Energy Levels in Embedded Semiconductor Nanoparticles and Nanowires", *Nano Lett.* 1, 605 (2001).

Chapter 4

Growth, Fabrication, and Characterization of IV-VI Semiconductor TPV Devices

For a successful technology reality must take precedence
over public relations, for nature cannot be fooled.
Richard Feynman

4.1 MBE Growth of IV-VI Semiconductor TPV Device Structure

There are at least two techniques by which the semiconductor heterostructures can be grown, molecular beam epitaxy (MBE) [1] and metal-organic chemical vapor deposition (MOCVD) [2]. Both can achieve a layer thickness control close to about one atomic layer. Devices were grown using MBE for this dissertation research. MBE is a very high vacuum technique in which beams of the constituent atoms or molecules e.g., PbSe, Se, and Sr, (for IV-VI materials) emerge from effusion cells and attach to the surface of a heated substrate. The material to be grown is controlled by opening and closing shutters in front of the effusion cells. Unlike III-V semiconductors, IV-VI semiconductors can be grown on lattice and thermally mismatched silicon substrates without developing a high density of crystalline defects [3]. The work described in this chapter takes advantage of this attractive materials growth capability.

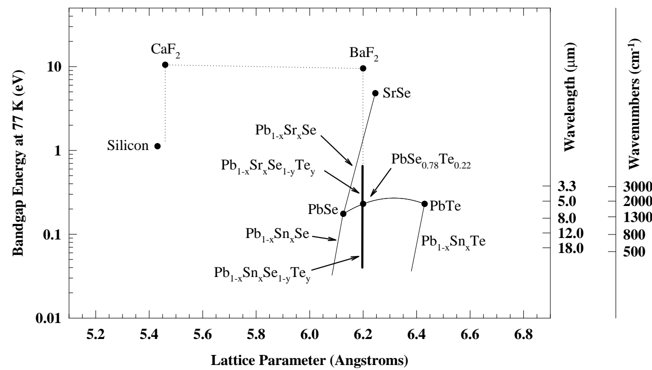

Figure 4.1: Bandgap energy and lattice constants of various binary IV-VI compounds.

Bandgap energy at 77 K and lattice constants of various IV-VI compounds and alloys are shown in Figure.4.1. The IV-VI semiconductor structure studied here consisted of a bulk pn junction $Pb_{0.93}Sr_{0.07}Se$ (Sr content = 7%) active layer $2 \sim m$ thick n-type PbSe ($n = 4 \times 10^{18} cm^{-3}$) along with $2 \sim m$ thick p-type PbSe ($p = 4 \times 10^{17} cm^{-3}$) all epitaxially grown on a 3 inch diameter Si (111) substrate in an Intevac GEN II modular MBE system (Figure 4.2).

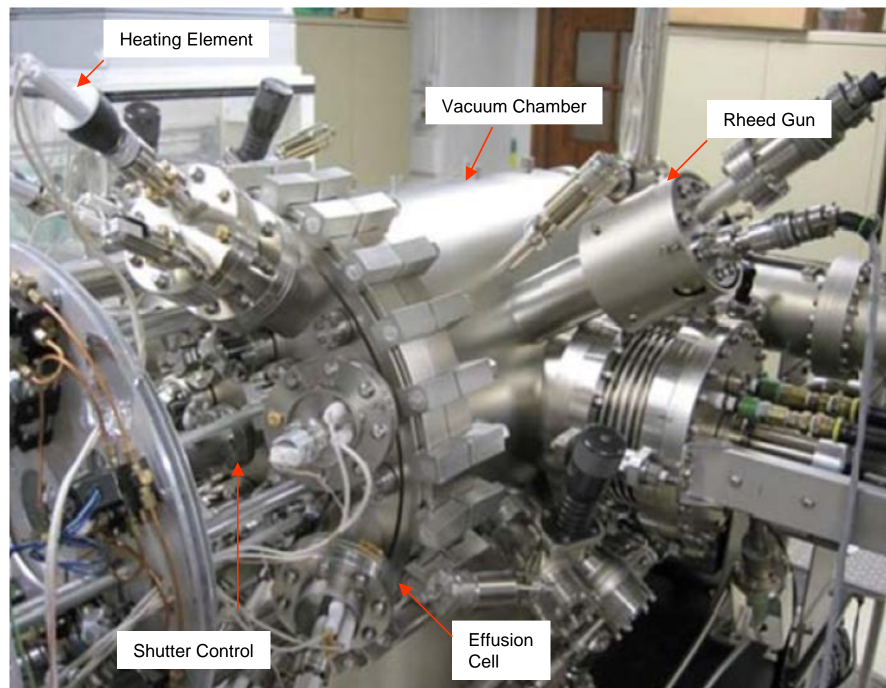

Figure 4.2: MBE system used to fabricate IV-VI TPV devices at University of Oklahoma.

The Si (111) substrate was prepared for epitaxial growth by utilizing the standard Shiraki cleaning method [4]. Native silicon dioxide desorption, as confirmed by a clear reflection high energy electron diffraction (RHEED) pattern indicating a (7x7)

reconstruction for the Si(111) surface, took place in the growth chamber at a substrate temperature of 800°C, immediately after which a 2.6 nm-thick layer of CaF_2 was grown. A streaky (1x1) RHEED pattern was observed for the as-grown CaF_2 indicating a smooth, crystalline, and un-reconstructed layer surface. A $3\sim m$ thick BaF_2 buffer layer followed by a bulk pn junction $Pb_{0.93}Sr_{0.07}Se$ (Sr content 7%) active layer was grown. The active layer consists of a $2\sim m$ thick n-type $Pb_{0.93}Sr_{0.07}Se$ ($n = 4\times10^{18}\,cm^{-3}$) doped with bismuth from a Bi_2Se_3 effusion cell along with a $2\sim m$ thick p-type $Pb_{0.93}Sr_{0.07}Se$ ($p = 4\times10^{17}\,cm^{-3}$), which was lightly p-type due to Pb vacancies with the excess selenium overpressure during growth. The beam equivalent pressures (BEPs) for PbSe, Se, Sr, and Bi_2Se_3 were $6.10\text{x}10^{-7}$, $1.46\text{x}10^{-7}$, $1.83\text{x}10^{-8}$, and $3.3\text{x}10^{-8}$ Torr, respectively. The electron and hole densities in the n-type and p-type layers are determined from Hall effect measurements of single calibration layers grown separately. Typical room temperature electron and hole mobilities in these layers are in the range of 200 to 300 cm^2/Vs. The complete structure grown in this study is depicted in Fig 4.3.

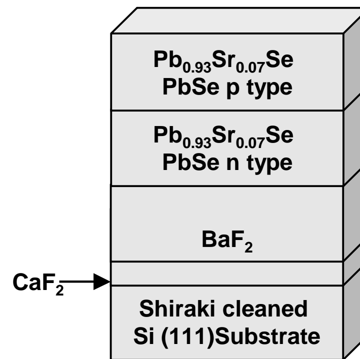

Figure 4.3: $Pb_{0.93}Sr_{0.07}Se$ TPV diode structure epitaxially grown using MBE. This growth was identified as number M292.

4.2 Fabrication of IV-VI Semiconductor TPV Devices

After the structure is grown it goes through device processing steps which involve flip chip [5] eutectic bonding. Ohmic contact metallization is first performed with thermal evaporation of Cr and Au to the as-grown p-type $Pb_{0.93}Sr_{0.07}Se$ layer. Electron beam evaporation was then used to deposit a Ti/Ni diffusion barrier layer and Sn followed by a thin layer of Au to inhibit Sn oxidation. Eutectic bonding of the 1x1 cm^2 MBE-grown chip to a 1x1 cm^2 copper chip metallized with Ni, In, and Au was performed in a custom built vacuum bonding chamber at about 125°C where the In and Sn form a eutectic liquid bond [5]. After cooling and removal from the bonder the bonded assembly is immersed in distilled water where the water-soluble fluoride buffer layers dissolve and the silicon growth substrate falls off. Photolithographic pattering and etching with a 1% Br:HBr solution were then performed to form isolated mesas. An insulating layer of parylene about 1 micron thick was then deposited after which photolithographic pattering and O_2 plasma etching is used to form a contact via in the center of each mesa. The final processing step is photolithographic patterning and thermal evaporation of top ohmic contacts using lift-off metallization. The final device structure fabricated for this study is depicted in Fig 4.4.

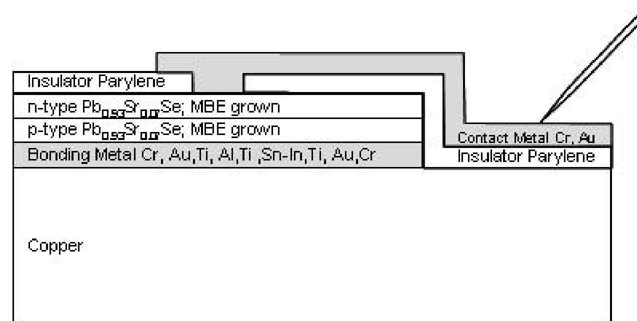

Figure 4.4: Fabricated TPV device.

4.3 IV-VI Semiconductor Device Characterization – LED and Detector Results

Figure 4.5 shows the light emitting diode (LED) emission spectrum and the detector spectral response spectrum from two different devices with different mesa sizes (200x 200 μm^2 and 400x 400 μm^2) fabricated from MBE growth number M292. Results show that the bandgap of the $Pb_{0.93}Sr_{0.03}Se$ material is 450 meV. These device results document the first known successful fabrication of IV-VI semiconductor optoelectronic devices from materials grown on a silicon substrate and transferred to copper. The LED emission results are also the first known demonstration of continuous wave (cw) emission from a IV-VI semiconductor device at room temperature. These results demonstrate the benefits of enhanced thermal management by bonding the epitaxial device structure to a high thermal conductivity copper substrate.

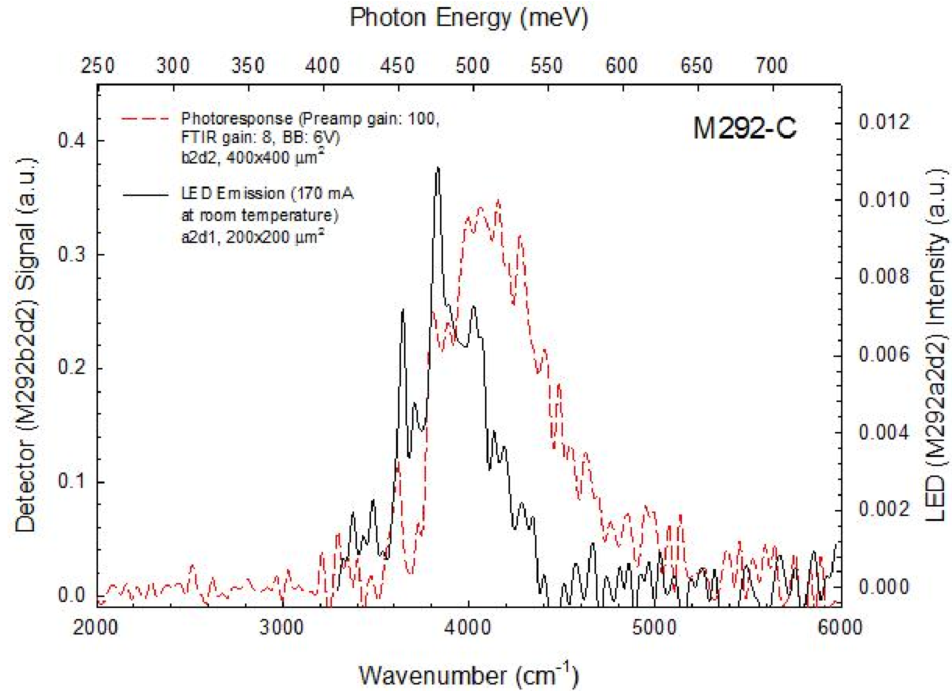

Figure 4.5: LED emission and detector photoresponse of M292 showing the bandgap energy of the material is 450 meV.

4.4 Current versus Voltage Characterization

Current versus voltage characterization for M292 was conducted using a Keithley 2400 source meter and a Keithley 2182A nano voltmeter. The sample (M292) was mounted to a copper base plate on a thermoelectric (TE) cooler, the temperature of which was stabilized using a modular laser diode controller power supply, LDC 3900, ILX Lightwave, Inc.

This section describes the current versus voltage characteristics of two different devices fabricated from MBE growth number M292, M292 a2e1 and M292 b1a3. Figures 4.6 and 4.8 show the current versus voltage characteristics on linear and semi-logarithmic plots at heat sink temperatures of 10, 20, 30, 40, and 50 °C for device

number M292 a2e1, a bulk $Pb_{0.93}Sr_{0.07}Se$ pn junction having a 200x 200 μm^2 mesa area and a 0.0003 cm^2 open area – the area covered by the top metallization is 0.0001 cm^2. Figures 4.7 and 4.9 show the current versus voltage characteristics on linear and semi-logarithmic plots at heat sink temperatures of 10, 20, 30, 40, and 50 °C for device number M292 b1a3, a bulk $Pb_{0.93}Sr_{0.07}Se$ pn junction having a 400x 400 μm^2 mesa area and a 0.0012 cm^2 open area – the area covered by the top metallization is 0.0004 cm^2. Figure 4.10 shows an expanded view of the reverse bias saturation current voltage plot for M292 b1a3 near the zero volt region for temperatures between $10^0 C$ and $50^0 C$. These data show the effects of thermal generation on reverse bias saturation current. At -26 mV it increases from 7.5 mA/cm^2 to 26.9 mA/cm^2 as the temperature increases from 10°C to 50°C indicating an increase in thermal generation of charge carriers across the 450 meV band gap of the pn junction material.

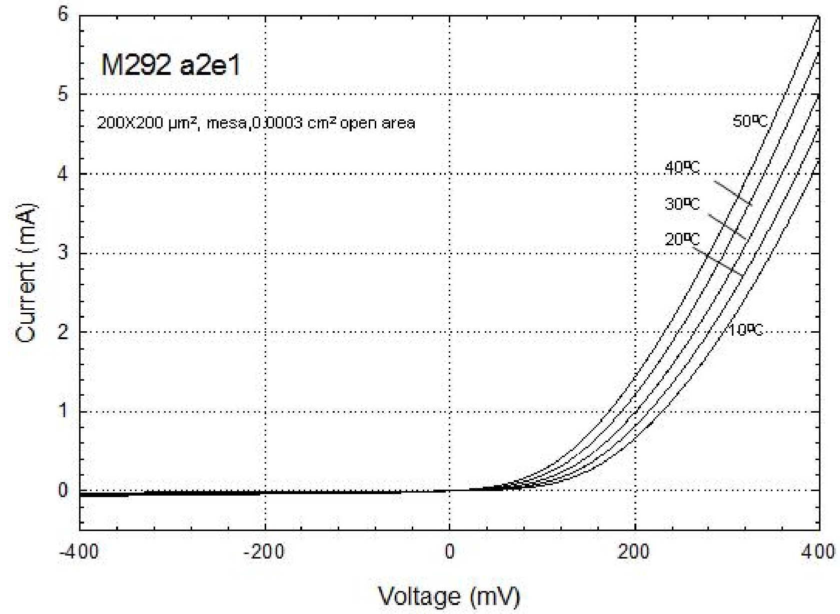

Figure 4.6: Linear plot of current versus voltage characteristics of M292 a2e1, for temperatures between $10^0 C$ and $50^0 C$.

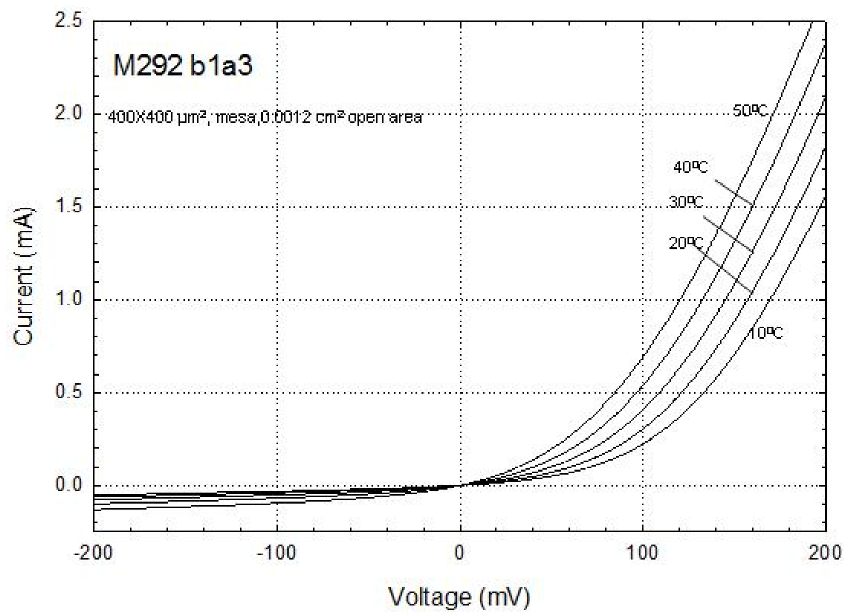

Figure 4.7: Linear plot of current versus voltage characteristics of M292 b1a3, for temperatures between $10^0 C$ and $50^0 C$.

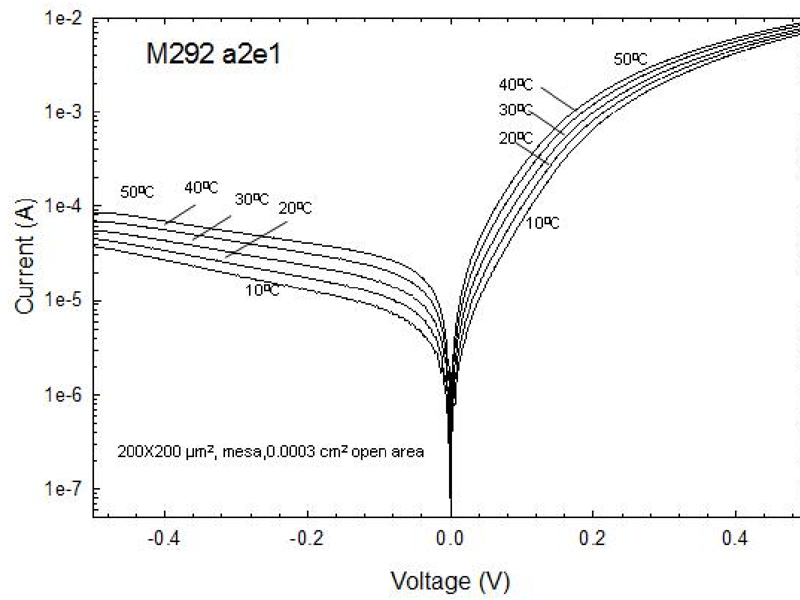

Figure 4.8: Semi-logarithmic plot of current versus voltage characteristics of M292 a2e1 for temperatures between $10^0 C$ and $50^0 C$.

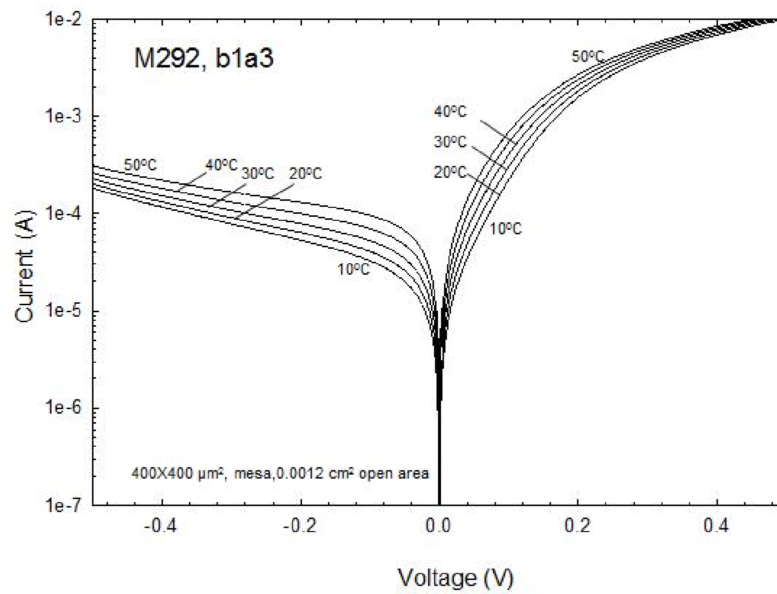

Figure 4.9: Semi-logarithmic plot of current versus voltage characteristics of M292 b1a3 for temperatures between $10^0 C$ and $50^0 C$.

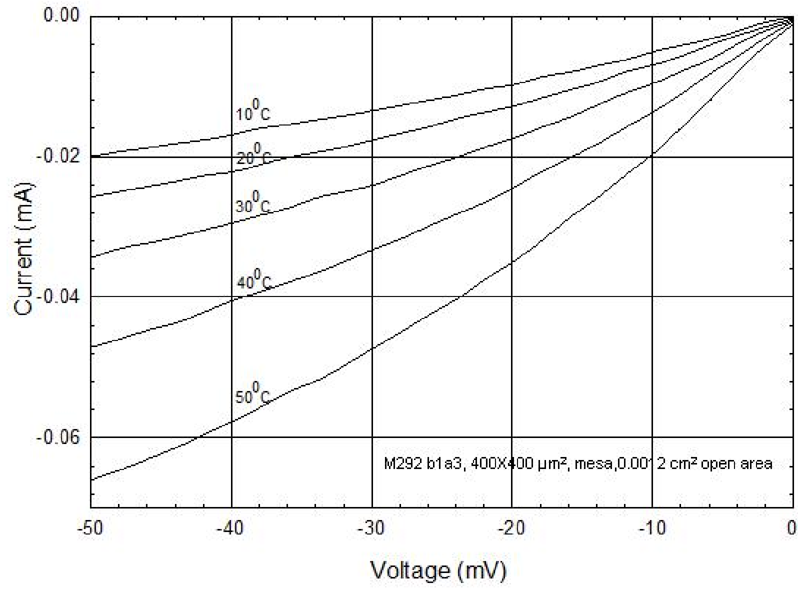

Figure 4.10: Expanded view of the reverse bias region for M292 b1a3 at temperatures between $10^0 C$ and $50^0 C$.

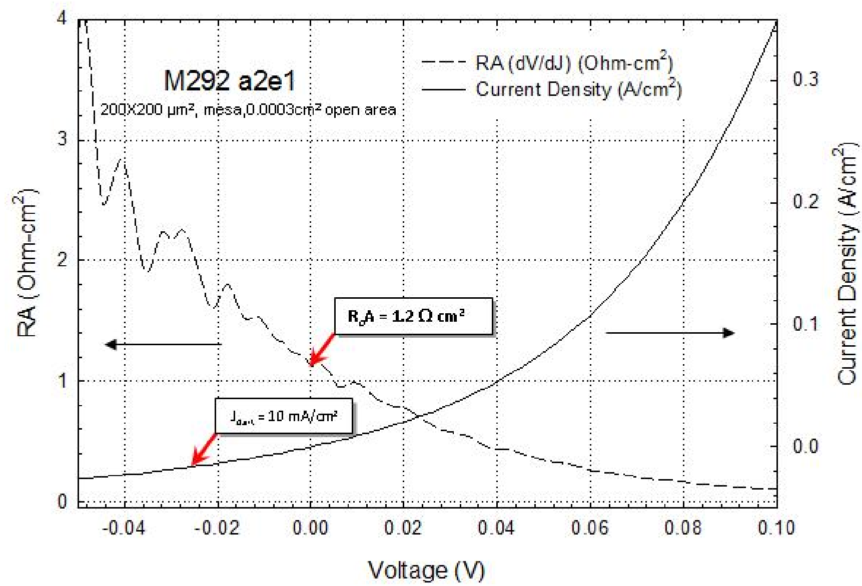

Figure 4.11: The resistance area product for M292 a2e1 at 300 K.

Figure 4.11 plots the resistance area product for M292 a2e1 at room temperature showing that the R_oA product (at V=0) is 1.35 Ωcm^2. A similar value of 1.35 Ωcm^2 is obtained for the larger mesa device, M292 b1a3, as shown in Figure 4.12. These values are in the same range as commercial mid-infrared detectors available from Vigo Systems S.A., which have specification sheet values of > 1 Ωcm^2 for detectors with cutoff wavelengths that are less than 3 microns (bandgaps greater than 414 meV).

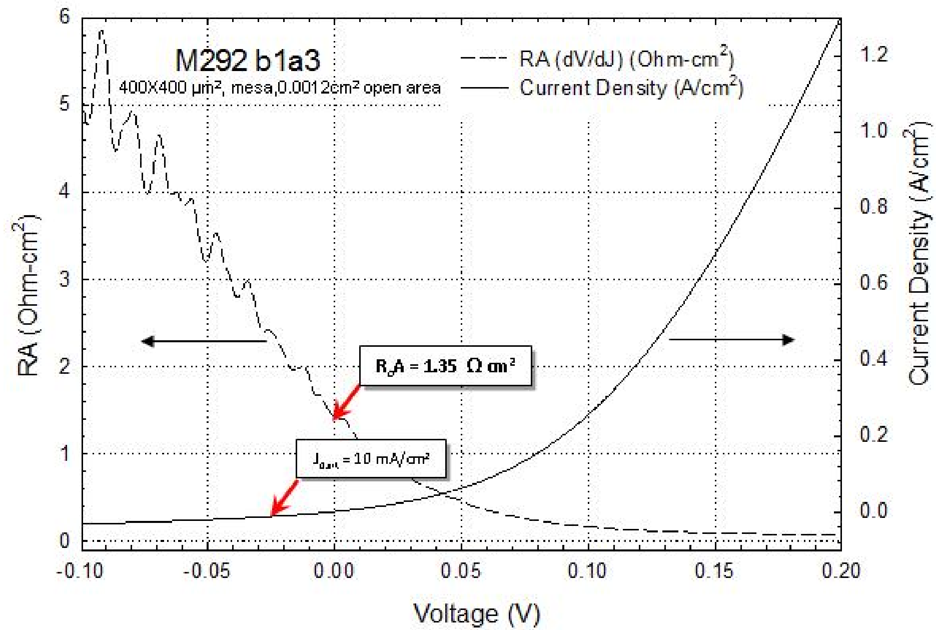

Figure 4.12: The resistance area product for M292 b1a3 at 300 K.

4.5 Device Characterization with Broadband Illumination

The current voltage characterization of devices from MBE growth number M292 under broadband illumination conditions was conducted using the same electrical and temperature control instrumentation described above. Broadband illumination was

provided by a resistance heated Si_3N_4 filament mounted inside a parabolic reflector (Hawkeye, Inc., part number IR-Si 272-P-1). Radiation was collimated by the parabolic reflector and focused using a concave mirror, a 4” diameter CaF_2 lens, and a 1” diameter ZnSe lens as shown in Figure 4.13

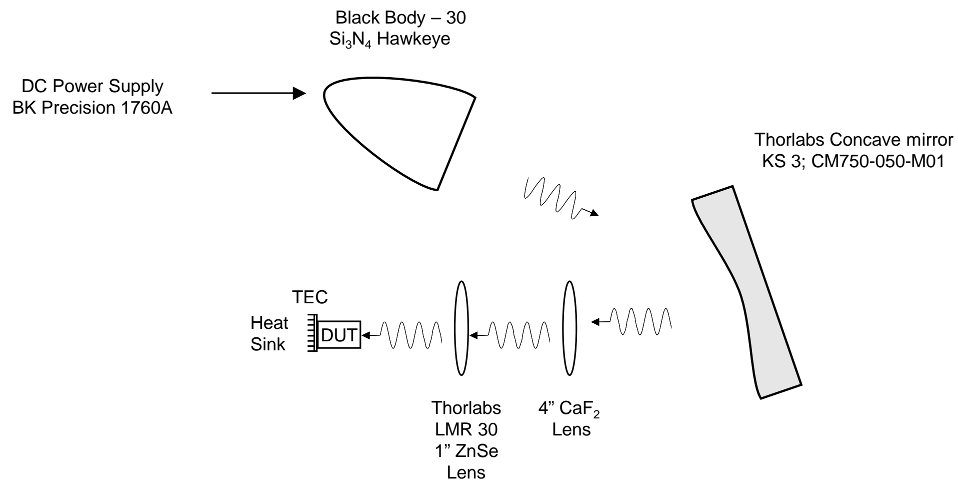

Figure 4.13: Experimental setup for measurement of current versus voltage characteristics with broadband thermal illumination.

With 6 volts of applied bias the Si_3N_4 filament is rated to dissipate 30 watts of total power and achieve a temperature of 1160°C. Measurements of the optical power density at the sample location using two different calibrated power meters (Newport, model # BK Precision 1760A and ThorLabs model # PM100A) showed a spotty intensity profile with the most intense spot having a broadband optical power density of 5.6 Watts/cm^2.

Figure 4.14 shows a semi-logarithmic plot of the current versus voltage characteristics of M292 a2e1 at heat sink temperatures between $10^0 C$ and $50^0 C$.

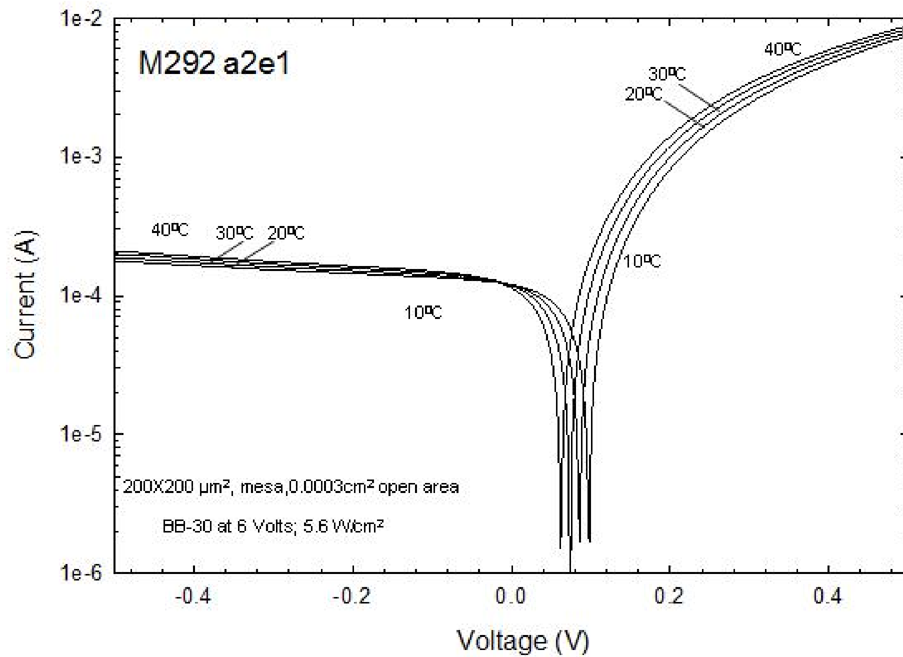

Figure 4.14: Semi-logarithmic plot of current versus voltage characteristics of M292 a2e1, for temperatures between $10^0 C$ and $50^0 C$ for broadband thermal radiation with the device located at a hot spot with an optical power density of 5.6 Watts/cm^2.

Figure 4.15 is a semi-logarithmic plot of the current versus voltage characteristics of M292 b1a3 at heat sink temperatures between $10^0 C$ and $50^0 C$.

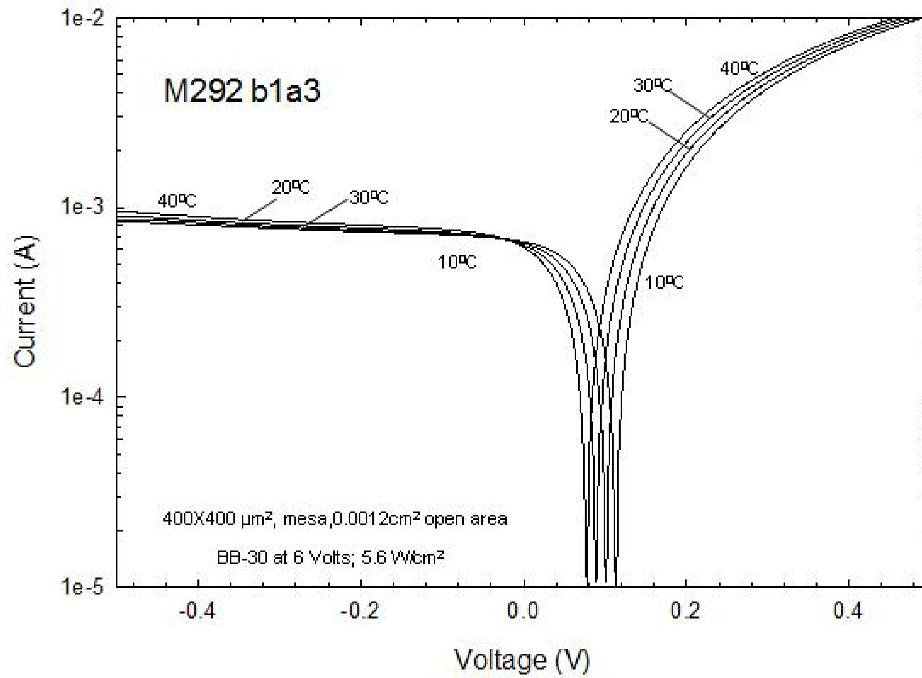

Figure 4.15: Semi-logarithmic current versus voltage characteristics of M292 b1a3, for temperatures between 10^0C and 50^0C.

Figure 4.16 shows the current density versus voltage characteristics of the two different sized pn junction devices, M292 a2e1 mesa size $200\times200{\sim}m^2$ and M292 b1a3 mesa size $400\times400{\sim}m^2$, at 10^0C. The plots show the open circuit voltage for M292 a2e1 is 98 mV, while the open circuit voltage for M292 b1a3 with its 4 times larger mesa size is 113mV. The short circuit current densities are 0.298 mA/cm^2 and 0.40 mA/cm^2 for the smaller and larger mesa devices, respectively.

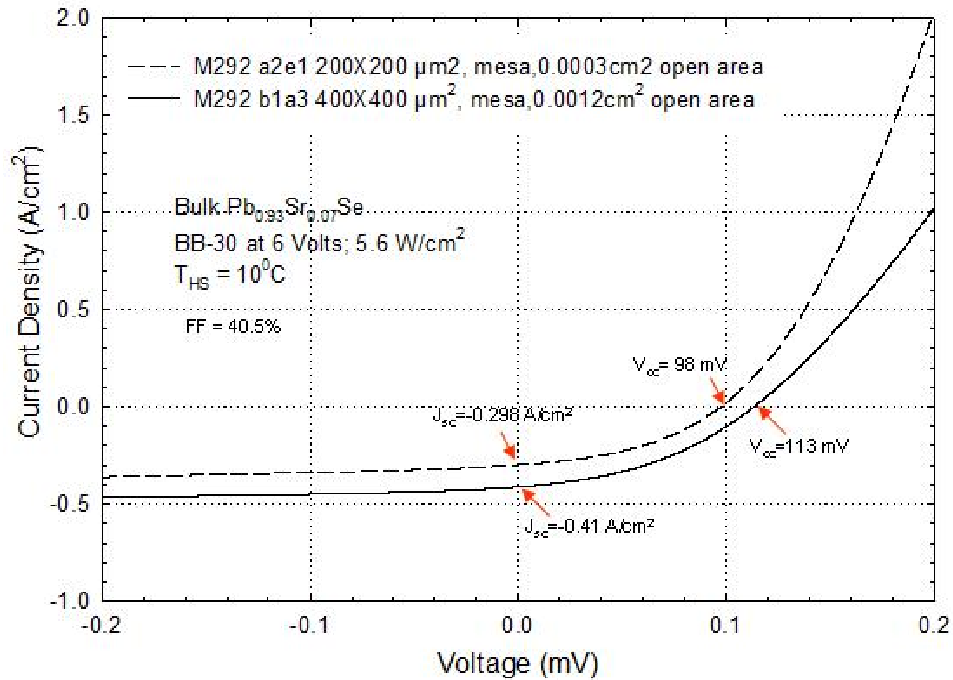

Figure 4.16: Current density versus voltage plot for M292 a2e1 and b1a3 at 10^{0}C.

Figure 4.17 shows the current density versus voltage characteristics of the two different sized pn junction devices, M292 a2e1 mesa size $200\times 200{\sim}m^2$ and M292 b1a3 mesa size $400\times 400{\sim}m^2$, at $40^0 C$. The plots show the open circuit voltage for M292 a2e1 is 62 mV while the open circuit voltage for M292 b1a3 with its 4 times lager mesa size $400\times 400{\sim}m^2$ is 78 mV. The short circuit current densities are 0.284 mA/cm^2 and 0.385 mA/cm^2 for the smaller and larger mesa devices, respectively.

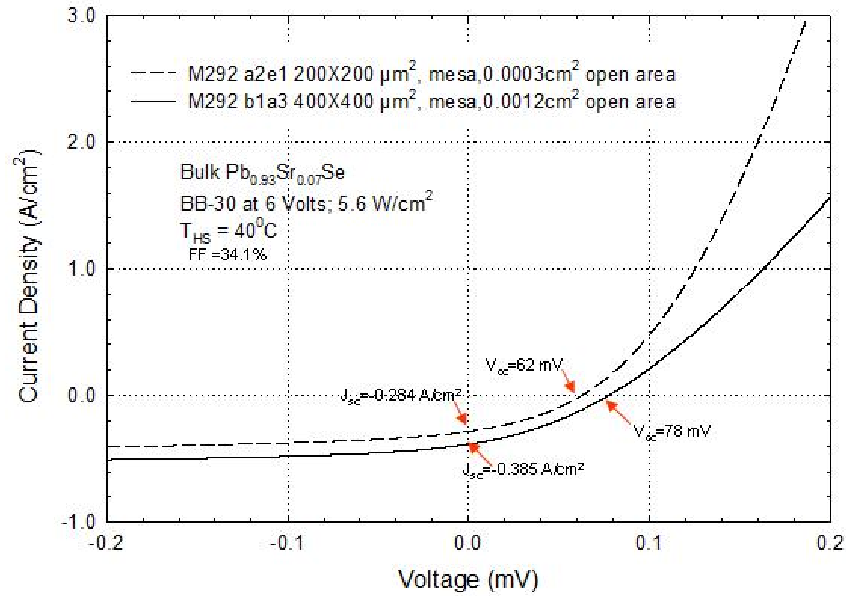

Figure 4.17:. Current density versus voltage characteristics plot of M292 a2e1 and b1a3 at 40°C.

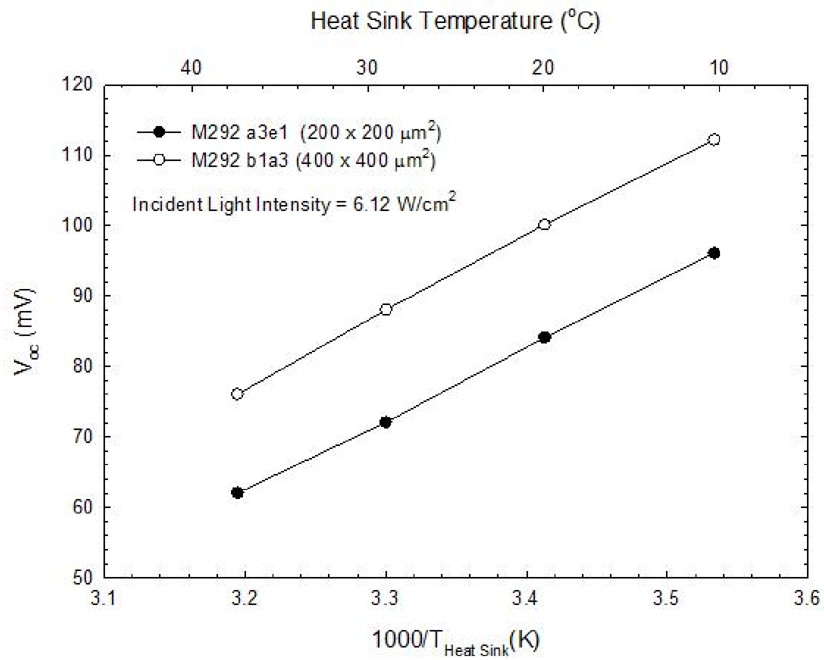

Figure 4.18: A plot of measured open circuit voltage vs heat sink temperature for M292 a2e1 and b1a3.

Figure 4.18 is the plot of open circuit voltage vs heat sink temperature for M292 a2e1 and b1a3 showing how open circuit voltage decreases with the increase in heat sink temperature.

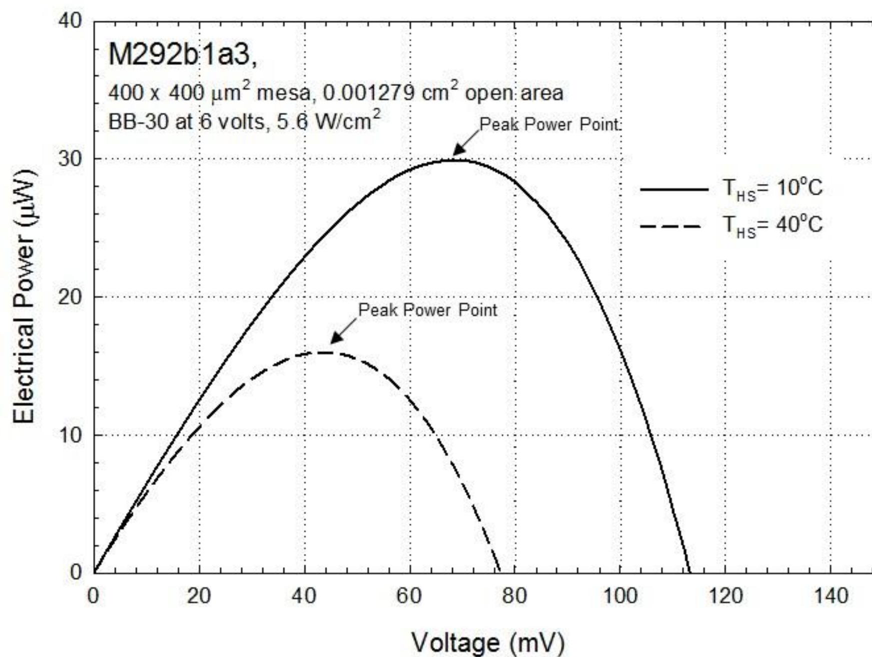

Figure 4.19: Electrical power generated by M292 b1a3 at heat sink temperatures of 10^0C and 40^0C.

Figure 4.19 is a plot of electrical power generated by the pn junction device while it is illuminated with broadband thermal radiation. It shows results for two different heat sink temperatures, 10°C and 40°C. Peak powers of 30 µW (18.8 mW/cm^2) at 10°C and 16 µW (10.0 mW/cm^2) at 40°C are demonstrated for this 400 µm x 400 µm mesa sized device.

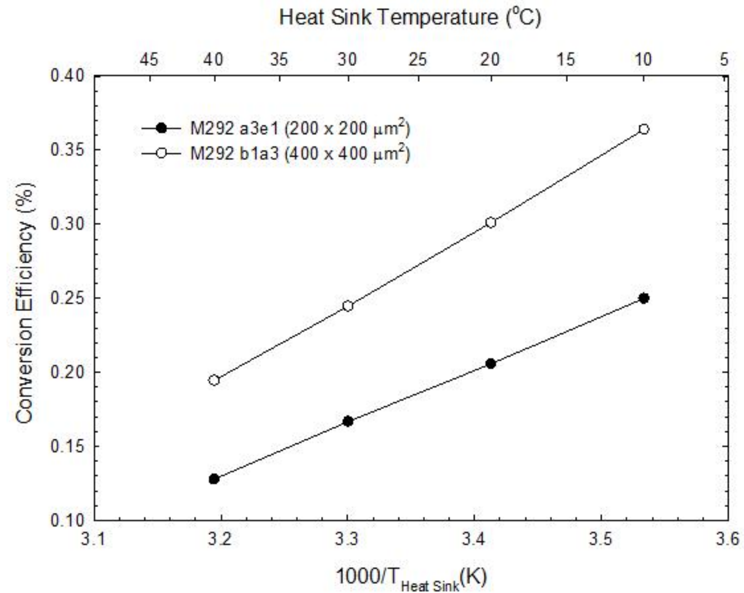

Figure 4.20: Power conversion efficiency vs heat sink temperature for M292 a2e1 and b1a3. Conversion efficiency is calculated by taking the ratio of electrical output power density of M292 over the incident broadband thermal radiation power density.

Figure 4.20 is a plot of the power conversion efficiency as a function of heat sink temperature for the two different mesa sized devices. The larger mesa sized device shows a consistently larger power conversion efficiency with a maximum value of 0.36% for these testing conditions.

4.6 Discussion

The efficiency is the most commonly used parameter to compare the performance of one TPV cell to another. The efficiency of a TPV cell is determined as the fraction of incident thermal radiation optical power which is converted to electricity and is defined as:

$$y = \frac{V_{OC} I_{SC} FF}{P_{in}} \tag{4.1}$$

where V_{OC} is the open-circuit voltage; I_{SC} is the short-circuit current; FF is the fill factor, P_{in} is the input power and y is the efficiency. The open circuit voltage and, to a lesser extent, the short circuit current depend on temperature. The short-circuit current (I_{sc}) is proportional to the number of generated charge carriers collected by the metal contacts. It strongly depends on the generation rate of charge carriers and diffusion length. Diffusion length increases by lowering the temperature as there is a significant reduction in phonon scattering. However, short circuit current depends on bandgap or how many carriers are absorbed by the cell. The positive temperature coefficient of the band gap in lead chalcogenides, unlike many other semiconductors, is favorable for TPV materials. The temperature dependent gap in IV-VI materials is known to be due to both lattice expansion and electron-phonon interactions [9]. Considering the thermodynamic role of the band gap as chemical potential for the mass action law and taking into account the entropy contributions the temperature coefficient the effect can be described by $\frac{dE_g}{dT} = \left(\frac{dE_g}{dT}\right)_V + \frac{3r_L}{K}\left(\frac{dE_g}{dP}\right)_T$,where r_L is the linear thermal

expansion coefficient $\left(\frac{1}{L}\left(\frac{dL}{dT}\right)_P\right)$, K is the bulk modulus $\left(\frac{-1}{V}\left(\frac{dV}{dP}\right)_T\right)$, $\left(\frac{dE_g}{dT}\right)_V$ describes the electron -phonon interactions and $\left(\frac{dE_g}{dP}\right)_T$ describes the bandgap dependent pressure [10]. The energy gap and effective masses of $Pb_{0.93}Sr_{0.07}Se$ system depends on temperature according to eq. (3.1). The effect of temperature on short circuit current is not very significant. However open circuit voltage depends significantly on temperature. From eq (2.5) considering $J_{dark} \approx J_{sc}$.The temperature dependence of V_{oc} can be obtained.

$$\frac{\partial V_{oc}}{\partial T} = \frac{V_{oc}}{T} + \frac{kT}{q}\left(\frac{\partial J_{sc}}{J_{sc}\partial T} - \frac{1}{J_0}\frac{\partial J_0}{\partial T}\right) \tag{4.2}$$

Reverse saturation current density, J_0, is a measure of the leakage of minority carriers across the p–n junction in reverse bias. This leakage is a result of minority carrier drift across the depletion region and carrier recombination in the neutral regions on either side of the junction, and therefore, J_0, primarily controls the value of V_{oc} in the TPV cells. The minority carriers are thermally generated; therefore, J_0 is highly sensitive to temperature changes. Reverse saturation current density, J_0 for a p–n junction solar cell, has been modeled as discussed in eq (2.3). Thus by combining eqs. (2.23) and (2.24) one can write.

$$J_0 = C \times T^3 \times e^{\frac{-E_g}{k_B T}} \tag{4.3}$$

In the above equation, doping and the material parameters of TPV cells are combined in this one constant C [11]. The important TPV cell parameters for the model calculations are the temperature and bandgap. The higher the bandgap the lower will be the saturation current density. Green has proposed a simple empirical relation for J_0 where the product $C \times T^3$ is replaced by a constant A $(A = 1.5 \times 10^8 mAcm^{-2})$ [12].

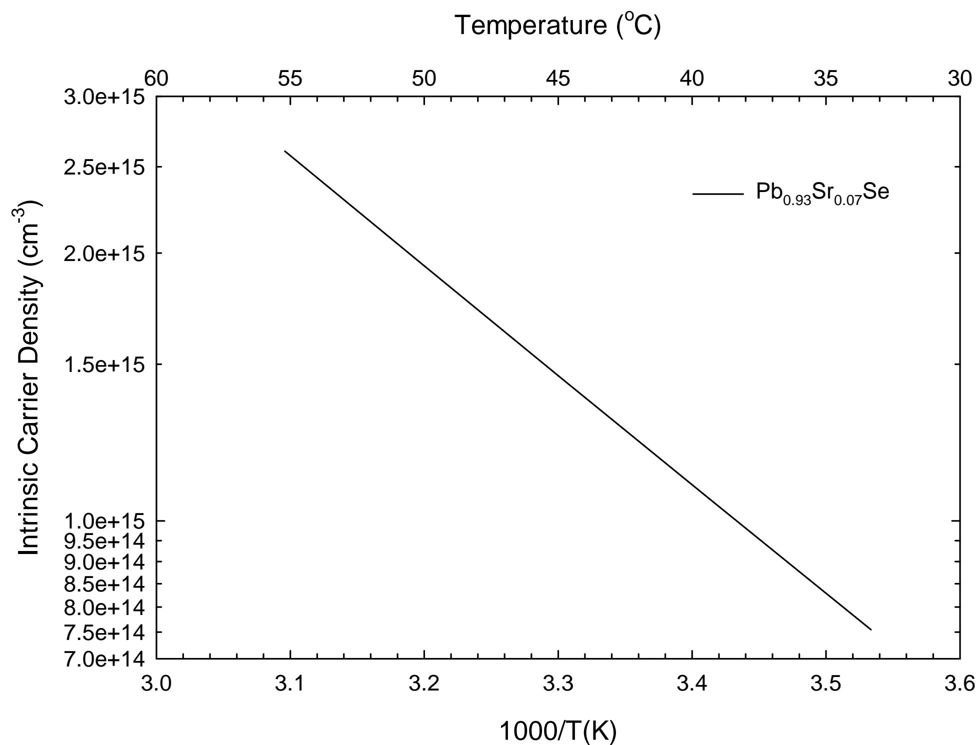

Figure 4.21: Arrhenius plot of intrinsic carrier density of $Pb_{0.93}Sr_{0.07}Se$ from 30^0C to 60^0C calculated using electron and hole effective masses of 0.11 m_o in four-fold degenerate L-valleys.

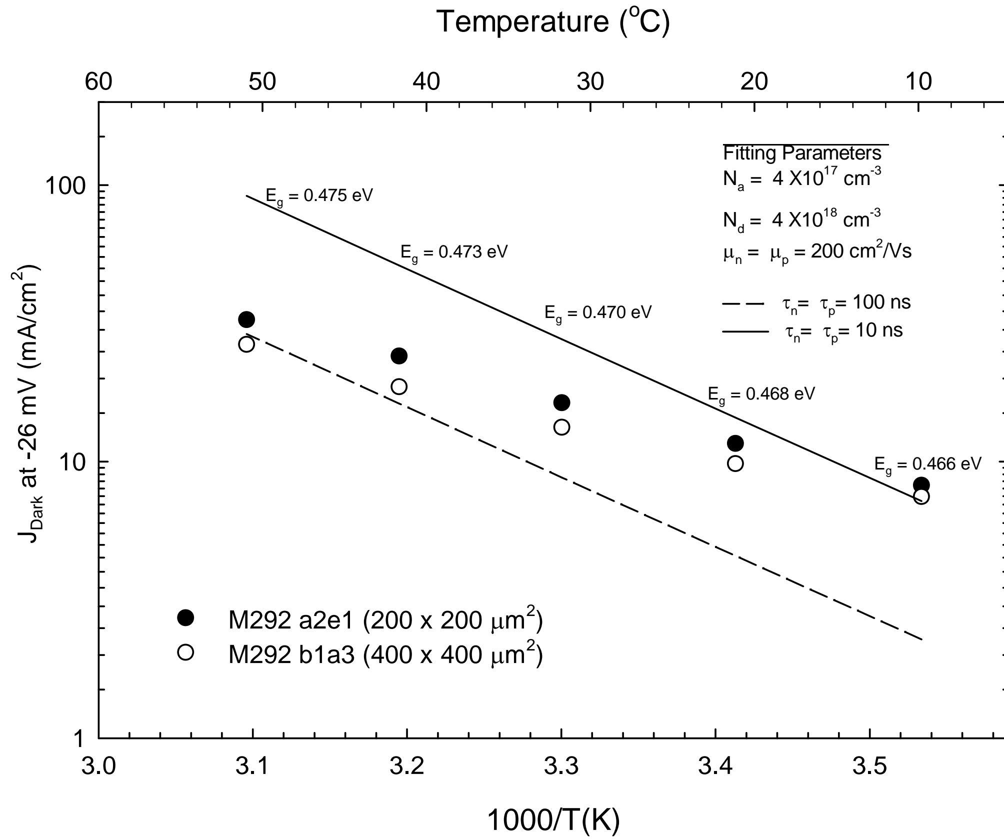

Figure 4.22: Calculated Arrhenius plots of reverse bias saturation current for a $Pb_{0.93}Sr_{0.07}Se$ pn junction from 30^0C to 60^0C with minority carrier lifetimes of 10 ns and 100 ns along with measured dark current data at -26 mV for two different devices.

Fig 4.22 plots measured dark current densities at a -26 mV reverse bias as a function of inverse temperature for the two pn junction device structures discussed above along with calculated dark currents using equation (4.4).

$$J_0 = \frac{qM_c M_v}{2}\left(\frac{\sqrt{m_h^* m_e^*}k_B T}{f\hbar^2}\right)^3\left(\sqrt{\frac{D_n}{\tau_n}}\frac{1}{N_A}+\sqrt{\frac{D_p}{\tau_p}}\frac{1}{N_D}\right)e^{\frac{-E_g}{k_B T}} \quad (4.4)$$

The n-type and p-type side doping values and electron and hole mobilities used are based on Hall effect measurements as discussed above. Two lines are calculated, one that assumes a 10 ns minority carrier lifetime, and one that assumes a 100 ns minority carrier lifetime. It is interesting that there are good fits to the measured data for a 10 ns minority carrier lifetime at 10°C and a 100 ns minority carrier lifetime at 50°C. Although the bandgap increases with temperature the 9 meV change is not that significant as shown in Fig 4.22. Increasing minority carrier lifetime can be explained by the phenomenon of thermal re-excitation from recombination center defect levels in the bandgap. Dark current is a thermally activated processes and follows an Arrhenius behavior where the activation energy is the bandgap energy. However, the pre-exponential coefficient in Equation 4.4 also includes terms that are temperature dependent. For example, minority carrier lifetime can increase with increasing temperature due the thermal excitation effect [13]. Therefore, the change in minority carrier lifetime with change in temperature is due to the fact that lifetime ‡ increases with temperature due to thermal reexcitation from recombination centers. A thermalized carrier can be trapped in deep traps or recombination centers immediately before recombining or stay for a long time in the shallow traps (with thermal re-excitation into the bands and re-trapping) before it is eventually captured by a recombination center. The minority-carrier recombination lifetime (‡$_{SRH}$) via the deep level is defined by the Shockley-Read-Hall (SRH) model [14, 15]. In the original paper of Shockley and Read [14], a model was presented describing the behavior of ‡ according to temperature and doping for n and p type semiconductors. In an n-type

semiconductor where the Fermi level at thermal equilibrium $F_0 > E_i$ (the intrinsic level) and $n_0 >> p_0$ the increase of lifetime with temperature is given by

$$\ddagger = \ddagger_{p0}(1 + n_1/n_0) = \ddagger_{p0}\left[1 + \exp\frac{(E_t - F_0)}{kT}\right] \tag{4.5}$$

Similarly for a p type semiconductor $F_0 < E_i$ and $p_0 >> n_0$

$$\ddagger = \ddagger_{n0} + \ddagger_{p0} n_1/p_0 = \ddagger_{n0} + \ddagger_{p0}\exp\left[\frac{(E_t + F_0 - 2E_i)}{kT}\right] \tag{4.6}$$

where $\ddagger_{p0}$ is the lifetime of holes in an n type semiconductor, $\ddagger_{n0}$ is the lifetime of electrons in a p type semiconductor and p_1 and n_1 are the concentrations of holes and electrons related to the E_t (the trap impurity level) respectively.

Equations (4.5) and (4.6) show that minority carrier lifetime increases exponentially with temperature. Therefore, the experimental dark current data do not follow the exact slope of the calculated Arrhenius plots for reverse bias saturation current, J_o, because there is an exponentially dependent temperature term in the preexponential coefficient of eq. (4.4).

4.7 Recombination & Minority Carrier Lifetime for Effect of Carrier lifetime for $Pb_{0.93}Sr_{0.07}Se$ based TPV device

Carrier lifetime depends on the recombination process. The generation processes which compete against the recombination processes directly affect the performance of a TPV cell [16]. Recombination processes in for IV-VI materials are widely discussed in the literature [17, 18]. The carrier recombination mechanisms in semiconductor devices are classified into radiative, Shockley-Read-Hall (SRH), Auger, and surface or

recombination. Among them, SRH and surface recombination are determined by material quality. The following is a discussion of different recombination processes that are prevalent in semiconductor materials and devices.

Radiative Recombination:

For the radiative process, in case of the Boltzmann statistics, the carrier lifetime is determined by [18]: The formula for the recombination rate $‡_r$ for band-to-band transitions for the IV-VI materials can be represented in a general way

$$‡_r = W \sum_q \int_{Š_{\min(q)}}^{\infty} \frac{dŠ}{2f} 4 D_i(q,Š) I_m \mathrm{V}_{cv}(q,Š) f_B\left(\frac{hŠ}{k_B T_L} - \mathrm{y}_c + \mathrm{y}_v\right) \times \left[1 + f_B\left(\frac{\hbar Š}{k_B T_L}\right)\right] \qquad (4.7)$$

$f_B(x)$ is the Bose function $\frac{1}{e^x - 1}$, y_c and y_v electronic quasi-Fermi levels for conduction and valence band states, respectively, in units of $k_B T_L$. k_B is the Boltzmann constant and T_L the lattice temperature. The factor W accounts for the many-valley structure of lead chalcogenides, i.e. W= w or (w-1) depending on whether processes is near a definite L-point or between equivalent L-points are regarded, w being the number of equivalent valleys. $\mathrm{V}_{cv}(q,Š)$ is the interband contribution of the dielectric function, i.e. $I_m \mathrm{V}_{cv}(q,Š) f_B\left(\frac{hŠ}{k_B T_L} - \mathrm{y}_c + \mathrm{y}_v\right)$ accounts for the statistical weight of interband transitions with exchange of energy $hŠ$ and momentum q. The function $D_i(q,Š)$ is related to the probability that a system interacting with electrons absorbs or emits the energy $hŠ$ and the momentum q. More relevant to TPV devices is the compilation by Charache [19] of experimental dark

current values in low bandgap semiconductor p-n junctions. j_0 decreases with increasing minority carrier lifetime, but there is a well known theoretical limit to minority carrier lifetime imposed by radiative recombination phenomena. This limit depends on whether photon recycling effects are operative, as can be affected and enhanced by a bandpass filter or a backside reflector. Photon recycling refers to the re-absorption of photons produced by radiative recombination of minority carriers. Whereas the re-absorbed photon generates a minority carrier. Photon recycling can increase the effective minority carrier lifetime by about an order of magnitude [20,21]. Another interesting part of radiative recombination which can play an advantageous role in a PV/TPV cell is the re-excitation and re-emission of photons causing electron hole pairs before they are extracted. The Shockley-Queisser (SQ) formulation [16] idealizes a solar cell to have no imperfections or defects. At the open-circuit condition, the only mechanism constraining the build-up of electrons and holes is the re-emission of photons out through the front surface. Miller et al [22] generalized this to include an extra parameter: the internal luminescence yield y. The internal luminescence yield is defined as the probability of an absorbed photon being re-emitted within the PV/TPV cell (as opposed to being lost to e.g. Auger or Shockley-Read-Hall recombination), without regard to what happens after re-emission.

Many materials have intrinsic limits to their internal luminescence yield representing a second important variable to be included in efficiency limits. The emission rate through the front surface, at non equilibrium, equals the equilibrium absorption rate scaled up by the electron-hole product $\frac{np}{n_i^2} = e^{\frac{qV}{kT}}$ [23]. As Miller et al

reported [22], we can write the general loss rate per unit volume as R_{loss} then the loss rate per unit area is simply $R_{loss}L$, where L is the thickness of the PV/TPV cell,

$$V_{oc} = \frac{kT}{q}\ln\left(\frac{\iint \alpha(E,\theta)S(E)\cos\theta\, dE d\Omega}{\iint \alpha(E,\theta)b(E)\cos\theta\, dE d\Omega}\right) - \frac{kT}{q}\left|\ln(\eta_{ext})\right| \tag{4.8}$$

Eq. (4.8) was first recognized by Ross [24]. From the above equations and using the SQ simplifying assumptions [16] Miller et al [22] came up with the generalized Shockley-Queisser equations:

$$\frac{J}{q} = af\int_{E_g}^{\infty} S(E)dE - \left(a + 4n_r^2\alpha L\frac{1-\eta_{int}}{\eta_{int}}\right)fe^{\frac{qV}{kT}}\int_{E_g}^{\infty} b(E)dE \; ; \; \frac{J_{sc}}{q} = af\int_{E_g}^{\infty} S(E) \tag{4.9}$$

$$\frac{qV_{OC}}{kT} = \ln\left(\frac{\int_{E_g}^{\infty} S(E)dE}{\int_{E_g}^{\infty} b(E)dE}\right) - \ln\left(1 + 4n_r^2\frac{\alpha L}{a}\frac{1-\eta_{int}}{\eta_{int}}\right) \tag{4.10}$$

where α is absorbance at energy E and n_r is the refractive index. The original SQ equations [16] depend on bandgap, and these equations have an additional, strong dependence on η_{int}.

Shockley Read Hall (SRH)

The SRH mechanism is not an intrinsic and fundamental process as it occurs via levels in the forbidden energy gap. It depends on the quality of the material. The reported positions of SRH centers for both n- and p-type materials range anywhere from near the valence band to near the conduction band. SRH recombination can be formulated as

$$R_{SRH} = \frac{(np - n_i^2)}{\ddagger_n (p + n_i) \ddagger_p (n + n_i)} \tag{4.11}$$

Where $\ddagger_{n,p}$ are SRH lifetimes.

Surface Recombination

For a single defect at the surface, the rate of surface recombination can be written as

$$R_{SRV} = \frac{S_n S_p (np - n_i^2)}{S_n (p + n_i) + S_p (n + n_i)} \tag{4.12}$$

Where $S_{n,p}$ are effective surface recombination velocities. Any defects or impurities within or at the surface of the semiconductor promote recombination. The high recombination rate in the vicinity of a surface depletes this region of minority carriers. Localized region of low carrier concentration causes carriers to flow into this region from the surrounding, higher concentration regions. Therefore, the surface recombination rate is limited by the rate at which minority carriers move towards the surface. The defects at a semiconductor surface are caused by the interruption to the periodicity of the crystal lattice, which causes dangling bonds at the semiconductor surface. The reduction of the number of dangling bonds, and hence surface recombination, is achieved by surface passivation. As discussed before, the surfaces or interfaces of a substrate represent a severe discontinuity in its crystalline structure. The large numbers of partially bonded atoms give rise to many dangling bonds, and therefore, a large density of defect levels are found within the bandgap near the semiconductor surface.

Auger Recombination

For the carrier lifetime depending on Auger's process, the relationship is given by

$$\ddagger_A = [C_A (N_A^2 + 2n_i^2)]^{-1} \tag{4.13}$$

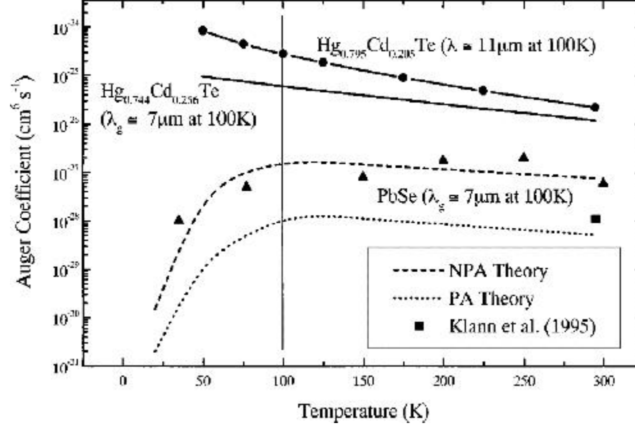

Figure 4.23: Auger coefficient (IV –VI materials) vs temperature [25].

In the case of $N_A >> n_i$ the simplified Auger carrier lifetime equation is derived as $\ddagger_A = (C_A N_A^2)^{-1}$ .The Auger recombination coefficient $C_A = 8\times10^{-28}$ is defined in [25, 26].

$$C_A = \frac{3q^4 (2f)^{\frac{5}{2}} (k_B T)^{\frac{1}{2}} E_g^{\frac{-7}{2}} h^3}{(16f \mathrm{V}_0 \mathrm{V}_\infty)^2 m_l^{*\frac{1}{2}} m_t^{*\frac{3}{2}}} \times e^{\frac{E_g}{2k_B T}\left(\frac{m_l^*}{m_t^*}\right)^{-1}} \tag{4.14}$$

where m_l^* and m_t^* are the longitudinal and transverse effective masses. Auger and radiative mechanisms are determined by energy band structures, therefore those two are fundamentally limiting factors for the overall generation-recombination processes.

VI-VI materials have a multi-valley band structure with band extrema at the L-point of the Brillouin zone. The absence of a heavy-hole band reduces the nonradiative

Auger recombination rate, one or two orders of magnitude below that of comparable narrow gap III-V and II-VI materials [25]. This is favorable for the reduction of the high temperature dark current.

Total Recombination

Effective decay time of carriers in the active layer is the sum of the contribution from bulk and surface recombination, as given by the equation

$$\frac{1}{\tau_{eff}} = \frac{1}{\tau_{rad}} + \frac{1}{\tau_{SRH}} + \frac{1}{\tau_{Aug}} + \frac{\#ofsurfaces \times SRV}{W} \tag{4.15}$$

The recombination time of free excess carriers in these IV-VI compounds is an important parameter limiting the efficiency of devices. Enhanced non radiative recombination rates are expected for higher carrier density devices such as laser diodes , but this will not be the case for TPV devices which will have relatively low carrier densities even for the most intense illumination power densities from hot radiators. Thus radiative recombination will be the primary mechanism that plays the key role in TPV cell performance.

4.8 Assessment of Fabricated IV-VI Semiconductor Devices

The measurements of the fabricated IV-VI semiconductor devices described here are consistent with minority carrier lifetimes that are in the range of 10 ns to 100 ns. When compared to other direct gap semiconductor device materials, these lifetimes are as long or even longer. This result shows that SRH and surface recombination are not dominating problems and that IV-VI semiconductor materials quality is sufficiently good to fabricate useful devices. This conclusion is particularly significant considering the fact that the materials were grown on silicon and

transferred to copper during device processing. These results therefore not only show that IV-VI materials are highly viable candidates for TPV device fabrication with no fundamental surface state problems that would give high surface recombination velocities, but that low cost silicon growth substrates and thermally conductive copper host substrates for good thermal management in a TPV generator can be used as part of a low cost TPV cell manufacturing technology.

4.9 Summary and Conclusions

This chapter described the epitaxial growth of IV-VI semiconductor $Pb_{0.93}Sr_{0.07}Se$ bulk pn junction structures, fabrication of these materials into testable TPV devices, and current versus voltage characterization without and with broadband illumination from a thermal radiator. Analysis of dark current, open circuit voltage and efficiency were conducted. A maximum open circuit voltage of 113 mV was demonstrated for a 450 meV bandgap material and minority carrier lifetimes between 10 ns and 100 ns depending on lattice temperature were determined.

References

[1] Cho A Y, 1991, Advances in molecular beam epitaxy (MBE) Journal of Crystal Growth Vol. 111 1.

[2] Furuya K, and Miyamoto Y, 1990, GaInAsP/InP organometallic vapor phase epitaxy for research and fabrication of devices, Int. J. High Speed Electronics Vol. 1 347.

[3] P. J. McCann, “IV-VI Semiconductors for Mid-Infrared Optoelectronic Devices”, Mid-Infrared Semiconductor Optoelectronics, p. 237, edited by A. Krier, Springer-Verlog, London (2006).

[4] A. Ishizaka and Y. Shiraki, “Low Temperature Surface Cleaning of Silicon and its Application to Silicon MBE,” *J. Electrochem. Soc.* **133**, 666 (1986).

[5] Y. F. Li, P. J. McCann, A. Sow, C. Yao, and P. C. Kamat, “Improvement of Heat Dissipation Through Transfer of IV-VI Epilayers From Silicon to Copper”, IEEE Photonics Technology Letters 16, 2433 (2004).

[6] A Rogalski, “HgCdTe infrared detector material: history, status and outlook” Institute Of Physics Publishing Reports On Progress In Physics; Rep. Prog. Phys. 68 (2005) 2267–2336.

[7] P. J. McCann, K. Namjou, and X. M. Fang, Appl. Phys. Lett. 75, 3608 (1999).
[8] X. M. Fang, K. Namjou, I. N. Chao, P. J. McCann, N. Dai, and G. Tor, J. Vac. Sci. Technol. B 18, 1720 (2000).

[9] Zachary M. Gibbs, Massoud Kaviany, Hyoungchul Kim and G. Jeffrey Snyder, Heng Wang, Robert L. White,Temperature dependent band gap in PbX (X =S, Se, Te); Applied Physics Letters 103, 262109 (2013).

[10] Zachary M. Gibbs; Band Engineering in Thermoelectric Materials Using Optical, Electronic, and Ab-Initio Computed Properties. Dissertation thesis California Institute of Technology 2015.

[11] M.E. Nell, A.M. Barnett, The spectral p–n junction model for tandem solar-cell design, IEEE Transactions on Electron Devices 24 (1987) 257–266.

[12] M.A. Green, Solar Cells, Prentice-Hall, Englewood Cliffs, NJ, 1982, p. 88.

[13] Y. Hayamizu, T. Hamaguchi, S. Ushio, T. Abe and F. Shimura " Temperature dependence of minority-carrier lifetime in iron-diffused P-type silicon wafers " J. Appl. Phys. 69 (5), 1 March 1991.

[14] W.Shockley and W.T. Read,Jr." Statistics of the Recombinations of Holes and Electrons" PHYSICALREVIEW; Volume 87, Number 5, September 1st 1952.

[15] R. N. Hall " Electron-Hole Recombination in Germanium" General Electric Research Laboratory, Schenectady, New York; May 8th 1952.

[16] Shockley, W., Queisser, H.J., " Detailed Balance Limit of Efficiency of pn Junction Solar Cells" Journal of Applied Physics, 32, 510 (1961).

[17] Antoni Rogalski, " Infrared detectors: status and trends" Progress in Quantum Electronics Volume 27, Issues 2–3, 2003, Pages 59–210.

[18] O. Ziep, D. Genzow, M. Mocker and K. H. Herrma " Nonradiative and Radiative Recombination in Lead Chalcogenides" phys. stat. sol. (b) 99, 129 (1980) Subject classification: 13.1 and 20.3; 22.

[19] G. Charache, GaSb-related materials and devices, Thermophotovoltaic Generation of Electricity, Fourth NREL Conf., American Inst. Physics Conf. Proc., 460, T.J. Coutts, C.S. Allman, and J.P. Benner, eds., 1998, pp 10-11.

[20] R. Arhenkiel, Minority carrier lifetime in compound semiconductors, Ch.1 in Current Topics in Photovoltaics, vol. 3, T.J. Coutts, J.D. Meakin, eds., (Academic Press, 1988).

[21] J.E. Parrott, Radiative recombination and photon recycling in photovoltaic cells, Solar Energy Materials 30 (1993) 221-231.

[22] Owen D. Miller and Eli Yablonovitch, "Photon extraction: the key physics for approaching solar cell efficiency limits," Proc. SPIE 8808, Active Photonic Materials V, 880807 (11 September 2013).

[23] Kittel, Introduction to Solid State Physics, Vol. 7. Wiley New York, 1976.

[24] R. T. Ross, Thermodynamic limitations on the conversion of radiant energy into work," The Journal of Chemical Physics, vol. 45, no. 1, pp. 17, 1966. doi: 10.106 3/1.1727289 .

[25] P.C. Findlay and C.R.Pidgeon " Auger recombination dynamics of lead salts under picosecond free eletron laser excitation " physical review B. Volume 58, Nov 19; 15 November 1998-1.

[26] P. R. Emtage " Auger recombination and junction resistance in lead tin telluride"J. Appl. Phys. 47, 2565 (1976); http://dx.doi.org/10.1063/1.322975

Chapter 5

Characterization of a IV-VI Semiconductor TPV Device using a Bandpass Filter and a Winston Cone.

What we observe is not nature itself,
but nature exposed to our method of questioning.
Werner Heisenberg

5.1 Introduction

A TPV generator system consists primarily of a combustion apparatus, a combustion-heated radiator, and photovoltaic cells. TPV generator efficiency is enhanced with a radiator that selectively emits thermal photons with energies that are well matched to the band gap of the TPV cells. In addition, TPV generator efficiency is significantly improved when thermal photons are optically directed towards the TPV cells. This chapter describes experimental testing procedures that accurately simulate the environment that a TPV cell would experience in a well-designed TPV generator system. A mid-infrared bandpass filter and a compound parabolic concentrator (Winston cone) were used to filter the spectrum and direct the photon flux from a resistance-heated thermal radiator. The techniques described here, which have not been previously described in the TPV literature, provide a new way to determine important TPV device figures of merit such as power conversion efficiencies and external quantum efficiencies (EQEs). Further and broader use of these device characterization methods will allow the TPV research community to compare experimental results more effectively thus facilitating advances in the field.

A well-matched band pass filter will limit the spectral range of incident photons to energies that are just slightly larger than the band gap energy of the TPV cell

material. Power conversion efficiency is improved with a spectral filter because there is a smaller quantum defect. In other words, elimination of high energy photons reduces the amount of energy that is dissipated by phonon emission as photo-generated carriers relax to the band edges. An additional benefit of using a bandpass filter in a TPV test setup is that it allows the experimental determination of external and internal quantum efficiencies. This is because a much more narrow range of photon energies is incident on the device and this allows a more accurate calculation of photon flux than would be possible with a broadband thermal radiation source that is not spectrally filtered.

The use of reflective surfaces is an effective way to direct divergent photons from a thermal radiator to a TPV cell. At the same time, it is useful to concentrate as much infrared light as possible to a small area. A Winston cone is a non-imaging optical element that collects and concentrates light. Winston cones have been used to concentrate sunlight, for example, and have been used to achieve optical power densities that are greater than those that are at the surface of the sun [1]. The concentrated light exiting a Winston cone will illuminate a much smaller area than if such an optical element were not used. This is a useful feature when it comes to testing small experimental TPV devices since excess illumination, light that is incident on areas of a chip that are adjacent to a mesa-etched device structure, for example, does not unnecessarily heat the whole chip. Confining the incident light to just the area of a TPV device will more accurately simulate a TPV cell in a well-designed generator since a more mature technology will involve larger TPV devices that are matched in size to the illumination area from a thermal radiator.

5.2 Bandpass Filter

In order to use a source of blackbody radiation to produce TPV cell electricity efficiently the correct sort of radiation must be arriving at the cell. Only light below a certain wavelength $\}_g$ will generate a voltage in the cell. Ideally, to increase efficiency long-wavelength light is recycled by reflection back to the radiator from the TPV cell. This is what occurs with the device structures fabricated as part of this study since the TPV device material is bonded with metal to a copper substrate and low energy photons that pass through the TPV semiconductor material will be reflected back. Nevertheless, reflectivity is not 100%, so there will be some unnecessary heating due to low energy photon absorption. Thus it is important to discuss an optimal "bandpass filter" that is matched to the TPV cell. A bandpass filter can consist of a number of thin layers with differing refractive indices. The combination of multiple reflections and refractions, with associated change of phase, results in interference so that light of certain frequencies is mostly reflected back while other light is mostly transmitted through to the other side of the filter.

The key element of designing a bandpass filter is the calculation of transmittance and reflectance of the incoming photon flux. The transmittance and reflectance can be calculated by modeling the bandpass filter material as a transmission line. The structure is considered homogenous on the plane perpendicular to the direction of propagation. The positive z axis is the direction of propagation, then $\bar{k} = k_z \hat{z}$, where $k_z = \frac{2fn}{\}}$ the propagation constant, n is the refractive index and $\}$ is the wavelength.

The goal is to find a 2×2 transmission matrix $\left[M_1^T\right]$, according to the parameters shown in Figure 5.1.

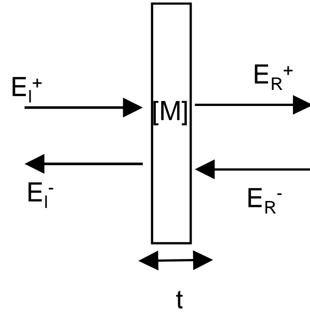

Figure 5.1: Transfer matrix parameters.

Equation 5.1 shows use of the transmission matrix for normally incident rays with no change in refractive index. The easiest case is the one where there is no change in refractive index between the two points at which the electric fields are evaluated. This corresponds to the uniform portion of the structure between any two interfaces. In this case only the phases of the electric fields are changed.

$$\begin{bmatrix} E_I^+ \\ E_I^- \end{bmatrix} = \begin{bmatrix} e^{-j„} & 0 \\ 0 & e^{j„} \end{bmatrix} \begin{bmatrix} E_R^+ \\ E_R^- \end{bmatrix} = [T] \begin{bmatrix} E_R^+ \\ E_R^- \end{bmatrix} \qquad (5.1)$$

In Equation 5.1 $„ = k_z t$ and t = thickness of the layer. To find out how electric field changes across a boundary as refractive index changes from n_I to n_R the two electric field components E_R^+ and E_R^- need to be converted into the total transverse electric and magnetic fields with the help of Maxwell's equations.

$$\vec{E} = \vec{E}^{+} + \vec{E}^{-} \Rightarrow E_R^{\perp} = E_R^{+} + E_R^{-} \tag{5.2}$$

$$\vec{k} \times \vec{H} = -\check{S}\vee_R \vec{E} \Rightarrow H_R^{\perp} = -n_R (E_R^{+} - E_R^{-}) \tag{5.3}$$

$$\begin{bmatrix} E_R^{\perp} \\ H_R^{\perp} \end{bmatrix} = \begin{bmatrix} 1 & 1 \\ -n_R & n_R \end{bmatrix} \begin{bmatrix} E_R^{+} \\ E_R^{-} \end{bmatrix} \tag{5.4}$$

where the superscript symbol $\perp$ indicates the transverse component. Here, $\vee = n^2$ and $\sim = 1$ (no magnetic material in the structure) were considered. Then the dispersion relation becomes $\left|\vec{k}\right|^2 = \check{S}^2 \sim \vee$. Now the matrix B can be defined as

$$B = \begin{bmatrix} +1 & +1 \\ -n & +n \end{bmatrix} \tag{5.5}$$

Therefore

$$\begin{bmatrix} E_R^{\perp} \\ H_R^{\perp} \end{bmatrix} = \left[B_R\right] \begin{bmatrix} E_R^{+} \\ E_R^{-} \end{bmatrix} \tag{5.6}$$

where $\left[B_R\right] = \begin{bmatrix} +1 & +1 \\ -n_R & +n_R \end{bmatrix}$. Without a “current sheet” across the surface of the boundary, the transverse electric and magnetic fields are continuous.

$$\begin{bmatrix} E_I^{\perp} \\ H_I^{\perp} \end{bmatrix} = \begin{bmatrix} E_R^{\perp} \\ H_R^{\perp} \end{bmatrix} \tag{5.7}$$

$$\begin{bmatrix} E_I^{+} \\ H_I^{-} \end{bmatrix} = \left[B_I\right]^{-1} \begin{bmatrix} E_I^{\perp} \\ H_I^{\perp} \end{bmatrix} = \left[B_I\right]^{-1} \left[B_R\right] \begin{bmatrix} E_R^{+} \\ E_R^{-} \end{bmatrix} \tag{5.8}$$

Where $\left[B_I\right]^{-1} = \begin{bmatrix} 1 - 1/n_I \\ 1 + 1/n_I \end{bmatrix}$.Thus Equation 5.8 can be written as

$$\begin{bmatrix} E_I^+ \\ H_I^- \end{bmatrix} = \frac{1}{2} \begin{bmatrix} 1 & -1/n_I \\ 1 & +1/n_I \end{bmatrix} \begin{bmatrix} +1 & +1 \\ -n_R & +n_R \end{bmatrix} \begin{bmatrix} E_R^+ \\ E_R^- \end{bmatrix} \tag{5.9}$$

When crossing a boundary the electric field vector can be multiplied by the matrix $[B_I]^{-1}[B_R]$. Layer 1 has thickness t_1, refractive index n_1, and is surrounded by vacuum of refractive index $n_0 = 1$. According to Figure 5.1, the electric field on the left of the layer is separated from that on the right by a boundary, a homogeneous layer and then another boundary

$$\begin{bmatrix} E_I^+ \\ E_I^- \end{bmatrix} = [B_0]^{-1}[B_1][T_1][B_1]^{-1}[B_0] \begin{bmatrix} E_R^+ \\ E_R^- \end{bmatrix} \tag{5.10}$$

Hence the Transmission Matrix can be written as:

$$[M_1^T] = [B_0]^{-1}[B_1][T_1][B_1]^{-1}[B_0] = \frac{1}{2} \begin{bmatrix} 1 & -1 \\ 1 & +1 \end{bmatrix} \begin{bmatrix} \cos\theta_1 & \frac{i\sin\theta_1}{n_1} \\ in_1\sin\theta_1 & \cos\theta_1 \end{bmatrix} \begin{bmatrix} +1 & +1 \\ -1 & +1 \end{bmatrix} \tag{5.11}$$

The matrix

$$\begin{bmatrix} \cos\theta_1 & \frac{i\sin\theta_1}{n_1} \\ in_1\sin\theta_1 & \cos\theta_1 \end{bmatrix} \tag{5.12}$$

is equivalent to the impedance matrix in the transmission line theory. It relates to the electric and magnetic fields at the two ends of the layer, it can be called matrix $[M_1]$. With a stack of N dielectric layers, as shown in Figures 5.2 and 5.3, the overall transmission matrix can be written as

$$[M^T] = [B_0]^{-1} \prod_{i=1}^{N} [M_i][B_{Sub}] \tag{5.13}$$

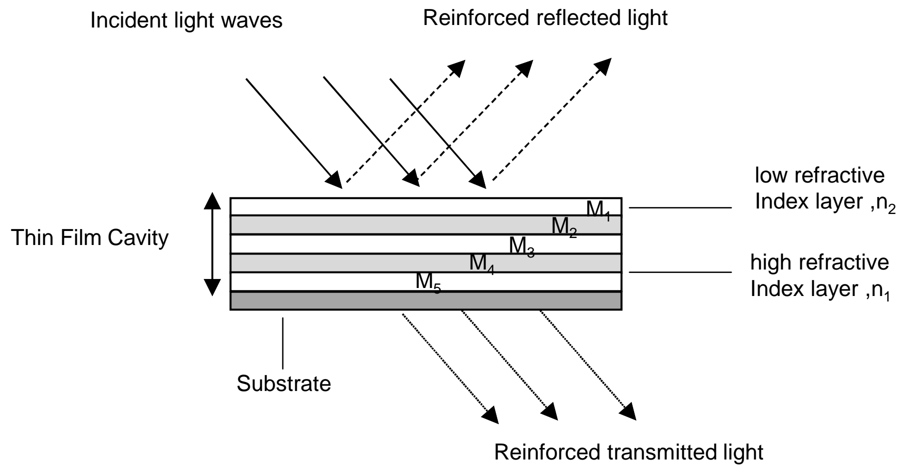

Figure 5.2: Transmission matrix for a dielectric stack.

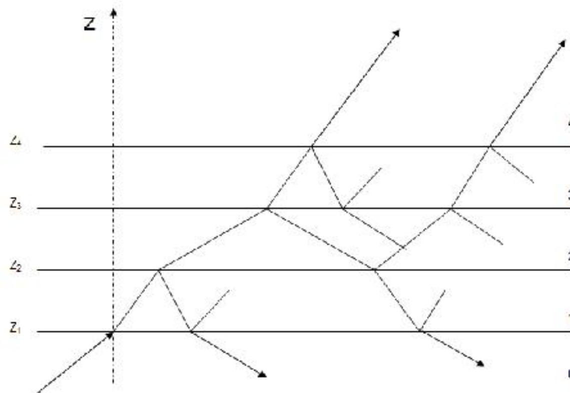

Figure 5.3: Multiple reflections and refractions for light moving from layer 0 to 1 to 2 …

where $[B_{sub}] = \begin{bmatrix} 1 & 1 \\ -n_{Sub} & n_{Sub} \end{bmatrix}$. Assuming $E_{Sub}^{-} = 0$; as light comes from the air side and the substrate extends to positive infinity (which is a good assumption if the substrate is thick)

$$\begin{bmatrix} E_0^+ \\ E_0^- \end{bmatrix} = [M^T] \begin{bmatrix} E_{Sub}^+ \\ E_{Sub}^- \end{bmatrix} = \begin{bmatrix} m_{11}^T & m_{12}^T \\ m_{21}^T & m_{22}^T \end{bmatrix} \begin{bmatrix} E_{Sub}^+ \\ 0 \end{bmatrix} = E_{Sub}^+ \begin{bmatrix} m_{11}^T \\ m_{21}^T \end{bmatrix} \quad (5.14)$$

Hence, reflectivity can be written as

$$r = \frac{E_0^-}{E_0^+} = \frac{m_{21}^T}{m_{11}^T} \quad (5.15)$$

and transmissivity can be written as

$$t = 1 + r = \frac{m_{11}^T + m_{21}^T}{m_{11}^T} \quad (5.16)$$

The reflectance R is

$$R = |r|^2 \ \ldots \quad (5.17)$$

and the transmittance T is

$$T = |t|^2 \quad (5.18)$$

Following conservation of energy rules, the transmittance (or transmission) can be written as T=1-R.

The use of the transfer matrix method outlined above and its use in spectral filter design is discussed in detail by Katsidis et al. [2]. A good bandpass filter is typically composed of two different materials with a large difference in refractive index and low absorption coefficients at the wavelengths of the desired transmitted light [3-5]. Two

materials that satisfy this requirement for a mid-infrared bandpass filter are $Pb_{0.724}Sr_{0.276}Se$ [6] and MgF_2. Table 5.1 lists the refractive indices and thicknesses for these materials as they can be used in the design of two different mid-IR bandpass filters, one with a center wavelength (CWL) at 5 microns and one with a CWL at 2.5 microns.

Table 5.1: Refractive indices, thickness, and the number of layers used for the design of two different bandpass filters. N= number of layer pairs; n_1 = refractive index of the first layer ($Pb_{0.724}Sr_{0.276}Se$); t_1 = thickness of the first layer; n_2 = refractive index of the second layer (MgF_2); t_2 = thickness of the second layer.

BP filter	N	n_1	t_1	n_2	t_2
CWL~5μm	5	5.9	0.28 μm	1.38	0.21 μm
CWL~2.5μm	5	5.9	58 nm	1.38	10 nm

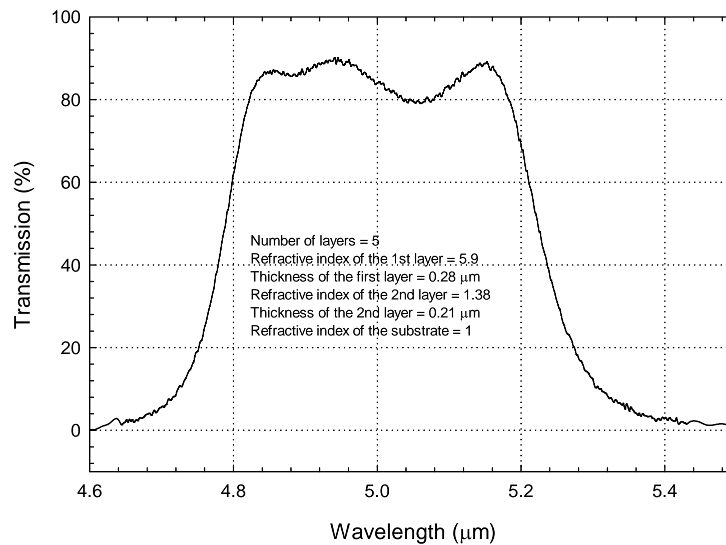

Figure 5.4: Transmission as a function of wavelength for dielectric filter (CWL~5μm). Plot is generated using the data from Table 5.1.

A MATLAB program (Appendix B) was written to implement the transfer matrix method outlined above, and it was used to generate the transmission spectra shown in Figures 5.4 and 5.5, which are for two different bandpass filter designs described in Table 5.1.

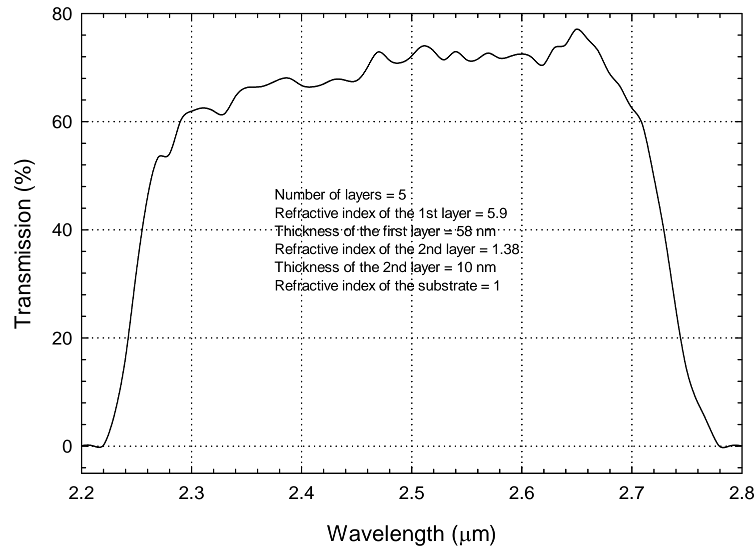

Figure 5.5: Transmission as a function of wavelength for dielectric filter (CWL~2.5μm).

A commercially available bandpass filter with a transmission spectrum similar to the 2.5 micron bandpass filter modeled above (Figure 5.5) was used for testing the TPV devices described in this dissertation. Figure 5.6 is the transmission spectrum provided by the vendor (Thorlabs) for the filter (part # FB2500-500) used in the TPV device test setup developed for this work. As discussed below, this bandpass filter is well matched to the band gap energy of the PbSrSe material used in the TPV devices that were fabricated.

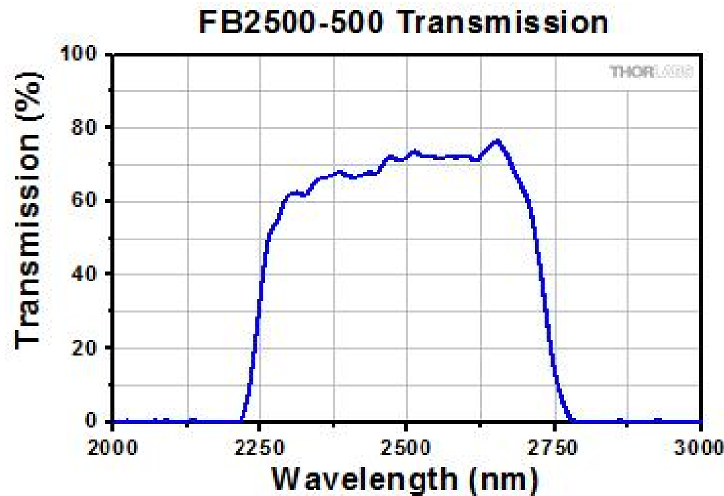

Figure 5.6: Transmission spectrum of Thorlab's IR bandpass filter (part # FB2500-500).

5.3 Winston Cone

A Winston cone is an off-axis parabola of revolution designed to maximize collection of incoming rays within a field of view [7-10]. It is a non imaging light concentrator intended to funnel all wavelengths passing through the entrance aperture and out through the exit aperture. It maximizes the collection of incoming rays by allowing off-axis rays to make a single bounce before passing out the exit aperture. A

commercially available Winston cone from Infrared Laboratories, Tuscon, AZ, with an entrance diameter of 0.5 inches, an exit diameter of 0.062 inches, and a length of 1.9 inches was used for testing the TPV devices described in this dissertation. Its principal functions are to concentrate the radiation from a thermal radiator and onto a mesa etched device structure. This cone has an inner reflective surface composed of electroplated gold. The geometric parameters of the Winston cone are shown in Table 5.2

Table 5.2: Winston cone entrance diameter, exit diameter, focal ratio (f), and the length of the cone.

Stock#	Cone entrance diameter(cm)	Cone exit diameter(cm)	Focal ratio (f)	Length of the cone (cm)
F3.80	1.27	0.157	3.8	4.8

The geometric field-of-view is defined as $\Theta = 2\theta = 2\sin^{-1}\left(\frac{a'}{a}\right)$ [11-12]. With a diameter ratio of 0.124, the field-of-view angle is 14.2 degrees. Therefore, off-axis light rays at an incident angle of less than 7.1 degrees will pass through the smaller diameter exit hole after a single bounce. Figure 5.7 shows the geometry of the Winston cone.

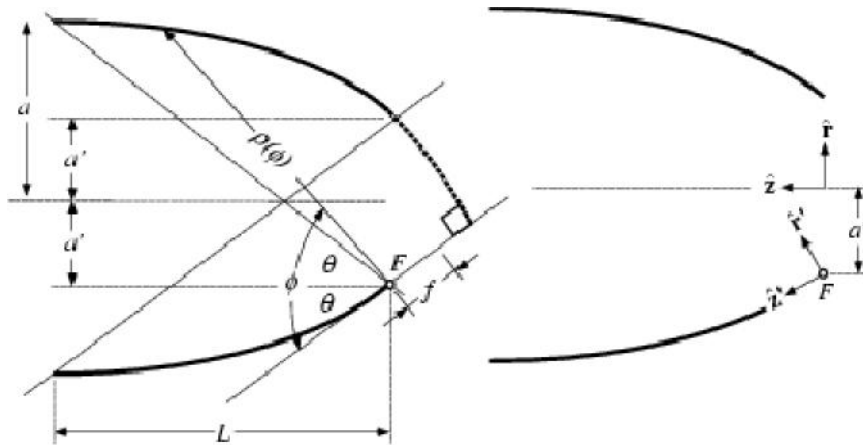

Figure 5.7: Schematic diagram of a Winston cone light concentrator. The entrance and exit apertures have radii of *a* and *a*', respectively. *F* is the focus of the upper parabola segments, and *f* is its focal length. The length of the cone is *L*. Figure reproduced from ref [11].

The concentration factor that the cone can achieve is given by the entrance aperture area ($A_{Entrance}$) divided by the exit aperture area (A_{Exit}). For the Winston cone used here $C \cong \frac{A_{Entrance}}{A_{Exit}} = 65.4$. In spite of this large concentration factor there is only a small portion of the total optical power from a radiator that will be collected because of the small cone of off-axis angles of light, less than 7.1 degrees, that will be collected and concentrated.

5.4 Test Setup: Power Density Measurement Procedure

Power density measurements were performed using broadband illumination provided by a resistance heated Si_3N_4 filament mounted inside a parabolic reflector (Hawkeye, Inc. part number IR-Si 272-P-1), see Figure 5.8. Radiation was collimated by the parabolic reflector and focused using a concave mirror, a 4" diameter CaF_2 lens, and a 1" diameter ZnSe lens. The radiation is spectrally filtered by a Thorlab's mid-IR bandpass filter (discussed above) and concentrated using a Winston cone (described above). The Winston cone was cooled with circulating water to limit the amount of thermal radiation coming from the cone. The Si_3N_4 thermal radiator was biased at 6 and 7 volts where 6 volts corresponded to the vendor's power specification of 30 watts. Optical power density at the sample location was measured using two different calibrated power meters (Newport, model # 1760A and Thorlab's model # PM100A).

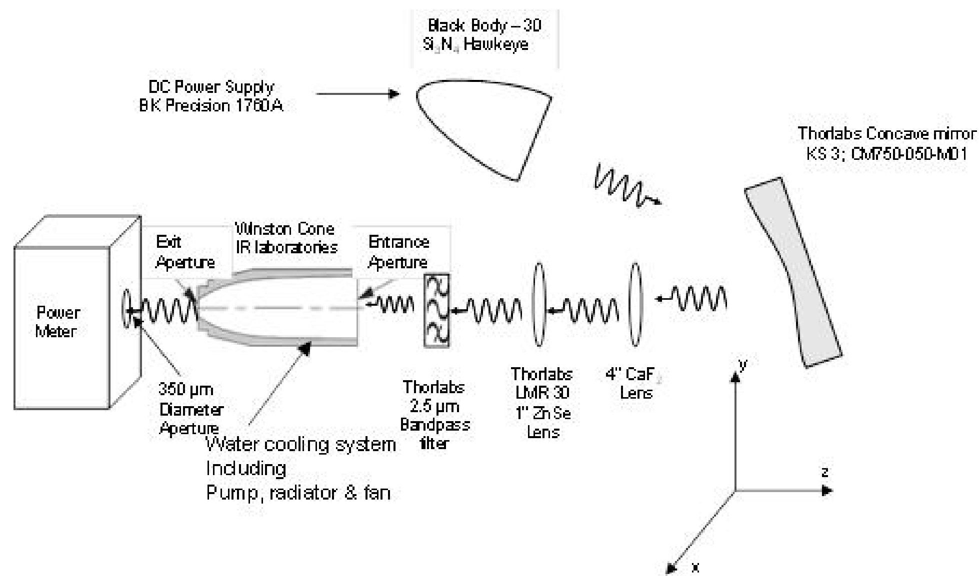

Figure 5.8: Power density measurement setup.

Figure 5.9 shows measured optical power exiting the Winston Cone as a function of distance from the cone exit in the z direction as shown in Figure 5.8. The plot shows the intensity of the beam decreasing as distance from the exit aperture of the Winston cone increases. The position of the TPV device, about 0.5 mm from the cone exit, during testing is indicated. (A minimum distance of about 0.5 mm is needed to allow room for the wire bond electrical connections to the chip perimeter.) The data show that the optical power decreases gradually with only about a 20% reduction in power density at a distance of 2 mm from the cone exit. This shows that there should be fairly good measurement repeatability when devices are placed at the testing location. This is important since it is practically difficult to position a wire bonded device at a specific location relative to the Winston cone exit aperture.

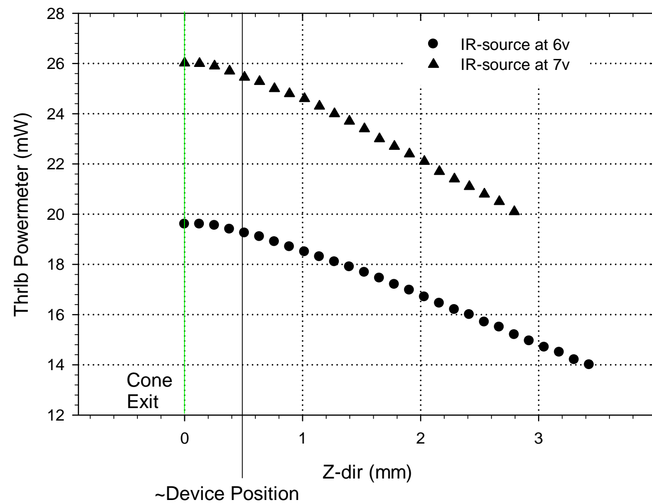

Figure 5.9: Measured infrared optical power exiting the Winston cone as a function of distance from the exit aperture for two infrared source

A water-cooled 0.351 mm diameter aperture placed between the cone exit and the power meter, shown in Figure 5.8, was used to measure the optical power density of

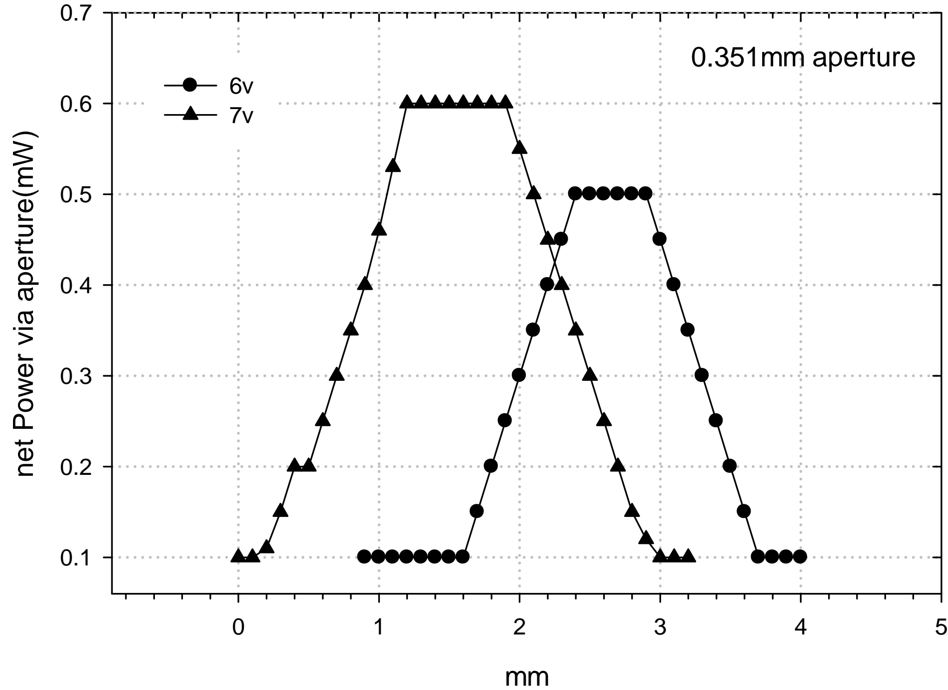

Figure 5.10: Measured infrared optical power exiting the Winston cone as a function of lateral distance perpendicular to the cone axis for two infrared source powers.

the bandpass-filtered infrared beam as it exited the Winston cone. The aperture entrance was placed a distance of about 0.5 mm from the cone exit, where the wire bonded device will be placed, and moved in the x direction. Figure 5.10 shows the results of measurements made with 6 volts (30 watts) and 7 volts of bias applied to the Si_3N_4 thermal radiator. Both plots show a flat-topped beam profile with widths of about 0.8 mm and 0.6 mm, respectively. Uniform incident optical power densities of 620 mW/cm^2 and 540 mW/cm^2 are thus possible with this testing setup.

5.5 TPV Device Characterization with IR Bandpass Filter and Winston Cone

Figure 5.11 shows light emitting diode (LED) emission and detector response spectra for pn junction sample number M292-C along with the bandpass spectral range of the Thorlabs filter used in the testing setup described above. Note the good spectral match to the bandgap of this device material. The low energy edge of the bandpass filter matches almost exactly with the 450 meV bandgap energy, and the high energy edge is only about 100 meV greater than the band gap energy.

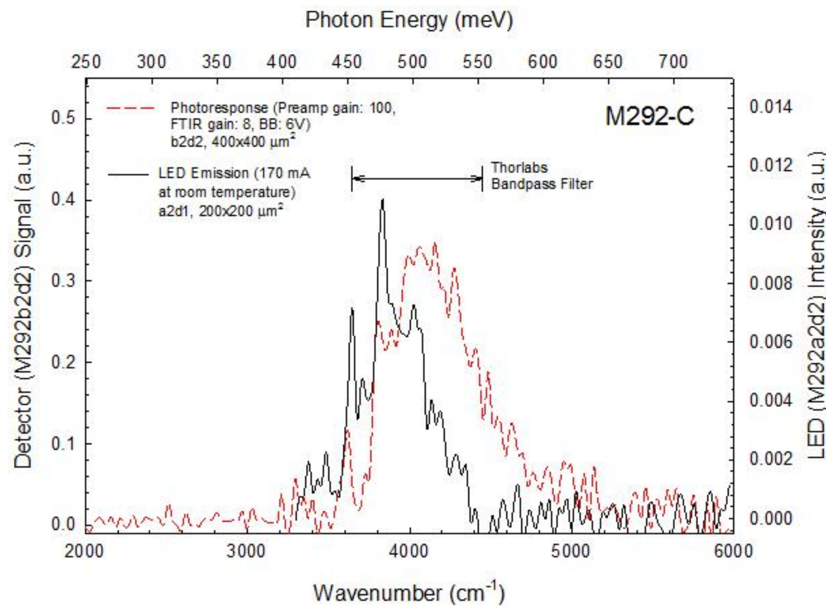

Figure 5.11: LED emission and detector response spectra of pn junction device M292-C showing a bandgap energy of around 450 meV.

Figure 5.12 shows the testing setup for measuring the performance of M292 b1a3. It is identical to the setup described above for measuring the optical power from the exit of the Winston cone except that the TPV device is placed at the same location as

the optical power meter. Current versus voltage characterization was conducted using a Keithley 2400 source meter and a Keithley 2182A nano voltmeter. The device was mounted to a copper base plate on a thermoelectric (TE) cooler, the temperature of which was stabilized using a modular laser diode controller power supply, LDC 3900, ILX Lightwave, Inc.

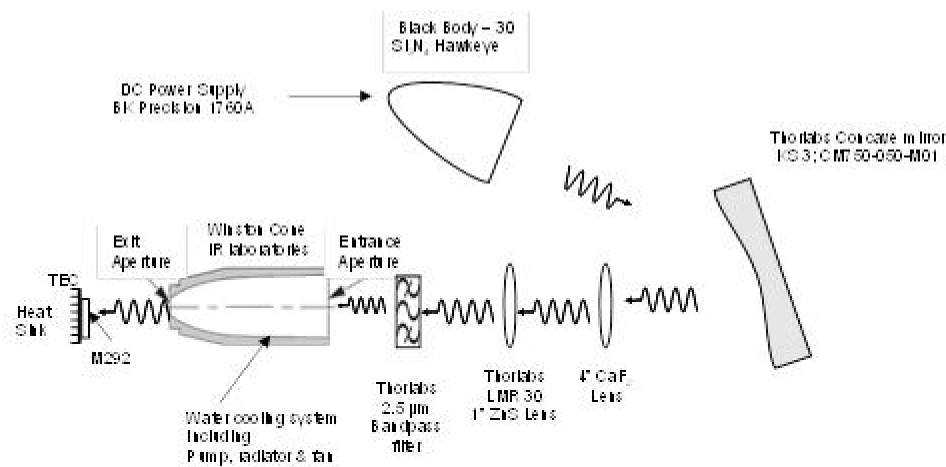

Figure 5.12: Test setup for measuring the performance of TPV device number M292 b1a3.

Figures 5.13 shows the current versus voltage characteristics at a heat sink temperature of 10°C for device number M292 b1a3, a bulk $Pb_{0.93}Sr_{0.07}Se$ pn junction device having a 400x 400 μm^2 mesa area and a 0.001279 cm^2 open area – the area covered by the top metallization is 0.000321 cm^2. Three plots are shown, dark and illuminated with optical power densities of 620 mW/cm^2 and 540 mW/cm^2. These data show open circuit voltages and short circuit currents of 116 mv and 0.523 mA for

620 mW/cm^2 and 108 mV and 0.386 mA for 540 mW/cm^2.

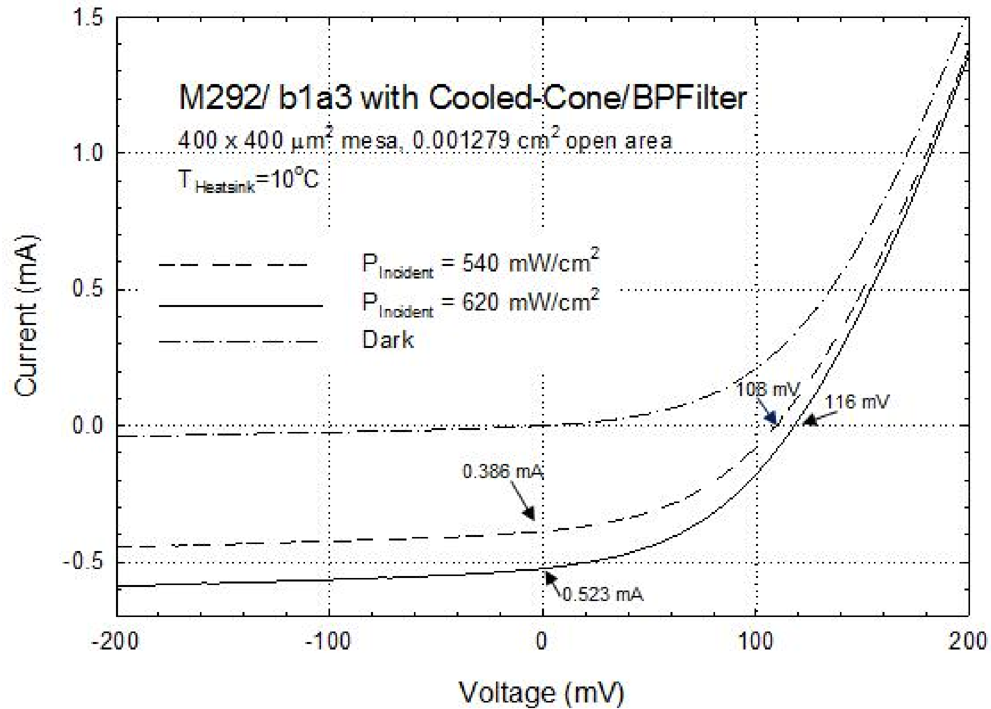

Figure 5.13: Dark and illuminated current voltage characteristics of M292 b1a3.

Figures 5.14 shows the same data as in Figure 5.13 except that current density is plotted on the vertical axis. In this case the open mesa area of 0.001279 cm^2, the portion of the 400 x 400 μm^2 mesa area that is not covered by metal, is used to determine the current density. Short circuit current densities of 409 mA/cm^2 and 302 mA/cm^2 for incident optical power densities of 620 mW/cm^2 and 540 mW/cm^2, respectively, are observed.

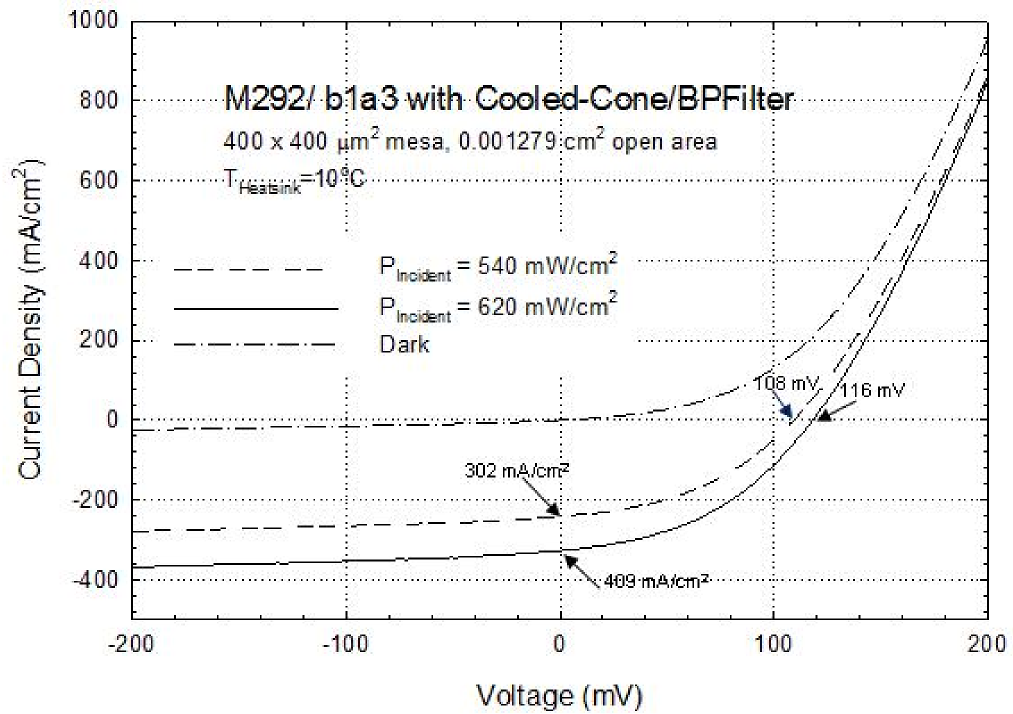

Figure 5.14: Dark and illuminated current density and voltage characteristics of M292 b1a3.

Figure 5.15 is a plot of electrical power generated by M292 b1a3 while it is illuminated with spectrally filtered broadband thermal radiation at a heat sink temperature of 10°C. This device produced peak electrical powers of 21 mW/cm^2 and 14 mW/cm^2 for incident powers of 620 mW/cm^2 and 540 mW/cm^2, respectively.

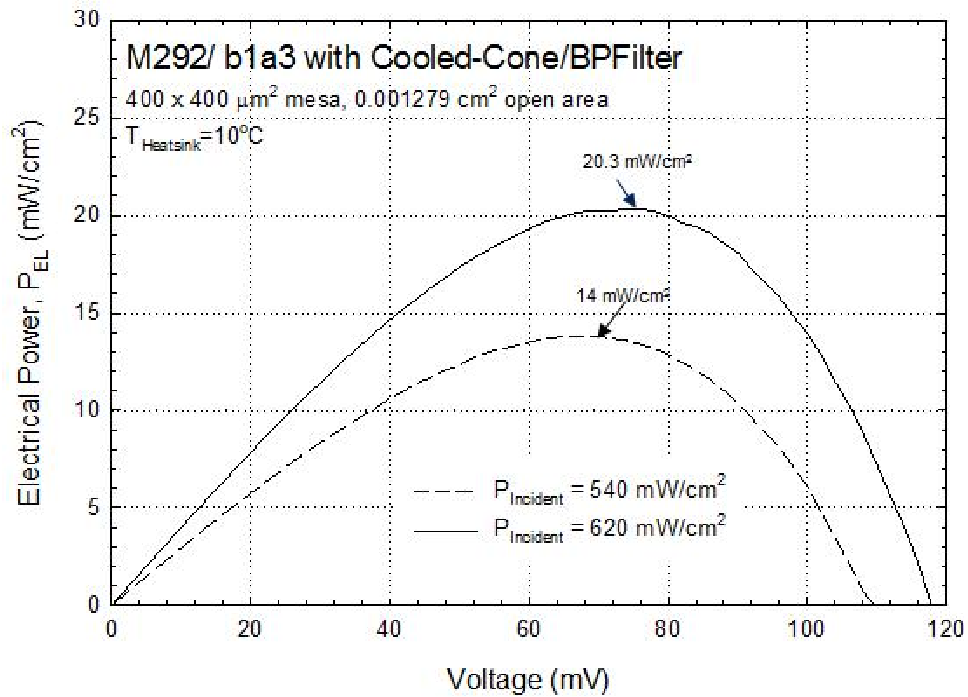

Figure 5.15: Electrical output power of M292 b1a3 at a heat sink temperature of 10°C.

5.6 Discussion

The performance of a PV/TPV cell is determined by three parameters, short circuit current density, J_{sc}, open circuit voltage, V_{oc}, and fill factor, FF. Short circuit current densities and open circuit voltages are measured directly as described above. Fill factor is calculated as the ratio of the maximum power output (P_{max}) divided by open circuit voltage and short-circuit current density and can be expressed as:

$$FF = \frac{P_{\max}}{V_{oc} J_{sc}} \tag{5.19}$$

A fill factor of 42.8% is obtained for P_{max} = 20.3 mW/cm^2, J_{sc} = 409 mA/cm^2, and V_{oc} 116 mV. This FF compares well with recently published values for other experimental TPV device technologies [13]. The optical-to-electrical power conversion efficiency of M293 b1a3 was calculated from the measured data as the ratio of the generated electrical power divided by the incident optical power

$$y = \frac{V_{oc} J_{sc} FF}{P_{in}} \tag{5.20}$$

The measured data for incident power, short circuit current density (Jsc), open circuit voltage (Voc) and the calculated value of fill factor (FF) and efficiency ( ) for M292 b1a3 at 283K are presented in Table 5.3.

Table 5.3: IR source power, incident optical power density, short circuit current density (Jsc), open circuit voltage (Voc), fill factor (FF), electrical output power and power conversion efficiency ( ) for TPV device number M292 b1a3 at 283K.

IR Source (V)	Incident Power (mW/cm^2)	J_{sc} (mA/cm^2)	Voc (V)	FF	Electrical Output Power (mW/cm^2)	Power Conv. Efficiency (%)
6	540	302	0.108	0.423	14	2.6
7	620	409	0.116	0.428	21	3.3

The external quantum efficiency (EQE) of TPV device number M292 b1a3 was also analyzed. EQE is calculated as the ratio of the number of charge carriers collected by the cell divided by the number of incident photons.

$$\text{EQE} = \text{\# of electrons collected/ \# of incident photons.} \tag{5.21}$$

The number of electrons collected is calculated by dividing the short circuit current density J_{sc} by the charge of an electron

$$\frac{0.409 mA/cm^2}{1.6\times10^{-19}\,Coulombs} = 2.56\times10^{18}\,electrons/s/cm^2 \qquad (5.22)$$

The number of incident photons (photon flux) is calculated by assuming a single photon energy of 500 meV, which is the in the center of the 450 meV to 550 meV band that passes through the bandpass filter,

$$E(500meV) = h€ = 0.8\times10^{-19}\,Joules/photon \qquad (5.23)$$

The incident photon flux is thus the incident power (0.620 Joules/s/cm^2) divided by the photon energy

$$\frac{0.62}{0.8\times10^{-19}} = 7.75\times10^{18}\,photons/s/cm^2 \qquad (5.24)$$

and this is used to obtain an EQE value

$$\text{EQE} = \frac{2.56\times10^{18}}{7.75\times10^{18}} = 0.3298 \approx 33\% \qquad (5.25)$$

For the lower incident power density of 540 mW/cm^2 the EQE is calculated to be 28.0%.

The internal quantum efficiency (IQE) is defined as the number of collected electrons divided by the number of absorbed photons.

$$\text{IQE} = \text{\# of electrons collected/ \# of absorbed photons.} \qquad (5.26)$$

By assuming a reflection loss of 40%, a value that is supported by prior experimental work [13], the number of absorbed photons can be calculated

$$\text{\# of absorbed photons} = \text{\# of incident photons* } (1 - 0.40) \qquad (5.27)$$

IQE values of 54.9% and 46.7 % are calculated for the 620 mW/cm^2 and 540 mW/cm^{2}incident optical power densities, respectively. A summary of the measured and calculated data for TPV device number M292 b1a3 at 283K is presented in Table 5.4. IQE values in the range of 50% show fairly good device performance where about half of the absorbed photons are effectively converted to useful electrical power.

Table 5.4: Incident power, absorbed photons, incident photons, e-charge/current, EQE and IQE for M292 b1a3 at 283K.

Incident Power (mW/cm^2)	absorbed photons (Photons /s/cm^2)	incident photons (Photons /s/cm^2)	e-charge/ current (electron s/s/cm^2)	EQE (%)	Reflection Loss (%)	IQE (%)
540	4.05E18	6.75E18	1.88E18	27.96	40	46.7
620	4.65E18	7.75E18	2.56E18	32.98	40	54.9

5.7 Summary and Conclusion

In this chapter the technical aspects of designing a mid-infrared bandpass filter and an optical concentrator (Winston cone) were reviewed. The use of such passive optical components, which can enable accurate simulation of the actual conditions that a TPV device would experience in a well-designed TPV generator system, was also described. Results from the characterization of TPV device number M292 b1a3 when illuminated with broadband thermal radiation that went through a bandpass filter and a Winston cone were described and analyzed. Values for open circuit voltage, short circuit current density, and power conversion efficiency of 116 mV, 409 mA/cm^2, and 3.3% were obtained for an incident optical power density of 620 mW/cm^2 when the

heat sink temperature of the TPV device was 283K. The analysis of EQE and IQE was also conducted for the device. EQE increased from 28.0% to 32.9% when the illumination intensity was increased from 540 mW/cm^2 to 620 mW/cm^2. Corresponding IQE values of 46.7% and 54.9% were estimated based on a reflection loss of 40%. These data show that about half of the absorbed thermal photons were converted to useful electrical power by the device.

References:

[1] D. Cooke, P. Gleckman, H. Krebs, J. O'gallagher, R. Winston, and D. Sagie, “Sunlight brighter than the Sun. (solar flux concentration)”, Nature, August 30, 1990, Vol. 346, p.802.

[2] Charalambos C. Katsidis and Dimitrios I. Siapkas "General transfer-matrix method for optical multilayer systems with coherent, partially coherent, and incoherent interference "Applied Optics Vol. 41, No. 19. p. 3978 (2002).

[3] A. Herpin, Compt. rend. 225, 182 (1947).

[4] F. Abeles, Ann. phys. [12] 5, 596 and 706 (1950).

[5] B.S. Verma; A. Basu; R. Battacharyya and V.V. Shah, " General Expression for the Reflectance of an All-Dielectric Multilayer Stack", Appl. Opt. Vol. 27, pp. 4110-4116, (1988).

[6] W. Z. Shen, H. F. Yang, L. F. Jiang, K. Wang, and G. Yu, H. Z. Wu and P. J. McCann," Band gaps, effective masses and refractive indices of PbSrSe thin films: Key properties for mid infrared optoelectronic device applications" J. Appl. Phys., vol. 91, no. 1, pp. 3319–3327, Jan. 2002.

[7] Winston, R. 1970. Light collection within the framework of geometric optics. *J. Opt. Soc. Amer.* 60, 245-247.

[8] Hildebrand, R. H. and R. Winston 1982. Throughput of diffraction-limited field optics system for infrared and millimetric telescopes. *Appl. Opt.* 21, 1844-1846.

[9] Hildebrand, R. H. 1985. Erratum to: Throughput of diffraction-limited field optics system for infrared and millimetric telescopes. *Appl. Opt.* 24, 616.

[10] Welford, W. T. and R. Winston 1989. *High Collection Nonimaging Optics.* San Diego: Academic Press.

[11] http://www.ericweisstein.com/research/thesis.

[12] Ari Rabl “Comparison Of Solar Concentrators” Solar Energy. Vol. 18. pp. 93-111. Pergamon Press 1976. Printed in Great Britain.

[13] H. Lotfi, R. T. Hinkey, L. Li, R. Q. Yang, J. F. Klem, and M. B. Johnson, “Narrow-bandgap photovoltaic devices operating at room temperature and above with high open-circuit voltage”, *Applied Physics Letters* 102, 211103 (2013).

Chapter 6

Summary and Future Investigations

God does not care about our mathematical difficulties. He integrates empirically.
Albert Einstein

6.1 Summary of Results

Chapter 1 described the fundamentals of thermophotovoltaic (TPV) technology with a discussion of infrared electromagnetic radiation and related technologies in the areas of infrared spectroscopy and thermal detectors. Currently available portable power technologies, Carnot efficiency, and the promise of a TPV technology to improve electrical power generator systems were reviewed. The importance of selecting an optimal emitter [1] was also presented. Prior work in the TPV technology area was discussed [2-3], and finally the encouraging prediction of the possibilities for power conversion efficiencies of 50% and greater with the development of a low bandgap junction in a multi-junction cell [4] was discussed.

Chapters 2 and 3 discussed the density of states and intrinsic carrier concentrations in bulk and quantum well (QW) materials. Mathematical expressions were developed for how electronic band structure information (i.e. effective mass and valley degeneracy) can be used to determine intrinsic carrier densities at different temperatures. Equations showing how a reduction in intrinsic carrier density can decrease reverse bias dark current and increase open circuit voltage in a TPV device were also developed. The developed expressions were then used to evaluate the use of IV-VI semiconductors, which have direct gap conduction and valence band extrema at the four-fold degenerate L-point in k-space, as photovoltaic device materials. The

specific case of quantum confinement in the [111] direction, which removes L-valley degeneracy [5], was investigated for PbSe quantum wells (QWs) with $Pb_{1-x}Sr_xSe$ barriers. Using Schrodinger's equation and the two different effective masses for charge carriers in the degeneracy split normal (or longitudinal) L-valley and the higher energy three-fold degenerate oblique L-valleys, the largest possible degeneracy splitting energies for three different normal valley subband energy gaps of 450 meV, 550 meV and 650 meV were found to be 21.7 meV, 37.1 meV, and 43.9 meV, respectively. Intrinsic carrier concentrations were calculated for these QWs using density of states functions and Fermi-Dirac statistics. It was found that thermally generated intrinsic carrier density can be reduced by more than an order of magnitude as compared to that of a bulk IV-VI semiconductor with the same bandgap energy. Dark current and open circuit voltages for TPV devices made from IV-VI materials were also calculated. Results show that use of optimal QW designs for a 650 meV bandgap material can increase open circuit voltages by almost a factor of two as compared to a bulk material having the same 650 meV band gap energy. With a doubling of open circuit voltages, the incorporation of QW designs in IV-VI semiconductor TPV devices is predicted to enable a 100% increase in optical-to-electrical power conversion efficiencies.

Chapters 4 and 5 of this dissertation presented the experimental results and analysis of IV-VI semiconductor pn junction devices fabricated from a bulk $Pb_{0.93}Sr_{0.07}Se$ active layer. The pn junction layer, which consisted of a 2 μm thick n-type layer doped with bismuth to give an electron density of $n=4x10^{18}$ cm^{-3} and a 2 μm thick p-type layer with a selenium overpressure during growth to give a hole

density of $p=4x10^{17}$ cm^{-3}, was grown by molecular beam epitaxy (MBE) on silicon, transferred to copper using a novel flip-chip eutectic bonding method, and fabricated into mesa-etched device structures with sizes of 200 x 200 μm^2 and 400 x 400 μm^2. Current-versus-voltage characterization was performed with and without broadband illumination at different heatsink temperatures to assess the performance of these devices as TPV cells. Measured reverse bias saturation current densities at -26 mV were observed to increase from 7.5 mA/cm^2 to 26.9 mA/cm^2 as the lattice temperature was increased from 10°C to 50°C. After accounting for band gap temperature dependence and thermal generation effects, these values were consistent with an increase in minority carrier lifetime from 10 ns at 10°C to 100 ns at 50°C. These data show a clear lifetime enhancing thermal re-excitation effect and confirm the high quality of these IV-VI semiconductor epitaxial layer materials for device fabrication applications. Moreover, these data show that high materials quality is maintained during device processing and that there are no significant surface recombination problems with the fabricated device structures. These pn junction devices were also operated at room temperature and in continuous wave (cw) mode as light emitting diodes (LEDs) and as mid-infrared detectors. Representing the first known demonstration of such mid-infrared IV-VI semiconductor device operation, LED emission spectra and detector spectral response showed a bandgap energy of 450 meV (2.76 µm cutoff wavelength) for the MBE-grown $Pb_{0.93}Sr_{0.07}Se$ layer.

Broadband illumination measurements were performed with spectrally-filtered thermal radiation and a parabolic optical concentrator (Winston cone). Unlike illumination with a laser, these testing conditions accurately simulate the environment

that a TPV cell would experience in an actual TPV generator system. Open circuit voltages as high as 116 mV, short circuit current densities as high as 409 mA/cm^2, and fill factors of 43% with an incident optical power density of 620 mW/cm^2 were observed. Generated electrical power was greater than 20 mW/cm^2 thus giving an optical-to-electrical power conversion efficiency of 3.3% for this non-QW device. External quantum efficiency (EQE) and an estimated internal quantum efficiency (IQE) based on an assumed 40% reflection loss were calculated to be 33.0% and 54.9%, respectively. These data show that further optimization of materials growth, device design, and processing techniques, which historically have shown to enable IQE values that approach 100%, could be ultimately used to achieve a power conversion efficiency of greater than 6% for this bulk single-junction device.

The remainder of this chapter offers suggestions for how future work can be conducted to take advantage of the unique materials properties of nano-structured IV-VI semiconductors and how these QW materials can be used within multi-junction TPV cell designs. Since IV-VI semiconductor materials can have smaller bandgap energies than other materials, such work will address the key issue in being able to fabricate TPV cells with the highest possible power conversion efficiencies as identified in ref [4]. Work in the area of improved optical designs to increase the intensity of broadband illumination from a thermal emitter are also offered. Increasing the optical power that is incident on a TPV cell will provide additional improvements in TPV cell power conversion efficiency. This additional improvement will accelerate the overall development of TPV generator technology thus making it a highly viable approach for future electrical power generation systems.

6.2 Recommendations for Future Investigations

MBE Grown Multi-Junction IV-VI Semiconductor Based TPV Devices

One of the fundamental loss mechanisms of the single-junction cell is the energy that goes to thermalization after a high-energy photon has been absorbed (quantum defect loss). This problem can be solved by using a multi-junction cell design. In this arrangement, less energy is lost due to thermalization (i.e. phonon emission) of photogenerated charge carriers. For example, equations 6.1 and 6.2 are expressions for the photocurrents through two junctions with two different band gap energies, E_{g1} and E_{g2} where $E_{g1} < E_{g2}$..

$$J_1 = \int_{E_{g1}}^{E_{g2}} r_1(E)S(E)dE - \frac{f}{y_{ext}^1} e^{\frac{qV_1}{kT}} \int_{E_{g1}}^{\infty} r_1(E)\Phi(E)dE + f n_r^2 e^{\frac{qV_2}{kT}} \int_{E_{g2}}^{\infty} r_1(E) r_2 \Phi(E)dE \qquad (6.1)$$

$$J_2 = \int_{E_{g2}}^{\infty} r_2(E)S(E)dE - \frac{f}{y_{ext}^2} e^{\frac{qV_2}{kT}} \int_{E_{g2}}^{\infty} r_2(E)\Phi(E)dE \qquad (6.2)$$

J_1 is the current through the smaller bandgap junction, and J_2 is the current through the larger bandgap junction. In Eqns. 6.1 and 6.2 the first term represents absorption of the incident radiation, while the second term represents total recombination (radiative and nonradiative). The current J_1 also has a third term, representing the radiative transfer from the larger bandgap TPV cell to the smaller one. This radiative transfer not only leads to extra current for the smaller bandgap TPV cell, it also leads to different external yields, $^{1}_{ext}$ and $^{2}_{ext}$. The internal yield for the smaller bandgap cell, $^{1}_{ext}$, is same as the external yield from a typical plane-

parallel PV/TPV junction. The external yield of the larger bandgap solar cell is smaller because photons escape through the rear of the junction and are absorbed in the other junction instead of being re-directed back into the cell by a mirror. The above calculations for two junctions can be expanded to 3 or more junctions. One key factor for multi-junction cells is that a low resistance connection between each pair of stacked junctions must be incorporated. A way to do this is to increase the doping levels on each side the adjacent junctions to form a degenerately-doped pn junction. Electrons can then tunnel from conduction band states through the band gap into valence band states. Such a tunnel junction is shown in Figure 6.1

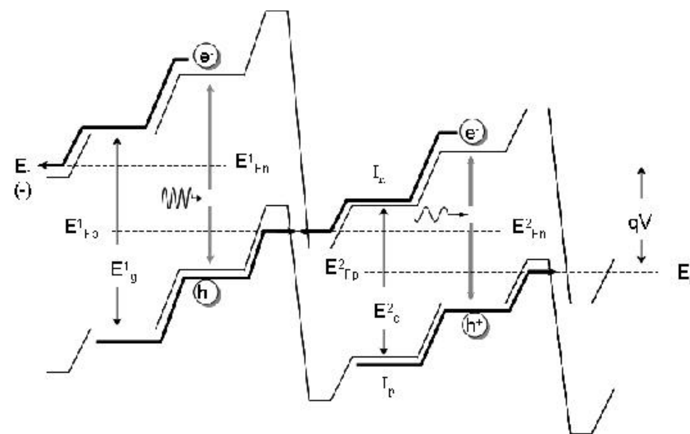

Figure 6.1: Tunnel junction between a dual junction cell, $E_{g1} > E_{g2}$.

The higher electrical power density obtained for multi-junction cells is mostly attributed to a higher power conversion efficiency with a greater portion of the incident spectrum being efficiently converted to electrical power. In the case of

thermophotovoltaic devices, where the spectrum from a thermal radiator has significant emission at wavelengths longer than 2 microns, it is important, as argued in ref. [4], to have a junction with a band gap energy of less than 500 meV in a multi-junction TPV cell design. The 450 meV bandgap TPV devices described in Chapters 4 and 5 of this dissertation describe precisely such a junction. An example of a multi-junction cell is depicted in Figure 6.2. With five pn junctions and four tunnel junctions, a design like this can be used to perform highly efficient conversion of radiated thermal power to electrical power. It is a device like this, one that includes a 450 meV bandgap material, for example, that will likely achieve the 50% power conversion efficiencies that are predicted in ref [4].

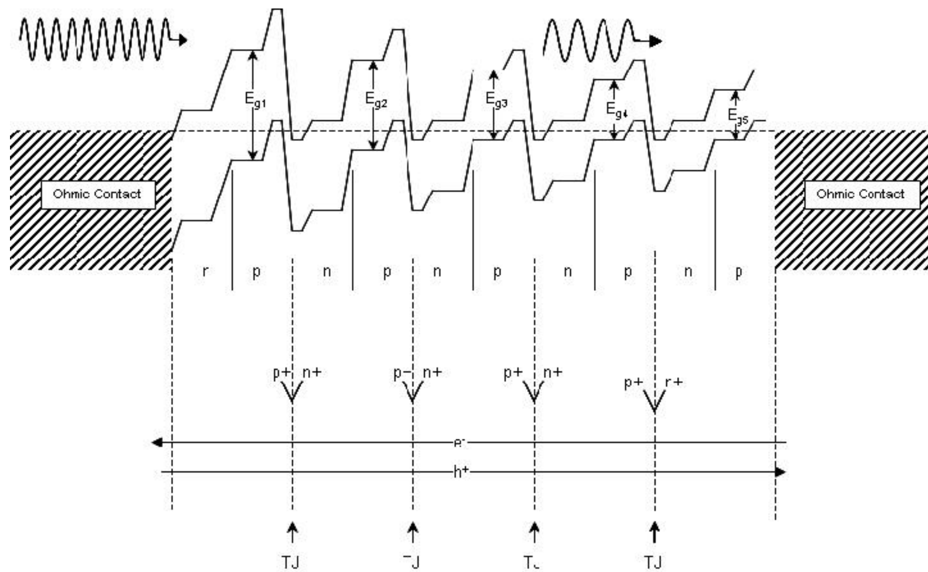

Figure 6.2: TPV multi-junction cell with five junctions.

Multiple Quantum Well (MQW) Materials in Multi-Junction Cells

As discussed in Chapters 2 and 3, it is possible to reduce significantly the intrinsic carrier concentrations in IV-VI semiconductor materials by incorporating quantum wells with confinement in the [111] direction.. The band gaps in the band diagram drawing in Figure 6.2 can thus represent the intersubband gaps between normal (or longitudinal) valleys with each pn junction active layer composed of multiple quantum well (MQW) material. PbSrSe barriers with varying amounts of strontium and PbSe wells with specific thickness to maximize L-valley degeneracy splitting energies can comprise the different junction materials.

As described in Chapter 3, such MQW materials can enable a doubling of power conversion efficiency for a 650 meV band gap material as compared to a bulk PbSrSe material with the same band gap. However, the improvement is smaller for smaller band gap materials. This is due, in part, to a smaller amount to L-valley degeneracy splitting so that there is a smaller reduction in the effective densities of states. A way to increase the power conversion efficiency for smaller band gap MQW materials is to use PbSnSe instead of PbSe as the QW material. PbSnSe, with its smaller band gap energy, will give more design flexibility and allow L-valley degeneracy splitting energies of greater than 40 meV as depicted in Figure 6.3. A large degeneracy splitting energy is desired because there will be less thermal population of the higher energy oblique valley subbands and this will give a smaller effective density of states. Figure 6.3 shows the possibility of growing a deep QW quantum well material by using a very low bandgap material, e.g. $Pb_{1-x}Sn_xSe$ (E_g < 100 meV), for the well material along with a $Pb_{1-x}Sr_xSe$ (x>30) high Sr>30% alloy for the barrier material.

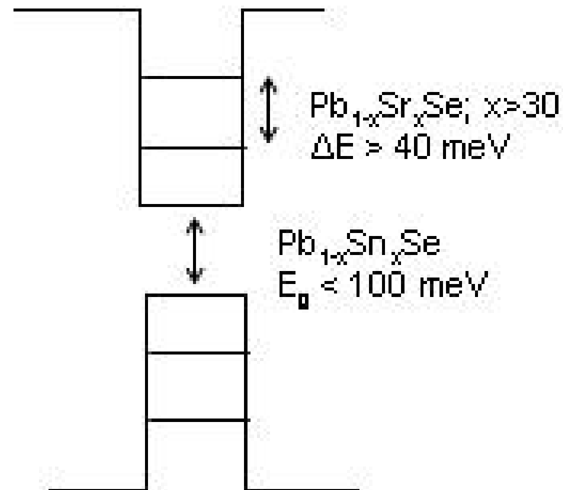

Figure 6.3: IV-VI QW designed for maximum degeneracy split.

Optical Design Monte-Carlo Analysis for Ray Tracing

In order to get better optical efficiency it is important to consider the angular distribution of the optical emission from a thermal radiator. Since the blackbody power distribution is known to be uniform as a function of position on the surface but with directional dependence on emission angle, it is possible to carry out a Monte-Carlo simulation with light being emitted randomly from a surface. The positional and directional distribution of rays, or photons, is the power distribution. The resulting rays can be traced through optical elements such as mirrors, prisms, or lenses following each reflection or refraction to determine the final power flux that is incident on a TPV cell.

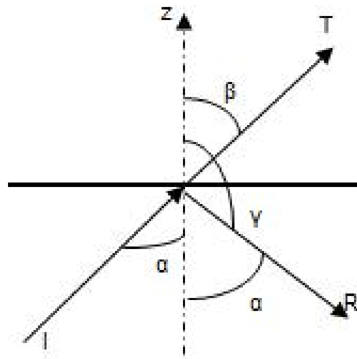

Figure 6.4: Light reflected and

transmitted at the interface z = 0.

For radiation the dependence of the normal component of power upon the angle of incidence as shown in Figure 6.4 relative to the surface normal exhibits a maximum at = /4. Although the power density with respect to angle is positive for all 0 < < /2, a significant amount of the radiation will be emitted from a thermal radiator along suboptimal directions for collection and direction to a TPV cell. It is desired to orient the radiation so that it falls on TPV cells with normal incidence since any incorporated spectral filters, discussed in Chapter 5, will work optimally with = 0.

Recently, Teng et al. [7] described a planar collimator design that can be useful for collecting light from a wide range of emission angles from a radiator and directing it to a TPV cell. The design effectively employs total internal reflection to capture light that is emitted at large angles relative to the normal and redirects it through a refractive element to produce a highly collimated beam of light. Developed for improving the directional emission of light through a liquid crystal display (LCD) screen, the planar collimator described in ref. [7] consists of an array of inverted cones

on one side and an array of lenses on the other side, see Figure 6.5. As shown in Figure 6.6, light entering the left side of the cone will experience total internal reflection at the right side of the cone and be directed vertically where a lens on the opposite side provides additional collimation. Using Monte-Carlo ray tracing software (Light Tools, Synopsis, Inc.) to simulate collimation of radiation from an LCD back light, Teng et al. [7] showed a high degree of collimation with this planar collimator design. This Monte-Carlo modeling work was confirmed by experimental demonstrations of visible light collimation (greater than 90% of the light exiting the collimator with an angle of less than 15 degrees relative to the normal) using planar collimator structures fabricated from UV-cured resin.

Guided by the prior work described in ref. [7], work on developing a planar collimator for directing infrared light from a thermal radiator to TPV cells can be planned. In this case the planar collimator can be fabricated from infrared transparent silicon, which is also suitable for close placement to a hot radiator due to its high melting point of 1414°C. Techniques for forming arrays of micro-lenses on one side of a silicon wafer using etching and thermal reflow and cones on the other side using anisotropic KOH wet etching are available. Optimizing the lens and cone patterns of such a Si-based planar collimator can be achieved through Monte-Carlo ray tracing simulations. A well-designed infrared Si-based planar collimator, like the one proposed here, can be placed very close to a combustion-heated planar radiator so that most of the thermal photons can be directed to TPV cells with predominantly normal incidence. The incident optical power density can thus be close to the theoretical numbers from a blackbody radiator. For example, a 1200°C radiator with a 90%

emissivity (such as SiC) will have a total radiated power of 24.0 W/cm^2 of which 13.2 W/cm^2 will be below a wavelength of 3 microns. This optical power density is significantly larger than those used to measure the performance of the TPV devices described in Chapters 4 and 5. In addition, a compound parabolic concentrator (Winston cone) could be used in conjunction with a planar collimator to achieve even larger incident optical power densities. Since TPV power conversion efficiency increases with incident optical power (see the data in Chapters 4 and 5), planar optical collimation provides an additional technique that can be used to improve the overall performance of a TPV generator system

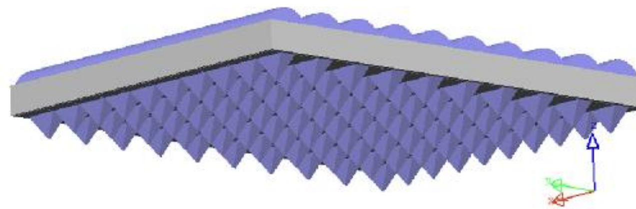

Figure 6.5: Planar collimator design. Figure reproduced from [7].

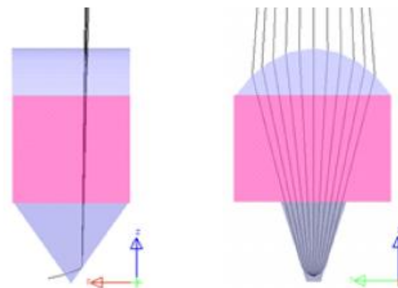

6.3

Figure 6.6: The mechanism to collimate light using total internal reflection and refraction. Figure reproduced from [7].

6.3 Summary and Conclusion

The research results presented in this dissertation represent a significant step towards making TPV technology a viable way to generate electrical power from thermal radiators. For the first time TPV device efficiency improvement of over 50% with use of a IV-VI semiconductor QWs is predicted for a 650 meV material.Three experimental achievements in the TPV field have also been determined for the first time as well:

1. Use of a low-cost silicon substrate technology for epitaxial growth of a narrow bandgap photovoltaic device material
2. Fabrication of IV-VI semiconductor TPV devices with long minority carrier lifetimes of between 10 ns and 100 ns and internal quantum efficiencies of greater than 50%
3. Demonstration of a 450 meV bandgap pn junction device to fill an important gap in covering the infrared spectrum.

In addition, this dissertation described the benefits of using MQW materials, multi-junction cells, and planar optical collimators to provide future improvements in TPV cell power conversion efficiencies.

The experimentally demonstrated optical-to-electrical power conversion efficiency of 3.3% reported here represents an important milestone in the TPV field. This number can be understood within the context of a portable power supply that is based on propane combustion. When propane undergoes combustion reactions in the presence of oxygen we get

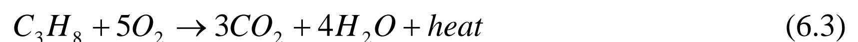

$$C_3H_8 + 5O_2 \rightarrow 3CO_2 + 4H_2O + heat \quad (6.3)$$

with an enthalpy of combustion of 14 kWhr/kg. One can assume that 50% of this combustion energy can be converted to incident optical power on a TPV cell. This 50% conversion efficiency takes into account losses associated with convection of combustion reaction products, radiator emissivity, and optical collection. This is a relatively conservative assumption since convection and emissivity losses can be 10% or less and there are effective ways to limit optical losses as discussed above. Using the 3.3% TPV power conversion efficiency demonstrated with MBE sample number M292, the electrical energy density of a propane-based TPV power supply will be 231 Whr/kg. The energy density of a lithium ion battery is 140Whr/kg. So even at this very early stage of TPV device development there are potential applications where a high energy density power supply is needed. Such applications would fill a gap between lithium ion battery and internal combustion engine power supplies.

As discussed earlier in this Chapter, a multi-junction TPV cell with MQW active layers can ultimately achieve the 50% power conversion efficiencies that are predicted in ref [4]. It is truly exciting to be at the point where there is enough experience and enough knowledge [11] of the individual components to envision the path that this new electrical power generation technology can take. The theoretical work described in this dissertation should prove to be valuable in working towards developing improved TPV device materials, and the experimental work described here provides a solid foundation upon which to new materials and device designs can be implemented.

References:

[1] R. Siegel, J. Howell, Thermal Radiation Heat Transfer, Mc Grew Hill, 1972.

[2] D.L Chubb. Fundamentals of Thermophotovoltaic Energy Conversion. Elsevier, 2007.

[3] C.A. Wang, R.K. Huang, D.A. Shiau, M.K. Connors, P.G. Murphy, P.W. O'Brien, A.C. Anderson, D.M. DePoy, G. Nichols, M.N. Palmisiano, Monolithically series- interconnected GaInAsSb/AlGaAsSb/GaSb thermophotovoltaic devices with an internal back surface reflector formed by wafer bonding, Appl. Phys. Lett. 83 (7) (2003) 1286–1288.

[4] A Datas, "Optimum semiconductor band gaps in single junction and multi junction thermo photovoltaic converters", Solar energy materials & Solar Cells 134 (2015) 275-290.

[5] H. Z. Wu, N. Dai, M. B. Johnson, P. J. McCann, and Z. S. Shi, “Unambiguous Observation of Subband Transitions from Longitudinal Valley and Oblique Valleys in IV–VI multiple Quantum Wells”, *Applied Physics Letters* **78**, 2199 (2001).

[7] Tun-Chien Teng and Jau Chian Ke “A novel optical film to provide a highly collimated planar light source”, Optics Express 21444, Vol. 21, No. 18 DOI: 10.1364 / OE.21.021444 (2013).

[8] A. Datas, D.L. Chubb, A. Veeraragavan, Steady state analysis of a storage integrated solar thermophotovoltaic (SISTPV) system, Sol. Energy 96 (0) (2013).

[9] A. Datas, C. Algora, Global Optimization of solar thermophotovoltaic systems, Prog. Photovoltaics: Res. Appl. 21 (5) (2013) 1040–1055.

[10] A. Data, C. Algora, Detailed balance analysis of solar thermophotovoltaic systems made up of single junction photovoltaic cells and broadband thermal emitters, Sol. Energy Mater. Sol. Cells 94 (12) (2010) 2137–2147.

[11] Lewis Fraas, James Avery and Leonid Minkin, “Design And Thermal Modeling Of A Portable Fuel Fired Cylindrical TPV Battery Replacement”, JX Crystals Inc.

APPENDIX A

M292 MBE Run Sheet

M292

Layers (target thickness)	
PbSe n-type	PbSe,Se Bi_2Se_3,Sr (2 μm)
PbSe p-type	PbSe,Se, Sr (2 μm)
Reaction BaF_2	BaSe (<1nm)
Release	BaF_2 (3μ)
Buffer	CaF_2 (2.6nm)
	Si (111)

SiO_2 Desorption	Not clear 7×7 sub@ 850°C
CaF_2 RHEED	Post RHEED streaky
IV-VI RHEED	Streaky
Visual Observation and Comments	This sample had two BaF_2 growths. One thin 10/26/15 (30min 120nm) and the other thick 11/10/15 (12 hours 2880nm) make a grand total of 3000nm of BaF_2 . Sample appears shiny with no delamination Slight Haze

Substrate Batch #	Sample(s)/Block	Grower(s)	Dates
Silicon Sense, Inc, invoice# 6472, PO#, LOT#603-891-4248, 3inch <111>, Resistivity <0.005, Dopant: p(Boron), Thickness 381+/-25 μm, Date: 09/09/2013	3" Si A8 Uni Block	Len	10/26, 11/11
		Len	11/17/15

Ex-situ Cleaning		In-situ Cleaning				
Shiraki Clean @ 10-23-2015		Outgassed at 350°C 24h				
Layer Structure		RHEED	Sub Temp Thermocouple	Target Time nm/μ		Comments
PbSe n-type	PbSe, Se, Sr, Bi_2Se_3		325	14,600 sec	2μ	24% Se PbSe, RHEED $n \sim 4x10^{18}$ cm^{-3}
PbSe p-type	PbSe, Se, Sr		325	14,600 sec	2μ	24% Se/PbSe $p \sim 4x10^{17}$ cm^{-3}
Reaction BaSe			620	30mins	<1	Convert BaF_2 surface to BaSe
BaF_2 Release			800	12hrs	2880	12 hour thick BaF_2
BaF_2 Release			800	30 min	120	Broken up into two growths
CaF_2			800	60Sec	2.6	
		7×7	850	2 min		
Oxide Desorption		1×1	600	1min		

Date(s)/Time(s) for Flux Measurements (EpiTrend): CaF_2, BaF_2 fluxes taken on 10/26,11/11 the rest on 11/17/15

Growth Parameters		CaF_2	BaF_2	PbSe	Se Cracker Bulk	Sr	Ag	Bi_2Se_3
Cell Temp (°C)		1265	1158	737/487	900/260, 12.7mils	446		690
Target BEP		1.20E-07	2.4E-7	6.10E-07	1.46e-7	1.8e-8		5.5e-8
Background	pre-growth	1.60e-7	1.44e-7 5.07e-8	6.39e-9	5.39e-9	5.88e-9		5.88e-9
	post-growth							
Beam Flux	pre-growth	2.95e-7	3.75e-7 2.62e-7	6.31e-7	1.52e-7	2.54e-8		
	post-growth							
BEP	pre-Growth	1.5e-7	2.47e-7 2.31e-7	62e-7	1.46e-7 / 1.19e-7 after 10mins	1.88e-8		

M292 MBE Run Sheet

1×1 @ 700°C 7×7 @ 850C Post CaF_2 growth

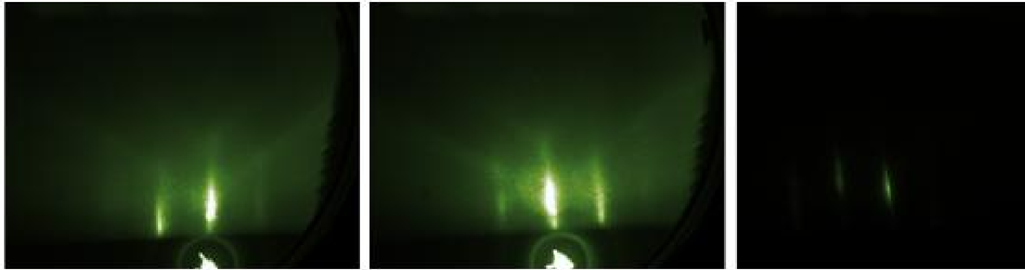

Flat 100X Center 100X Round 100X

Flat, 400× Center, 400× Round, 400×

M292 MBE Run Sheet

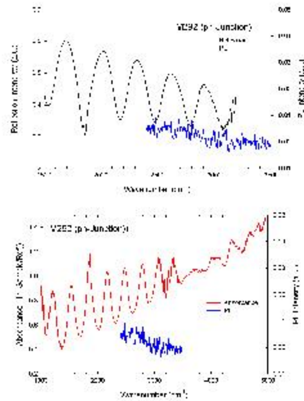

MBE Growth, Processing, and Testing Instructions

Layers (target thicknesses)		Open Shutters (time)	Alloying, Doping, etc.
PbSe n-type	$Pb_{0.93}Sr_{0.07}Se$ (2 μm)	PbSe, Se, Sr, Bi_2Se_3 (14,600 sec)	24% Se/PbSe, RHEED n ~ $4x10^{18}$ cm^{-3}
PbSe p-type	$Pb_{0.93}Sr_{0.07}Se$ (2 μm)	PbSe, Se, Sr (14,600 sec)	24% Se/PbSe p ~ $4x10^{17}$ cm^{-3}
Cool CAR to 325°C at 5Ê1C/min (1 hour)			
Reaction	BaSe (<1 nm)	Se (30 min)	
Heat CAR to 620°C			
Measure Bi_2Se_3, PbSe, Sr, & Se Fluxes			
*Growth Interrupt – Wafer Parked in Buffer Chamber**			
Release/Buffer	BaF_2 (3 μm)	BaF_2 (12.5 hours)	
Buffer	CaF_2 (2.6 nm)	CaF_2 (60 sec)	CAR 800°C
	Oxide Desorption		CAR to 850°C
Measure CaF_2 & BaF_2 Fluxes			
Shiraki Cleaned Si (111)			

* Oxide desorption and fluorides growth were performed in week of October 26, 2015. The BaF_2 was grown in two steps, 0.5 hours + 12 hours.

MBE Growth Notes:

1) This is a pn junction growth of bulk ternary $Pb_{0.93}Sr_{0.07}Se$ on thick (~3 μm) BaF_2.
2) The Bi_2Se_3 BEP of $3.3x10^{-8}$ Torr is the same as with M278, which had an electron density of $3.9x10^{18}$ cm^{-3}.
3) The Se/PbSe BEP ratio is 24%. The valve position should be in the range of 13.0 mils.

Processing/Testing Plan:

[2] Take whole wafer digital camera and Nomarski images.
[3] Cleave wafer in half, and cleave one of the halves into quarters. Cleave one of the quarters into at least four (4) 1 x 1 cm^2 chips and number each one with center, flat, and round notations.
[4] Perform Hall effect, PL, and absorption (using reflection geometry) measurements.
[5] Fabricate into testable photovoltaic devices.

Source	BEP	Expected Cell Temp
Se	$1.46x10^{-7}$	900°C/260°C/~13.0 mils
Bi_2Se_3	$3.3x10^{-8}$	690°C
Ag	NA	NA
Sr	$1.83x10^{-8}$	444°C
PbSe	$6.10x10^{-7}$	487°C (base)/738°C (tip)

APPENDIX B

MATLAB Code for Band Pass Filter

```
%Transfer Matrix Program (CWL~5μm)
clear
v= [300 900 0 2];
alpha = pi/4;
d1=5000/4/5.9;
d2=5000/4/1.38;
N=5;
lambda=v(1):1:v(2);
%Lambda
l00=[4000 6000];
n00=[1.1];
l10=[4000 6000];
n10=[5.9 5.9];
k10=[0 0];
l20=[4000 6000];
n20=[1.38 1.38];
k20=[0 0];
l30=[4000 6000];
n30=[1.1];
%interpolation function for refractive indices for all lambda
n0=interp1(l00,n00,lambda);
n1=interp1(l10,n10,lambda);
k1=interp1(l10,k10,lambda);
n2=interp1(l20,n20,lambda);
k2=interp1(l20,k20,lambda);
n3=interp1(l30,n30,lambda);
[T,R]=trans_matrix(n0,n1,k1,n2,k2,n3,d1,d2,N,alpha,lambda);
figure(1);
hold on;
plot(lambda,T,'k:');
ylabel('Transmission (%)');
xlabel('Wavelength(μm)');
grid on;
axis(v);
%Function subroutine
function[T,R]=trans_matrix(n0,n1,k1,n2,k2,n3,d1,d2,N,alpha,lambda)
for n=1:length(lambda)
   f1=asin(sin(alpha)*n0(n)/(n1(n)+1i*k1(n)));
   f2=asin(sin(alpha)*n0(n)/(n2(n)+1i*k2(n)));
   f3=asin(sin(alpha)*n0(n)/n3(n));
   [r01p,t01p,r01s,t01s]=f_rtamp(n0(n),0,n1(n),k1(n),f0,f1);
   [r12p,t12p,r12s,t12s]=f_rtamp(n1(n),k1(n),n2(n),k2(n),f1,f2);
   [r21p,t21p,r21s,t21s]=f_rtamp(n2(n),k2(n),n1(n),k1(n),f2,f1);
   [r23p,t23p,r23s,t23s]=f_rtamp(n2(n),k2(n),n3(n),0,f2,f3);
%Function subroutine(amplitude)
function [rp,tp,rs,ts]= trans_matrix1(n1,k1,n2,k2,f1,f2)
n1=n1-1i*k1;
n2=n2-1i*k2;
rp=(n1*cos(f2)-n2*cos(f1))/(n1*cos(f2)+n2*cos(f1));
rs=(n1*cos(f1)-n2*cos(f2))/(n1*cos(f1)+n2*cos(f2));
tp=2*n1*cos(f1)/(n1*cos(fi2)+n2*cos(f1));
ts=2*n1*cos(f1)/(n1*cos(f1)+n2*cos(f2));
```

```
%Transfer Matrix Program (CWL~2.5μm)
clear
v=[300 900 0 2];
alpha=pi/4;
t1=2500/4/5.9;
t2=2500/4/1.38;
N=5;
lambda=v(1):1:v(2);
%Lambda
l00=[1000 4000];
n00=[1 1];
l10=[1000 4000];
n10=[5.9 5.9];
k10=[0 0];
l20=[1000 4000];
n20=[1.38 1.38];
k20=[0 0];
l30=[1000 4000];
n30=[1 1];
%interpolation function for refractive indices for all lambda
n0=interp1(l00,n00,lambda);
n1=interp1(l10,n10,lambda);
k1=interp1(l10,k10,lambda);
n2=interp1(l20,n20,lambda);
k2=interp1(l20,k20,lambda);
n3=interp1(l30,n30,lambda);
[T,R]=trans_matrix(n0,n1,k1,n2,k2,n3,d1,d2,N,alpha,lambda);
figure(1);
hold on;
plot(lambda,T,'k:');
ylabel('Transmission (%)');
xlabel('Wavelength(μm)');
grid on;
axis(v);
%Function subroutine
function[T,R]=trans_mtix(n0,n1,k1,n2,k2,n3,d1,d2,N,alpha,lambda)
for n=1:length(lambda)
   f1=asin(sin(alpha)*n0(n)/(n1(n)+1i*k1(n)));
   f2=asin(sin(alpha)*n0(n)/(n2(n)+1i*k2(n)));
   f3=asin(sin(alpha)*n0(n)/n3(n));
   [r01p,t01p,r01s,t01s]=f_rtamp(n0(n),0,n1(n),k1(n),f0,f1);
   [r12p,t12p,r12s,t12s]=f_rtamp(n1(n),k1(n),n2(n),k2(n),f1,f2);
   [r21p,t21p,r21s,t21s]=f_rtamp(n2(n),k2(n),n1(n),k1(n),f2,f1);
   [r23p,t23p,r23s,t23s]=f_rtamp(n2(n),k2(n),n3(n),0,f2,f3);
%Function subroutine(amplitude)
function [rp,tp,rs,ts]= trans_mtix1(n1,k1,n2,k2,f1,f2)
n1=n1-1i*k1;
n2=n2-1i*k2;
rp=(n1*cos(f2)-n2*cos(f1))/(n1*cos(f2)+n2*cos(f1));
rs=(n1*cos(f1)-n2*cos(f2))/(n1*cos(f1)+n2*cos(f2));
tp=2*n1*cos(f1)/(n1*cos(fi2)+n2*cos(f1));
ts=2*n1*cos(f1)/(n1*cos(f1)+n2*cos(f2));
```